

**Molecular Dynamics Simulations of the Shock Response of the
Energetic Materials Pentaerythritol Tetranitrate and Hexahydro-1,3,5-
Trinitro-1,3,5-s-Triazine**

A Dissertation Presented to the Faculty
of the Graduate School of the
University of Missouri-Columbia

In Partial Fulfillment
of the Requirements of the Degree
Doctor of Philosophy

By
Reilly M. Eason
Prof. Thomas D. Sewell, Dissertation Supervisor
May 2016

The undersigned, appointed by the Dean of The Graduate School, have examined the dissertation entitled:

Molecular Dynamics Simulations of the Shock Response of the Energetic Materials Pentaerythritol Tetranitrate and Hexahydro-1,3,5-Trinitro-1,3,5-s-Triazine

Presented by Reilly Michael Eason

A candidate for the degree Doctor of Philosophy

And hereby certify that, in their opinion, it is worthy of acceptance.

Professor Thomas D. Sewell

Professor Donald L. Thompson

Professor John E. Adams

Professor Carol A. Deakyne

Professor Stephen A. Montgomery-Smith

Acknowledgements

I would like to thank the following people, all of whom contributed in no small way to me being where I am today:

My parents, Mike and Judy Eason, obviously deserve the largest amount of thanks. They always pushed me to set high standards and to constantly be better than good enough. Without their constant support I would not have achieved even a fraction of what I have accomplished to this point.

I would like to thank all of my committee members in general for listening to my presentations, offering feedback, and challenging me with questions that forced me to critically think about the research I was doing. Individually, a thanks is due to Dr. Adams and Dr. Deakyne for being excellent teachers and always ready to answer a question regardless of whether I was a student of theirs or not. Thank you to Dr. Montgomery-Smith for making math so interesting that I wanted to sit in his classes just to hear him lecture. Thank you to Dr. Thompson for playing quite a large role in me considering graduate school and in my acceptance at Mizzou; and for helping me to quickly learn that giving facile answers to hard questions is not an option.

Two individuals from my undergraduate studies at Union University deserve special mention. Dr. Charles Baldwin, who originally lit the fire under me to be more than just an average student. Dr. Michael Salazar, without whom it is doubtful that I would have ever attended graduate school. Even near the end of my undergraduate studies I still wasn't quite certain what I planned to do for a career. Dr. Salazar made me

realize how much I enjoyed Physical Chemistry and provided the inspiration for me to pursue an advanced degree in the field.

No student who goes through graduate school in the Chemistry Department would survive without the assistance of Jerry Brightwell. I long ago lost count of the number of times he has taken care of paperwork or administrative issues for me. Thank you Ali Siavosh-Haghighi for answering all of my dumb computer related questions when I first started doing research. Thanks to Jamin Perry for providing countless hours of discussion throughout graduate school.

It is always customary to thank one's graduate advisor but in this case a simple thank you does not feel sufficient. Outside of my parents, I don't believe any person has had more profound of an impact on my life than Dr. Thomas Sewell. I could not have asked for a better mentor for my journey through graduate school. I will always be grateful for the lessons I learned from him and in my professional career I already find myself applying the principles I learned from him.

TABLE OF CONTENTS

Acknowledgements	ii
List of Figures	vii
List of Tables	ix
Chapter 1: A Brief Introduction to Energetic Materials	1
1.1 Material Response	1
1.2. Energetic Materials	2
1.3 Shock Waves	4
1.3.1 Continuity Equations	4
1.3.2 Deformation	6
1.4 Historical Analysis and Data	9
1.4.1 Experimental Studies	9
1.4.2 Simulations	12
1.5 Predictive Capability Goals	14
1.6 Thesis Outline	16
Chapter 2: Molecular Dynamics: Basic Principles and Applications to the Study of Energetic Materials	20
2.1 Molecular Dynamics Methodology	20
2.2 Force Fields Overview	24
2.3 Potentials Used in This Work	27
2.3.1 RDX Force Field	27
2.3.2 PETN Force Field	34

Chapter 3: Shock-Induced Inelastic Deformation in Oriented Crystalline Pentaerythritol Tetranitrate (PETN)	42
3.1 Introduction	42
3.2 Methods	47
3.3 Results and Discussion for the 3D Systems	50
3.3.1 Relative Molecular Displacements	50
3.3.2 Spatial Profiles of Intermolecular and Intramolecular Temperatures	55
3.3.3 Dihedral Angle Distributions in Unshocked and Shocked Material	58
3.4 Results and Discussion for the Quasi-2D System	61
3.4.1 Relative Molecular Displacements in Regions A-D	64
3.4.2 Kinetic Energy Time Histories in Regions A-D	65
3.4.3 Rotational Order in Regions A-D	67
3.4.4 Time Scales for Re-Establishing the Maxwell-Boltzmann Distribution of Kinetic Energy Behind the Shock	70
3.5 Conclusions	76
Chapter 4: Molecular Dynamics Simulations of the Collapse of a Cylindrical Pore in the Energetic Material α-RDX	82
4.1 Introduction	82
4.2 Methods	90
4.3 Results and Discussion	94
4.3.1 Snapshots of Center-of-Mass Positions and Local Velocity Fields	94
4.3.2 Rotational Order During Collapse	101
4.3.3 Temperature and Longitudinal Pressure	107
4.4 Conclusions	114

Chapter 5: Conclusions and Future Work _____ **119**

Vita _____ 123

LIST OF FIGURES

Chapter 1

Figure 1.1 Example of the unit cell structure of a bcc atomic system_____8

Chapter 2

Figure 2.1 Molecular connectivity of a molecule of PETN_____25

Figure 2.2 Isothermal linear and volumetric compression curves of RDX calculated using the Smith Potential at $T = 298\text{K}$ _____31

Figure 2.3 Linear and volumetric coefficients of RDX obtained from NPT simulations at $P = 1$ atm compared to experimental values_____32

Figure 2.4 Hugoniot locus in the u_s - u_p plane for RDX shocked normal to (100)_____34

Figure 2.5 Isothermal linear and volumetric compression curves for PETN obtained from NPT simulations at $T = 298$ K_____37

Figure 2.6 Linear and volumetric coefficients of thermal expansion for PETN calculated from NPT simulations at $P = 1$ atm compared to experimental values_____38

Figure 2.7 PETN Hugoniot locus in the u_s - u_p plane at initial temperature $T_0 = 300\text{K}$ and pressure $P_0 = 1$ atm compared to experiment_____39

Chapter 3

Figure 3.1 Depictions of PETN crystal_____45

Figure 3.2 Relative molecular displacements at times of maximum compression_____52

Figure 3.3 Orthographic projections of the piston s and flexible slabs at the times of maximum compression in the 3D systems_____54

Figure 3.4 Instantaneous spatial profiles for intermolecular and intramolecular temperatures_____57

Figure 3.5 Distributions of CCON dihedral angles_____60

Figure 3.6 Distributions of CONO dihedral angles_____62

Figure 3.7 Orthographic projection of the piston and flexible slab for the quasi-2D shock at the instant of maximum compression_____	63
Figure 3.8 Relative molecular displacements for the quasi-2D [100] shock projected into the (001) plane at the time of maximum compression_____	65
Figure 3.9 Time histories of total kinetic energies, expressed in temperature units, for molecules determined to be elastically (blue) and inelastically (red) displaced at the time of maximum compression in the quasi-2D [100] shock_____	67
Figure 3.10 Time histories of the orientational order parameter $P_2(t)$ for molecules determined to be elastically (blue) and inelastically (red) displaced at the time of maximum compression in the quasi-2D [100] shock_____	68
Figure 3.11 Normalized histograms of atomic kinetic energies for [100]-shocked PETN material_____	73
Figure 3.12 Normalized histograms of molecular center-of-mass kinetic energies for [100]-shocked material_____	74

Chapter 4

Figure 4.1 An RDX molecule and snapshot of the molecular center-of-mass locations in the simulation cell prior to shock_____	92
Figure 4.2 Snapshots of molecular centers of mass and velocity fields during pore collapse at three instants of time for the $1.0 \text{ km}\cdot\text{s}^{-1}$ _____	95
Figure 4.3 Snapshots of molecular centers of mass and velocity fields during pore collapse at three instants of time for the $2.0 \text{ km}\cdot\text{s}^{-1}$ _____	98
Figure 4.4 Snapshots of molecular centers of mass and velocity fields during pore collapse at three instants of time for the $3.0 \text{ km}\cdot\text{s}^{-1}$ _____	100
Figure 4.5 Rotational autocorrelation functions during and after pore collapse_____	103
Figure 4.6 Rotational-vibrational temperatures just after pore closure and at the time of maximum compression_____	109
Figure 4.7 Spatial profiles of temperature and longitudinal stress parallel to the shock direction_____	111

LIST OF TABLES

Chapter 2

Table 2.1 Lattice parameters and volume for a single unit cell of RDX_____ 31

Table 2.2 Lattice parameters and volume for a single unit cell of PETN_____36

Chapter 4

Table 4.1 Rotational time constants for RDX_____105

Chapter 1: A Brief Introduction to Energetic Materials

1.1 Material Response

A detailed understanding of how a material responds to some external stimulus is necessary to fully understand how that material functions. Responses to strong stimuli are generally complex processes involving chemical, mechanical, and thermodynamic changes to the system. Here, a mechanical response refers to an applied force producing a change in the structure of the material through non-chemical rearrangement of the constituent atoms and molecules. The thermodynamic response involves the conversion of mechanical energy to thermal energy, or heat, along with how the thermal energy is distributed throughout the material. Chemical response refers to the redistribution of electrons among atoms along with the associated breaking and forming of bonds. These responses are by no means independent from each other but instead are highly interconnected with one response type affecting all others in some manner.

Information on material response is vital in a variety of fields. Prescription medications are pressed into pellets at high pressures; therefore, an understanding of the response of the molecules is required to ensure that there is not a change in the structure of the active ingredients. Hoses in automobiles are made of rubber compounds that are composite materials consisting of polymer, fillers, plasticizers, and special purpose ingredients. The rubber materials are subjected to high temperatures and aggressive fluids; the engineer must be certain that the hose will maintain its integrity in this extreme environment. Explosives are extremely energetic and potentially dangerous materials that are also a composite material. A thorough understanding of how an explosive responds to

stimulus is vital to the evaluation of the safety and performance of that explosive. This work will be concerned with the primary energetic ingredients in explosives and the response of these ingredients to strong impacts.

1.2 Energetic Materials

Energetic materials (EM) are the key active ingredients in explosives responsible for the signature energy release achieved upon detonation. The typical EM is usually an organic crystal that often contains some type of nitro functionality. Some examples of energetic materials are pentaerythritol tetranitrate (PETN), hexahydro-1,3,5-trinitro-1,3,5-s-triazine (RDX), octahydro-1,3,5,7-tetranitro-1,3,5,7-tetrazocine (HMX), 2,4,6-trinitrotoluene (TNT), and 2,4,6-triamino-1,3,5-trinitrobenzene (TATB). Explosive formulations are usually a composite material consisting of energetic materials, plasticizers, bonding agents, and fillers. The term plastic bonded explosive (PBX) is often used to label these composite materials. Explosives are often divided into two classes based on sensitivity: primary and secondary. Primary explosives require only a very small amount of external stimulus and are initiated fairly easily. Secondary explosives are less sensitive than primary explosives and require a greater amount of stimulus to initiate detonation. Energetic materials are distinguished by the fact that they store large amounts of potential energy in conjunction with the capability to release this stored energy very rapidly. Release of stored potential energy occurs when detonation is initiated in the material.

Detonation in an EM is often initiated by generation of a shock wave that travels through the material causing mechanical deformations and large jumps in the

Chapter 1: A Brief Introduction to Energetic Materials

thermodynamic properties, including temperature and stress. Sufficiently high temperatures and stresses can cause chemical reactions that lead to a detonation wave in the material.¹ The initiation-to-detonation transition in EMs is an extremely complex process that is not currently fully understood. A better understanding of EM shock response would lead to safety and performance improvements during real-world applications of explosives.

The very characteristics that make energetic materials useful also serve to impede easy access to a complete understanding of the initiation-to-detonation process. Initiation processes occur across extremely small spatial and temporal scales, angstrom distances and femtosecond times, which are difficult to satisfactorily resolve with currently available experimental techniques. Further complications arise due to the destructive effect associated with energy release that makes analysis difficult. Thus, purely experimental methods are not able to provide the full range of information needed to achieve a complete understanding of detonation.

Computer simulations are able to augment experimental data by examining shock wave phenomena on spatial and temporal scales that are difficult to resolve through experimental methods alone. Simulations at the mesoscale (0.1 – 1,000 μm) make use of hydrodynamic simulation codes to model an energetic material as a continuum system. Hydrocodes require an equation of state for the reactants and products to predict thermo-mechanical properties in a sample of material. Even smaller than the mesoscale is the atomic scale, which is within the domain of Molecular Dynamics (MD) simulations. Molecular dynamics simulations use classical equations of motion to compute the

Chapter 1: A Brief Introduction to Energetic Materials

trajectories of the individual atoms, providing a time history of atomic positions and velocities from which various thermo-mechanical properties can be calculated.

There are different strengths and weaknesses associated with each method making the choice of appropriate method dependent upon the phenomenon of interest to be studied. The ideal goal is to combine information from simulations (both MD and hydrocodes) with experimental data to be able to describe all the dynamic processes from the microscale to the macroscale involved in the initiation-to-detonation transition in an energetic material. This work will focus on the application of molecular dynamics to the study of energetic materials and how this information contributes to the current knowledge base of energetic materials.

1.3 Shock waves

1.3.1 Continuity Equations

It is useful to establish some basic theoretical principles associated with the continuum description of shock waves in energetic materials. Once detonation is achieved in an energetic material, a shock wave travels through the material causing a change in the thermodynamic properties. Mathematically, a shock wave can be regarded as a discontinuity in the gradient of the flow variables (density, velocity, pressure, and energy). The jumps in the flow variables that occur across the discontinuity are described by the equations of continuity²

$$\rho_1 u_1 = \rho_0 u_0 \tag{1.1}$$

$$p_1 + \rho_1 u_1^2 = p_0 + \rho_0 u_0^2 \quad (1.2)$$

$$s_1 + \frac{p_1}{\rho_1} + \frac{u_1^2}{2} = s_0 + \frac{p_0}{\rho_0} + \frac{u_0^2}{2} \quad (1.3)$$

where ρ is the density, p is the pressure, u is the velocity, and ε is the internal energy. The subscript 1 denotes shocked material “behind the shock front” and the subscript 0 denotes un-shocked material “in front of the shock.”

It is possible to relate equations 1.1 – 1.3 to some useful physical explanations. Equation 1.1 is the conservation of mass which states that the mass flow into the discontinuity is equal to the mass flow out of the discontinuity. Equation 1.2 is the conservation of momentum flux density; simple rearrangement to

$$p_0 - p_1 = \rho_1 u_1^2 - \rho_0 u_0^2 \quad (1.4)$$

indicates that the change in momentum across a plane is due to the pressure on that plane. Equation 1.3 expresses the conservation of energy and states that the increase in the internal (ε) and kinetic ($u^2/2$) energies is due to the work done by the pressure forces.

Another useful equation is the Hugoniot relation which defines an equation of state for the energy as a function of pressure and specific volume on each side of the discontinuity. The Hugoniot is the locus of final states available to the system dependent upon the given initial set of conditions (pressure, density, volume). The Hugoniot energy equation is given by

$$s_1(p_1, V_1) - s_0(p_0, V_0) = \frac{1}{2}(p_1 + p_0)(V_0 - V_1) \quad (1.5)$$

The Hugoniot locus can be depicted in various forms but is often shown in the p - V plane or in the $u_s - u_p$ plane (or shock wave velocity and particle velocity plane). One is thus

Chapter 1: A Brief Introduction to Energetic Materials

able to predict the final shock wave velocity u_s when the initial particle velocity u_p is known. Another useful relation that can be derived from the Hugoniot equation is the Rankine-Hugoniot shock pressure

$$P_{RH} = \rho_0 u_s u_p \quad (1.6)$$

This relation allows determination of the shock pressure when one knows the initial density, initial piston velocity, and shock velocity.

Continuum scale computer simulations make use of the continuity equations and equations of state to propagate a system forward in time. However, MD simulations such as those performed in this work usually do not explicitly include the continuity equations in the propagation calculations (although mention must be made of special “Hugonostat” methods³⁻⁵ used in MD that drive the system to a specific point on the Hugoniot locus). Instead the importance of the continuity equations is realized during the post-simulation analysis of data where the shock wave produces much different properties in the shocked material compared to unshocked material.^{6,7} The effect of these jumps in temperature and stress on the molecular scale response of the material is the primary concern in this work.

1.3.2 Deformation

Strong stresses on a material can result in a structural rearrangement as the atoms or molecules undergo translational and orientational motion relative to each other; additionally, in the case of molecules, changes in molecular conformation can occur. At low stresses an elastic response is probable in which atoms will move closer or farther apart depending upon whether the stress is compressive or tensile in nature, respectively

Chapter 1: A Brief Introduction to Energetic Materials

(removal of the stress will result in atoms returning to their original lattice positions). Plastic, or inelastic, deformation occurs once enough stress is applied to the system to exceed the elastic limit. Plastic deformation is essentially an irreversible movement of atoms in the material (removal of the stress will not result in the atoms returning to their original lattice positions).

Deformation is affected by any pre-existing defects in the material that disrupt the perfect lattice structure. There are several types of defects that can occur, including but not limited to chemical impurities, vacancies, voids, interstitial atoms/molecules, stacking faults, grain boundaries, and dislocations.^{8,9} This work will primarily be concerned with dislocation defects that occur in previously defect-free crystals and with crystals that contain void regions. A vacancy defect is one in which a atom/molecule is missing from a lattice site. Void defects are volumes of space in the material where groups of atoms or molecules are missing. Dislocations are regions in the crystal where planes of atoms or molecules are displaced from each other relative to the perfect crystal lattice structure. The glide of dislocations is referred to as slip, which occurs along a defined plane called the slip plane. A slip plane in conjunction with a slip direction defines a slip system. For example, refer to the simple representation of a body-centered unit cell in Figure 1.1. (A quick note on notation used here: Miller indices are used to label planes and directions, with parentheses indicating a general plane, e.g. (100), and brackets indicating a general direction, e.g. [100]. The Cartesian frame used in the studies here is such that [100] is parallel to x , [010] is parallel to y , and [001] is parallel to z . The notation for planes in our Cartesian reference frame is as follows: (100) is normal to the [100] direction, (010) is normal to the [010] direction, and (001) is normal to the [001] direction.) The plane

defined by AEFD would be a slip plane (100) and the line defined by OB [010] would be a slip direction; in this case the slip system would be labeled as (100)[010] where (100) is the general slip plane and [010] is the general direction this plane slides along. The available slip systems in an energetic material play a large role in determining the shock response of that material.^{10,11}

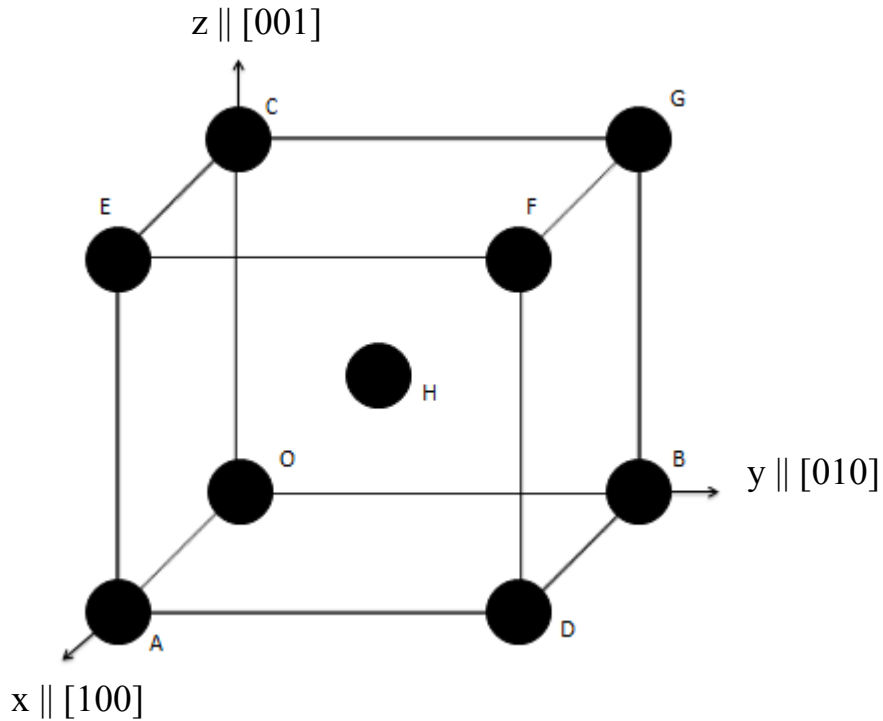


Figure 1.1 Example of the unit cell structure of a bcc atomic system. Cartesian x , y , and z axes are defined for reference along with parallel Miller indices directions. Atom H is at the center of the cell.

The process of plastic deformation in metals and simple ionic systems has been extensively studied and is well characterized.^{8,9} The independent slip systems and threshold energies needed to induce deformation have been determined for many of these systems.¹²⁻¹⁵ These processes are not currently as well understood for organic crystals

such as energetic materials due in large part to a much more complicated lattice structure. Even when considering materials that are not highly reactive, such as sucrose, there is still a gap in the knowledge base.¹⁶ Metals have only the $3N$ degrees of freedom associated with translational motion whereas organic crystals possess those $3N$ translational degrees of freedom along with far more additional degrees of freedom associated with rotational and vibrational motions of the molecules. Organic crystals have a more complex chemical environment with a variety of atom types containing different electronic structures which lead to more complicated particle-particle interactions.

1.4 Historical analysis and data

1.4.1 Experimental

Much effort has been invested in the study of explosives since even the early discovery of the energetic effects of black powder centuries ago.¹⁷ An exhaustive list of even just the experimental work done over the past few decades is far beyond the scope of this work (see for example, SCCM proceedings¹⁸ and International Detonation Symposium proceedings¹⁹); instead mention will be made of some of the important studies that are relevant to the concepts explored in this work. The primary methods of experimental study have focused on the use of engineering-oriented techniques with the goal of characterizing sensitivity and performance of a given explosive.²⁰

Deformation processes play a key role in determining the sensitivity of explosives; therefore much emphasis is placed on understanding the localized plastic

Chapter 1: A Brief Introduction to Energetic Materials

response of energetic materials, especially in knowing the available slip systems for a given material. Hardness indentation methods in conjunction with topography techniques, such as atomic force microscopy, are often used to identify the dominant slip systems in crystals of energetic materials.²¹⁻²⁴ An indenter is pressed into a chosen surface orientation of crystal material producing a load-depth curve from which information about elastic-plastic response can be obtained. Scanning the indentation with a topography technique such as AFM provides information about the slip systems activated during plastic deformation from the indentation. For example, this method has been used to identify slip systems in two materials studied in this thesis, PETN and RDX.²⁵ Recently, nanoindentation has been combined with MD studies to obtain hardness values, elastic moduli, and dynamic coefficient of friction of deformation for various surfaces of RDX.²⁶

It was mentioned previously that explosives can be categorized as primary or secondary based on the relative sensitivity of the explosive. Special emphasis has been placed on learning what characteristics of a material determine sensitivity. Impact sensitivity is often assessed by drop weight tests in which a weight is dropped onto a sample of explosive with the height of the initial release point varied to obtain an H_{50} value (the height at which the impact triggers an observable decomposition of the explosive 50% of the time). Attempts have been made to correlate H_{50} values with some structural or chemical properties to understand what determines sensitivity in an energetic material. A few examples of properties for which this has been attempted include electrostatic potential,²⁷ oxygen balance and nitro group charge,²⁸ crystal size,²⁹ and bond dissociation energies.³⁰ Even though the drop weight tests can give a relative ranking of

impact sensitivity, the method is not without flaws. Mathieu³¹ points out the H_{50} values are sensitive to factors beyond just chemical composition and recommends gap tests as a more reliable measure of sensitivity, although the increased difficulty performing the test means less experimental information is available for analysis. The large amount of readily available H_{50} values means that much insight can still be gained by correlating structural and chemical properties to this relative sensitivity ranking.

Plate impact experiments are a technique where a thin sample of material is impacted with a flyer plate in order to generate a planar shock wave. This technique can then be coupled with other analysis methods to gather information on the shock response of the material. Velocity interferometer system for any reflector (VISAR) is a flyer plate method from which is obtained a profile of surface velocity as a function of time.³² The velocity profile can be used to obtain useful information, such as when a transition from an elastic wave to a plastic wave occurs in a shocked crystal,³² or to identify differences in the response of crystals that are shocked along different orientations.^{33,34} Examples of plate impact methods in conjunction with spectroscopy analysis include emission spectroscopy to determine decomposition pathways in shocked energetic materials,^{34,35} Raman spectroscopy to study phase changes in shocked crystals³⁶ and crystals compressed in a diamond anvil cell,³⁷ and ultrasound spectroscopy to determine elastic constants.³⁸

Special mention will also be made here of laser ignition of explosives. One of the weaknesses of experimental methods in general is their inability to resolve phenomena at the extremely small space and time scales on which initial chemical events occur. Laser shocks have emerged recently as a method to experimentally probe these small scales.³⁹

Chapter 1: A Brief Introduction to Energetic Materials

Initial work using laser shocks on metal films was able to produce shock wave rise times of less than 6.25 ps for shock fronts that were only a few tens of lattice spacings in length.⁴⁰ Subsequent studies have continued to resolve short time scale events in laser driven shocks on metal films.⁴¹

The works referenced in the preceding paragraphs are a very small sampling of the experimental data available for energetic materials. The studies mentioned here are intended as examples to highlight the ideas of sensitivity, deformation, and shock response which are of greatest concern in this work. The interested reader is referred to the reviews by Armstrong and Elban²³ and Bouma *et al.*⁴² for a more complete listing of experimental works.

1.4.2 Simulations

Most experimental studies are primarily engineering-based methods that determine properties on the macroscale; however, detonation is a multiscale process that includes these macroscale properties along with small spatial and temporal scale phenomenon that are currently beyond experimental capabilities to study (although the spectroscopy and laser-induced shocks discussed in the previous section are able to probe events on the Å length scale and ps time scale). Computer simulations have been used over the past several decades to explore these small space and time scales. As mentioned previously, the two primary methods of simulating shock in energetic materials are hydrodynamic simulations and molecular dynamics simulations.

Chapter 1: A Brief Introduction to Energetic Materials

Hydrodynamic simulations are continuum scale calculations that simulate explosives at length scales of mm or higher. Hydrocodes function by solving the conservation equations (1.1 – 1.3) along with an equation of state for the material. Input consists of constitutive properties that describe the material at the mesoscale.⁴³ The computational domain studied in such cases is usually on the mm scale, which is sufficient to describe a “representative volume element” of μm sized grains in a sample.⁴⁴ Specific mesoscale simulations that are relevant to PETN and RDX will be discussed in chapters 3 and 4. The interested reader is referred to the thesis of Handley⁴⁵ for an extensive list of background references on mesoscale simulations along with an outline of the structure of a typical hydrocode simulation. Additionally, Menikoff and Sewell⁴³ have described important constituent properties needed for mesoscale simulations along with methods for obtaining the properties.

Molecular dynamics simulations allow insight into events that occur on the atomic scale below the resolution of continuum-scale methods. Molecular dynamics simulations usually employ analytical potential functions to integrate Newton’s equations, providing particle time histories from which pertinent thermomechanical properties can be calculated.^{46,47} Molecular simulations have been employed in a variety of ways to study energetic materials. A few examples of atomistic simulations providing useful data include, spectroscopic analysis,⁴⁸⁻⁵⁰ nanoindentation simulations of RDX,^{26,51} melting of nitromethane,^{52,53} calculation of thermodynamic properties which can be used as input into mesoscale simulations,⁵⁴⁻⁵⁶ and structural properties such as phase changes⁵⁷ and conformational stability.⁵⁸

Chapter 1: A Brief Introduction to Energetic Materials

The first example of MD application to a shock-wave like phenomenon is attributed to a study of radiation cascade damage in 1960.⁵⁹ Holian contributed greatly to much of the pioneering early work on computer simulations of shock waves.⁶⁰⁻⁶³ The initial work consisted of shock waves in 1D chains⁶⁰ followed shortly thereafter by shocks in 3D systems.^{61,63} Good agreement was even found between the thermodynamic variables of an argon-like system calculated from MD and Navier-Stokes continuum mechanics.⁶²

The focus of the present studies is on shock waves in molecular energetic materials, a topic that has seen increased MD application over the past couple of decades as more powerful computational resources became available allowing for simulations employing more complicated molecular descriptions. An in-depth discussion of computer simulations of shock waves will be deferred to later chapters to place them in context of specific projects.

1.5 Predictive capability goals

The goal of energetic material research is centered on the ideas of safety and performance, in other words the development of explosives that are not easily triggered in accident scenarios and that reliably produce the desired energy release at the appropriate time following an intended stimulus. A prime example of increased safety and performance is the evolution of nitroglycerin usage when it was first developed.^{17,64} Pure nitroglycerin is extremely unstable and resulted in many deaths due to accidental detonation during handling. The development of blasting caps and mixing with diatomaceous earth produced the much safer material known as dynamite. This goal has

not changed for present-day explosive development and application. The desire is to eliminate unintentional detonation while at the same time still producing a strong energy release.

Some emphasis has been placed on engineering “designer explosives” through predictive capabilities.⁶⁵ The high cost associated with synthesizing candidate molecules and testing new formulations makes it desirable to be able to pre-screen materials to eliminate ones with no useful potential.^{65,66} An ideal explosive would be one that is extremely energy dense but relatively insensitive to detonation. A lot of work has focused on using data for existing energetic materials to search for a correlation between some physio-chemical property and sensitivity or energy release.^{28,31,65-67}

The structural characteristics of crystal shape and size have been shown to have an effect on the shock sensitivity of the energetic materials RDX, HMX, and CL-20.⁶⁷ Efforts have been made to correlate bond strengths with impact sensitivities but the accuracy of this method was limited.⁶⁸ Extension of this idea to using bond dissociation energies scaled by energy content, the ratio D/E_d , produced a better correlation with H_{50} impact sensitivity data.⁶⁶ Mathieu³¹ found that a slightly altered definition of the energy density as a per-atom density in place of volumetric density, along with a comparison to gap test threshold pressures, produced a much stronger correlation between bond energies and sensitivity.

1.6 Thesis Outline

Background information was presented in this chapter on important concepts needed to understand the function of energetic materials. Specifically, the importance of understanding the response of energetic materials, the challenges associated with obtaining that information, and the goal of enhanced predictive capability were all highlighted. The rest of this thesis will focus on the use of molecular dynamics simulations to gain insight into the mechanical response of shocked PETN and RDX at the atomic scale. Chapter 2 will discuss the method of molecular dynamics along with the details for application to PETN and RDX. In chapter 3, anisotropic shock deformation of PETN is studied in the context of explaining orientation-dependent detonation initiation thresholds observed in experimental studies. Shock induced void collapse as a potential source of hot spots in RDX is discussed in chapter 4. Chapter 5 will identify deficiencies in the current studies and possibilities for future work.

References

- (1) Menikoff, R. *Combustion Theory and Modelling* **2006**, *10*, 1003.
- (2) Zel'dovich, Y. B.; Raizer, Y. P. *Physics of Shock Waves and High-Temperature Hydrodynamic Phenomena*; Dover Publications, Inc., 2002.
- (3) Maillet, J. B.; Mareschal, M.; Soulard, L.; Ravelo, R.; Lomdahl, P. S.; Germann, T. C.; Holian, B. L. *Physical Review E* **2000**, *63*, 016121.
- (4) Ravelo, R.; Holian, B. L.; Germann, T. C.; Lomdahl, P. S. *Physical Review B* **2004**, *70*, 014103.
- (5) Bedrov, D.; Hooper, J. B.; Smith, G. D.; Sewell, T. D. *The Journal of Chemical Physics* **2009**, *131*, 034712.
- (6) Hardy, R. J. *The Journal of Chemical Physics* **1982**, *76*, 622.
- (7) Root, S.; Hardy, R. J.; Swanson, D. R. *The Journal of Chemical Physics* **2003**, *118*, 3161.
- (8) Hull, D.; Bacon, D. J. *Introduction to Dislocations*; Third ed.; Pergamon Press: New York, 1984.
- (9) Hirth, J. P.; Lothe, J. *Theory of Dislocations*; John Wiley & Sons: New York, 1982.
- (10) Groves, G. W.; Kelly, A. *Philosophical Magazine* **1963**, *8*, 877.
- (11) Kocks, U. F. *Philosophical Magazine* **1964**, *10*, 187.
- (12) Duesbery, M. S.; Vitek, V. *Acta Materialia* **1998**, *46*, 1481.
- (13) Ismail-Beigi, S.; Arias, T. A. *Physical Review Letters* **2000**, *84*, 1499.
- (14) Cawkwell, M. J.; Nguyen-Manh, D.; Woodward, C.; Pettifor, D. G.; Vitek, V. *Science* **2005**, *309*, 1059.
- (15) Bringa, E. M.; Caro, A.; Wang, Y.; Victoria, M.; McNaney, J. M.; Remington, B. A.; Smith, R. F.; Torralva, B. R.; Van Swygenhoven, H. *Science* **2005**, *309*, 1838.
- (16) Ramos, K. J.; Bahr, D. F. *Journal of Materials Research* **2007**, *22*, 2037.
- (17) Anderson, K. J. *MRS Bulletin* **1989**, *14*, 84.
- (18) In *2013 Shock Compression of Condensed Matter Conference Proceedings*; Collins, G., Moore, D. S., Yoo, C. S., Eds. Seattle, WA, 2013.
- (19) In *International Detonation Symposium Proceedings*.
- (20) Armstrong, R. W. *Rev. Adv. Mater. Sci.* **2009**, *19*, 13.
- (21) Ramos, K. J.; Hooks, D. E.; Bahr, D. F. *Philosophical Magazine* **2009**, *89*, 2381.
- (22) Elban, W. L.; Hoffsommer, J. C.; Armstrong, R. W. *J Mater Sci* **1984**, *19*, 552.
- (23) Armstrong, R. W.; Elban, W. L. *Materials Science and Technology* **2006**, *22*, 381.
- (24) Jing, Y.; Zhang, Y.; Blendell, J.; Koslowski, M.; Carvajal, M. T. *Crystal Growth & Design* **2011**, *11*, 5260.
- (25) Gallagher, H. G.; Halfpenny, P. J.; Miller, J. C.; Sherwood, J. N.; Tabor, D. *Philosophical Transactions of the Royal Society of London. Series A: Physical and Engineering Sciences* **1992**, *339*, 293.
- (26) Weingarten, N. S.; Sausa, R. C. *The Journal of Physical Chemistry A* **2015**, *119*, 9338.
- (27) Rice, B. M.; Hare, J. J. *The Journal of Physical Chemistry A* **2002**, *106*, 1770.
- (28) Cao, C.; Gao, S. *The Journal of Physical Chemistry B* **2007**, *111*, 12399.
- (29) Armstrong, R. W.; Coffey, C. S.; DeVost, V. F.; Elban, W. L. *Journal of Applied Physics* **1990**, *68*, 979.
- (30) Rice, B. M.; Sahu, S.; Owens, F. J. *Journal of Molecular Structure: THEOCHEM* **2002**, *583*, 69.
- (31) Mathieu, D. *The Journal of Physical Chemistry A* **2012**, *116*, 1794.
- (32) Barker, L. M.; Hollenbach, R. E. *Journal of Applied Physics* **1972**, *43*, 4669.
- (33) Hooks, D. E.; Ramos, K. J.; Martinez, A. R. *Journal of Applied Physics* **2006**, *100*, 024908.

Chapter 1: A Brief Introduction to Energetic Materials

- (34) Dang, N. C.; Dreger, Z. A.; Gupta, Y. M.; Hooks, D. E. *The Journal of Physical Chemistry A* **2010**, *114*, 11560.
- (35) Dreger, Z. A.; Gruzdkov, Y. A.; Gupta, Y. M.; Dick, J. J. *The Journal of Physical Chemistry B* **2001**, *106*, 247.
- (36) Patterson, J. E.; Dreger, Z. A.; Gupta, Y. M. *The Journal of Physical Chemistry B* **2007**, *111*, 10897.
- (37) Dreger, Z. A.; Gupta, Y. M. *The Journal of Physical Chemistry B* **2007**, *111*, 3893.
- (38) Schwarz, R. B.; Hooks, D. E.; Dick, J. J.; Archuleta, J. I.; Martinez, A. R. *Journal of Applied Physics* **2005**, *98*.
- (39) Bourne, N. K. *Proceedings of the Royal Society of London. Series A: Mathematical, Physical and Engineering Sciences* **2001**, *457*, 1401.
- (40) Gahagan, K. T.; Moore, D. S.; Funk, D. J.; Rabie, R. L.; Buelow, S. J.; Nicholson, J. W. *Physical Review Letters* **2000**, *85*, 3205.
- (41) Whitley, V. H.; McGrane, S. D.; Eakins, D. E.; Bolme, C. A.; Moore, D. S.; Bingert, J. F. *Journal of Applied Physics* **2011**, *109*.
- (42) Bouma, R. H. B.; van der Heijden, A. E. D. M.; Sewell, T.; Thompson, D. L. In *Numerical Simulations*; Awrejcewicz, J., Ed.; InTech: 2011, p 29.
- (43) Menikoff, R.; Sewell, T. D. *Combustion Theory and Modelling* **2002**, *6*, 103.
- (44) Baer, M. R. *Thermochimica Acta* **2002**, *384*, 351.
- (45) Handley, C. Numerical Modeling of two HMX-based plastic-bonded explosives at the mesoscale, St. Andrews University, 2011.
- (46) Allen, M. P.; Tildesley, D. J. *Computer Simulation of Liquids*; Oxford University Press: New York, 1987.
- (47) Frenkel, D.; Smit, B. *Understanding Molecular Simulation: From Algorithms to Applications*; First ed.; Academic Press: San Diego, 2002.
- (48) Strachan, A. *The Journal of Chemical Physics* **2004**, *120*, 1.
- (49) Piryatinski, A.; Tretiak, S.; Sewell, T. D.; McGrane, S. D. *Physical Review B* **2007**, *75*, 214306.
- (50) Pereverzev, A.; Sewell, T. D. *The Journal of Chemical Physics* **2011**, *134*, 014513.
- (51) Chen, Y. C.; Nomura, K. I.; Kalia, R. K.; Nakano, A.; Vashishta, P. *Applied Physics Letters* **2008**, *93*.
- (52) Agrawal, P. M.; Rice, B. M.; Thompson, D. L. *The Journal of Chemical Physics* **2003**, *119*, 9617.
- (53) Zheng, L.; Luo, S. N.; Thompson, D. L. *The Journal of Chemical Physics* **2006**, *124*, 154504.
- (54) Bedrov, D.; Smith, G. D.; Sewell, T. D. *Chemical Physics Letters* **2000**, *324*, 64.
- (55) Zaoui, A.; Sekkal, W. *Solid State Communications* **2001**, *118*, 345.
- (56) Sewell, T. D.; Menikoff, R.; Bedrov, D.; Smith, G. D. *The Journal of Chemical Physics* **2003**, *119*, 7417.
- (57) Munday, L. B.; Chung, P. W.; Rice, B. M.; Solares, S. D. *The Journal of Physical Chemistry B* **2011**, *115*, 4378.
- (58) Mathew, N.; Picu, R. C. *The Journal of Chemical Physics* **2011**, *135*, 024510.
- (59) Gibson, J. B.; Goland, A. N.; Milgram, M.; Vineyard, G. H. *Physical Review* **1960**, *120*, 1229.
- (60) Holian, B. L.; Straub, G. K. *Physical Review B* **1978**, *18*, 1593.
- (61) Holian, B. L.; Straub, G. K. *Physical Review Letters* **1979**, *43*, 1598.
- (62) Holian, B. L.; Hoover, W. G.; Moran, B.; Straub, G. K. *Physical Review A* **1980**, *22*, 2798.
- (63) Holian, B. L. *Physical Review A* **1988**, *37*, 2562.
- (64) Anderson, K. J. *MRS Bulletin* **1989**, *14*, 63.

Chapter 1: A Brief Introduction to Energetic Materials

- (65) Rice, B. M.; Byrd, E. F. C. *Journal of Materials Research* **2006**, *21*, 2444.
- (66) Fried, L. E.; Manaa, M. R.; Pagoria, P. F.; Simpson, R. L. *Annual Review of Materials Research* **2001**, *31*, 291.
- (67) van der Heijden, A. E. D. M.; Bouma, R. H. B.; van der Steen, A. C. *Propellants, Explosives, Pyrotechnics* **2004**, *29*, 304.
- (68) Politzer, P.; Murray, J. S. *Journal of Molecular Structure* **1996**, *376*, 419.

Chapter 2: Molecular Dynamics: Basic Principles and Application to Energetic Materials

2.1 Molecular dynamics simulations methodology

Molecular Dynamics is a simulation method in which particle motion is determined by the laws of classical mechanics.^{1,2} Particles are moved forward in time by a numerical integration scheme that solves the classical equations of motion in either Newtonian, Hamiltonian, or Lagrangian form; for example, the equation of motion in Newtonian form is

$$\vec{F} = m\vec{a} = -\nabla V. \quad (2.1)$$

Equation 2.1 is the essential requirement for calculating a classical trajectory. Starting with initial phase space coordinates (positions and momenta) and knowledge of the potential energy surface for a system of particles, one can use Equation 2.1 to calculate the forces on the particles and predict their phase space coordinates at some later time.

Trajectory integration is fundamentally solving an initial value problem by finite difference methods. There are a wide variety of finite difference algorithms available for solution of the differential equations such as predictor-corrector methods, the Runge-Kutta-Gill³ integrator, or various forms of the Verlet⁴ algorithm. There are many additional algorithms available to integrate equations of motion,^{5,6} with those listed providing a few of the more well-known and commonly used examples. When choosing an integrator, one desires a method that is both accurate and efficient. Accuracy refers to tracing a path through phase space as closely as possible to the true trajectory while efficiency refers to a low computational demand. All simulations performed in this work employed the velocity version⁷ of the Verlet algorithm, which has demonstrated both

accuracy and efficiency.⁸ Trajectory integration yields the phase space coordinates of the system as a function of time starting from a given set of initial conditions; from this data one can calculate thermal and mechanical properties relevant to the phenomenon being studied. Given access to forces, a molecular dynamics “experiment” can conceptually be thought to proceed in three major steps:

- 1) Initial conditions selection
- 2) Trajectory integration
- 3) Analysis

Initial conditions refers to the initial positions of atoms in space to define a simulation cell along with specification of appropriate parameters for running the simulation. For liquids, the construction can be crudely accomplished simply by random placement of particles inside the simulation cell at a density matching the liquid state, while taking care to prevent any atomic overlap. Simulation cell construction of a solid can be accomplished by taking the atomic coordinates of a single unit cell from crystallographic data and replicating additional unit cells along the crystal axes until the desired simulation cell dimensions are reached. Simulation cell edge lengths on the order of a few tens to hundreds of Å are sufficient for calculating elastic constants;^{9,10} lattice parameters and isothermal compression curves;¹⁰ examining vibrational mode excitation;¹¹ or studying stress-induced phase transitions.¹² Performing shock simulations requires sizes that are on the order of hundreds to thousands of Å to allow sufficient time for events such as deformation occurring behind the shock front to evolve.^{13,14}

Sizes on the order of thousands of Å on a side are the largest possible for molecularly complex substances with currently available computing power. These dimensions are much too small to be representative of real macroscopic materials. Periodic boundary conditions are used to partially overcome the problem of size limitations.¹ The constructed simulation cell is the central cell with replica images existing on a periodic lattice in three dimensions. If a molecule crosses one face of the cell a replica image molecule enters the corresponding face on the other side of the cell. In this manner a bulk macroscopic material is simulated. Careful consideration must go into any cell construction to avoid unrealistic artifacts in the results that are the product of the setup. For example, finite-size effects can occur when using simulation cell sizes that are too small even if PBCs are used. Initial atomic velocities must also be selected to go along with the Cartesian coordinates; a random sampling of velocities from the Maxwell distribution at the desired temperature is appropriate for initial assignment, though this is usually followed by some amount of equilibration. However, random velocity sampling is not appropriate for all simulations, for example, selective vibrational excitation, in which case a specific amount of energy is assigned to one or more specific local or normal vibrational modes.^{11,15-17}

An appropriate integration timestep Δt must be chosen to update the system from time t to $t + \Delta t$. The smaller the timestep the more steps required to advance the simulation by a given amount, which means more time-consuming force calculations must be performed. In this regard, the larger the timestep, the better. However, a timestep that is too large will not properly resolve the short time scale phenomena occurring in the simulation (e.g. X-H bond vibrations) and will result in inaccurate solutions to the

equations of motion. It is best to choose a timestep based on the highest frequency characteristic motion in the simulation. The highest frequency motion for all studies in this dissertation is the C-H bond vibration with a frequency of about 3000 cm^{-1} , which gives a vibrational period of about 11 fs. Thus, a timestep no greater than 1 fs is ever used in these simulations to allow for at least 10 timesteps per C-H vibrational period. Such a large timestep was only used for equilibration calculations. Smaller timesteps of 0.1 and 0.2 fs are used during the production segments of the simulations so that there are at least 50 timesteps per C-H vibrational period.

Construction of a simulation cell for a crystalline material using the previously described replication technique results in a perfect crystal with all atoms positioned at their lattice sites based on the reference structure. Finite temperature materials exhibit thermal fluctuations of molecular locations and orientations, and intra-molecular displacements. Thermal equilibration is performed on the simulation cell to obtain a sample more representative of the fluctuations at a given pressure and temperature. Equilibration is performed in a statistical mechanical ensemble¹⁸ appropriate for studying the process of interest. In a given ensemble certain external parameters are held constant while others are allowed to vary. The most commonly used ensembles used in the present studies are the *NVT* ensemble, the *NPT* ensemble, and the microcanonical (*NVE*) ensemble. (Note that the italicized letters denote parameters that are held constant. For example, *N* is the number of particles, *V* is the simulation cell volume, *P* is the simulation cell pressure, *T* is the temperature in the cell, and *E* is the total energy in the cell.)

Once a steady-fluctuating state corresponding to the thermodynamic conditions of interest has been achieved it is then appropriate to perform the production simulation.

Data for subsequent analysis is collected during this portion of the simulation to calculate properties of interest from the time-dependent position and velocity data. The details of data collection and analysis will vary depending on the problem being studied. These details will be provided where appropriate in later sections.

2.2 Force fields overview

Trajectory integration is carried out by calculating the forces on all atoms as a function of position to predict positions at some later time. Specification of initial Cartesian coordinates and velocities was summarized previously; determination of subsequent positions and velocities requires knowledge of the forces acting on each particle as a function of the relative positions of all particles in the system. From Equation 2.1 it is apparent that the forces on a particle can be calculated through the use of a potential function. A force field is essentially a mathematical representation of the potential energy surface for a system of interacting particles. The potential energy for each particle prescribes how that particle interacts with all other particles in the system.

Some of the earliest computer simulations using force fields for condensed phases were of simple atomic systems such as noble gases.^{4,19} The lack of molecular complexity for simple atomic systems makes describing the potential energy surface comparatively simple due to intramolecular many-body terms being unnecessary and the sufficiency, to a first approximation, of using simple pairwise terms to describe all interatomic interactions between the particles.

Molecular force fields require more complicated terms to describe particle interactions than do simple atomic systems due to the need to account for two- and many-body covalent intramolecular bonded interactions in addition to the non-covalent “non-bonded” interactions. Covalent (or bonded) interactions include covalent bonds, three-center angles, torsional angles, and improper dihedrals. The atoms and connectivity of a molecule of PETN are presented in Figure 2.1. As examples, the atoms labeled C1 and C2 define a chemical bond; C1, C2, and H7 define a three-body angle; the sequence C1, C2, O3, and N6 define a torsional angle. Improper dihedrals are generally defined to maintain planarity among a group of atoms and are measured as an out-of-plane wag. For example; the atoms O4, O5, and N6 define one plane while O3, N6, and O5 define another plane; the improper dihedral is the angle between these two planes.

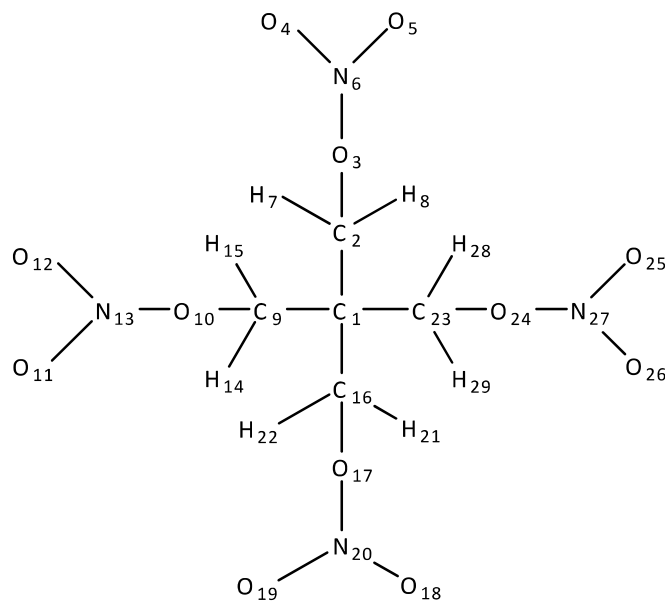


Figure 2.1 Molecular connectivity of a molecule of PETN. Note that the figure is not representative of the 3-dimensional spatial arrangement of PETN.

Non-bonded terms are needed to describe the interactions between atoms that are not connected by one of the previously described coordinate types. Examples of such non-bonded terms include Coulombic interactions between atomic partial charges and van der Waals interactions. Atoms N20 and O5 in Figure 2.1 are an example of atoms that are not directly bonded but potentially can still interact *via* non-bonded interactions. Typically, non-bonded interactions are applied to atoms in the same molecule but separated by three or more covalent bonds and to all atoms belonging to different molecules. The total potential energy for any given atom in the system (assuming no external forces) is then the sum of the bonded plus non-bonded terms

$$V_{\text{atom}}(r) = \sum V_{\text{bond}} + \sum V_{\text{non-bonded}} \quad (2.2)$$

Ideally, a developed force field would be parameterized in a manner that allows atoms of a given type to be transferred from one molecule to another with no loss of accuracy in the molecular description. One would then be able to more easily compare and contrast conclusions drawn from different molecular systems. Unfortunately, this cross-system generalization is not easily achieved due to the complicated, highly variable environments in molecular systems with different molecular flexibility, reactivity, and lattice structures. Attempts have been made to develop generalized force fields, in some cases including chemical reactivity, such as CHARMM,²⁰ AIREBO,²¹ and ReaxFF²² that can be applied to any number of different molecular systems with varying degrees of success. However, the general nature of these force field results in difficulties describing the complex physics and chemistry that occur over the wide temperature and pressure ranges that are often of interest for energetic materials.

Molecular force fields are usually developed by adjusting parameters in analytical potential functions to the results of quantum chemistry calculations, experiments, and using input from preceding force fields. These potential functions describe the bonded and non-bonded interactions in Equation 2.2 in various levels of detail. Typically, the required computational resources scale upward as the number of defined interactions increases since more time consuming force calculations are required. Molecular force fields can be non-reactive and rigid molecule, non-reactive and partially or fully flexible, or reactive; with the level of computational power increasing accordingly. The increase in computational resource demand with higher levels of detail is also due to more complicated functions being used to describe the forces on the particles. The bottleneck step in a MD simulation is the calculation of the forces. Thus, if the number of particle interactions that must be described by a potential function is increased then the computational cost of individual force calculations that must be performed per time step will increase resulting in an overall increase in the amount of computer time necessary for a simulation.

2.3 Potentials used in this work

2.3.1 RDX force field

This focus of the research presented here is simulations of shock waves in the energetic materials α -hexahydro-1,3,5-trinitro-1,3,5-s-triazine (RDX, see Figure 4.1) and pentaerythritol tetranitrate (PETN, see Figure 3.1). Therefore, potentials needed to be chosen that accurately describe these molecules at temperatures and pressures well away from standard ambient conditions of 300 K and 1 atm. All simulations of RDX performed

in this work used a fully flexible, non-reactive nitramine potential developed by Smith and Bharadwaj²³ (hereafter referred to as the “Smith potential”). The potential used for RDX was developed for another closely related energetic material, octahydro-1,3,5,7-tetranitro-1,3,5,7-tetrazocine HMX. The force field was developed by fitting parameters obtained from quantum chemistry calculations of molecular geometries and conformational energies to analytical potential functions. A special emphasis was placed on accurately reproducing dihedral displacements and out-of-plane deformations when parameterizing this force field. Partial atomic charges centered on the atoms were used to describe charge influenced interactions in the molecules. Bedrov *et al.*²⁴ validated the potential for HMX by calculating and comparing to experimental data the unit cell lattice parameters, coefficients of thermal expansion, and heats of sublimation; in addition, Sewell *et al.*²⁵ calculated the bulk modulus and elastic constants. Bedrov, Smith, and Sewell^{26,27} then employed the potential to calculate from simulations previously unreported values of the shear viscosity coefficient and thermal conductivity of liquid HMX.

Cawkwell *et al.*¹³ subsequently determined that RDX is also accurately described by the potential. Munday *et al.*¹² independently validated the use of the force field for RDX in simulations of the high-pressure phase transition between the α and γ crystal polymorphs. Precedence for the transferability of a potential between RDX and HMX had been previously established by Sorescu, Rice, and Thompson for the case of rigid molecules. They developed an intermolecular potential for RDX²⁸ described by pairwise Buckingham (exp-6) plus charges atom-atom interactions for prediction of condensed phase properties; follow-up studies found this potential to accurately predict the space

group and lattice parameters of HMX.²⁹ Given the structural similarities between HMX and RDX it is not surprising that the force fields are transferable; both molecules are heterocyclic rings containing the same nitramine (N-NO₂) group functionality with the difference being that HMX is an eight-member ring (a cyclic tetramer of CH₂N₂O₂) and RDX is a six-member ring (a cyclic trimer of CH₂N₂O₂).

The functional form of the potential used for both RDX and PETN is given by

$$U^{bond} = \frac{1}{2} k_{ij}^{bond} (r_{ij} - r_{ij}^0)^2 \quad (2.3)$$

$$U^{bond} = \frac{1}{2} k_{ijk}^{bond} (\theta_{ij} - \theta_{ij}^0)^2 \quad (2.4)$$

$$U^{torsion} = \frac{1}{2} k_{ijkl}^{torsion} [1 - \cos(n\varphi_{ijkl})] \quad (2.5)$$

$$U^{imp} = \frac{1}{2} k_{ijkl}^{imp} \delta_{ijkl}^2 \quad (2.6)$$

$$U^{NB} = A_{ij} e^{-B_{ij} R_{ij}} - \frac{C_{ij}}{R_{ij}^6} + \frac{q_i q_j}{4\pi\epsilon_0 R_{ij}} \quad (2.7)$$

where covalent bonds (eq. 2.3), three-body angles (eq. 2.4), and improper torsions (eq. 2.6) are approximated as harmonic oscillators; four-body dihedral angles are approximated by a sum of cosines (eq. 2.5); and non-bonded interactions are represented as a Buckingham plus Coulomb term (eq. 2.7).

This force field was implemented in the Large-scale Atomic/Molecular Massively Parallel Simulator (LAMMPS)³⁰ molecular dynamics code. LAMMPS is a large-scale parallel MD code that is free and open-source. A different functional form had to be used in place of Equation 2.5 for the force field implementation in LAMMPS. The functional form in Equation 2.5 is not present in the LAMMPS code therefore the function used was

$$U^{torsion} = \sum_{n=1,3} A_n \cos^{n-1}(\varphi), \quad (2.8)$$

where the force constants A_n in Equation 2.8 were solved in terms of the force constants k in Equation 2.5. The functional forms are equivalent.

Once the potential for RDX was chosen, it was necessary to validate the implementation of the force field in LAMMPS. For this purpose, unit cell lattice parameters (Table 2.1), isothermal compression curves (Figure 2.2), coefficients of thermal expansion (Figure 2.3), and the Hugoniot locus in the (shock velocity, particle velocity) plane (Figure 2.4) were calculated and compared to experimental data.

The calculated lattice parameters compare favorably to the experimental values reported by Choi and Prince,³¹ with the largest percentage error being about 2.4% in the a lattice parameter. All supercell constructions of RDX in this dissertation used our calculated lattice parameters of $a = 1.3498$ nm, $b = 1.1553$, and $c = 1.0564$ nm. The lattice parameter calculations in this research and by Cawkwell *et al.*¹³ were performed using the same force field in LAMMPS. The slight difference in values can be attributed to the fix npt settings used in LAMMPS. Cawkwell *et al.*¹³ used the *iso* setting in which all three diagonal components of the pressure tensor are coupled together (conditions of hydrostatic pressure); while this research used the *aniso* setting in which the three diagonal components are allowed to vary independently of each other using separate barostats for each.

Shock waves impose a strong uniaxial compression on the material, even “weak” shocks achieve pressures on the order of 1 – 2 GPa, (or about 10,000 – 20,000 atm) making it necessary to test the potential at high pressures. Isothermal compression curves were calculated up to pressures of about 9 GPa and are presented in Figure 2.2. There is good agreement between our curve and the experimental data of Olinger, Roof, and

Table 2.1 Lattice parameters (units of Å) and volume (units of Å³) for a single unit cell of RDX calculated at $T = 300\text{K}$ and $P = 1\text{ atm}$.

Lattice Parameter	Experiment ³¹	Cawkwell ¹³	This work	Percentage Error ^a
<i>a</i>	13.182	13.400	13.498	2.4%
<i>b</i>	11.574	11.517	11.553	0.2%
<i>c</i>	10.709	10.623	10.564	1.4%
<i>V</i>	1633.856	1639.424	1647.375	0.8%

a) Percentage error is between experimental values and this work and was calculated as

$$\% \text{error} = \frac{|\text{simulation} - \text{experiment}|}{\text{experiment}} \times 100$$

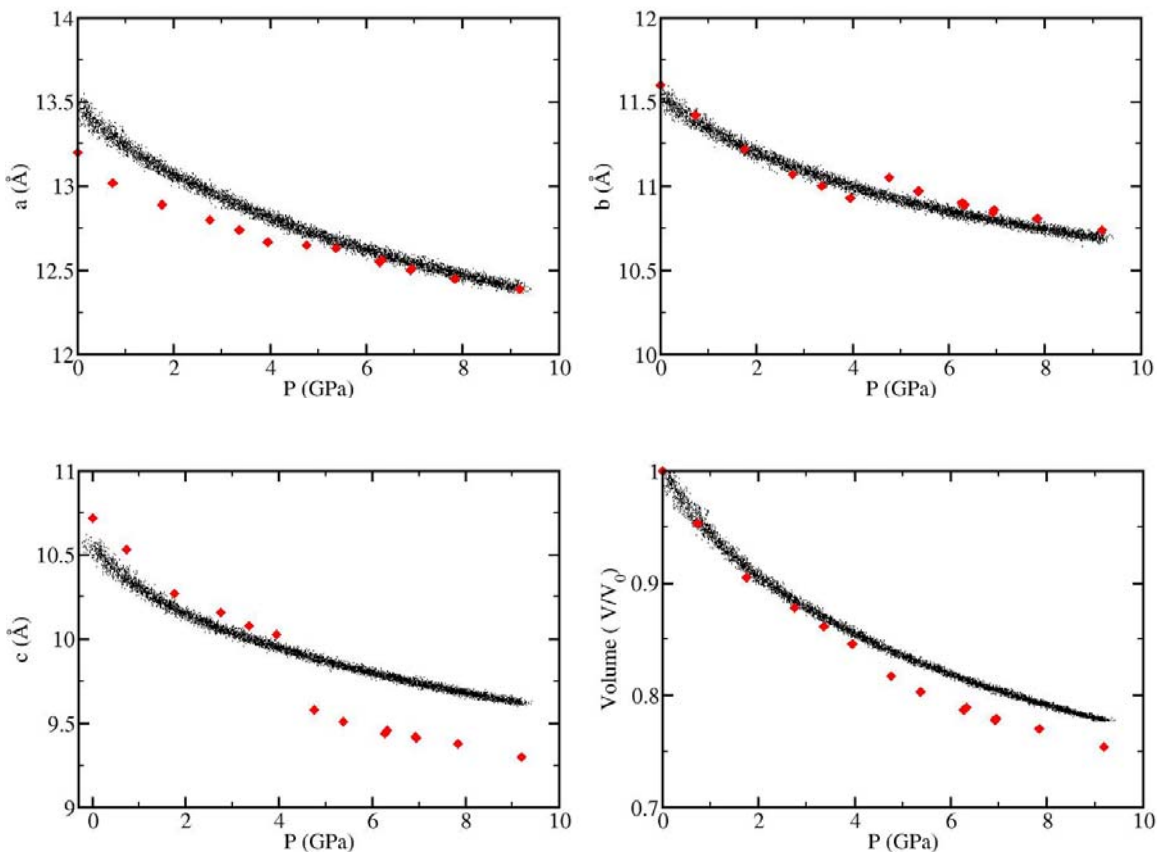


Figure 2.2. Isothermal linear and volumetric compression curves of RDX calculated using the Smith potential at $T = 298\text{ K}$. Black dots represent simulation data points while red diamonds are experimental data of Olinger, Roof, and Cady.³²

Cady.³² The discontinuity in the experimental compression curves at about 4.5 GPa is thought to be the result of a phase transition from α -RDX to γ -RDX.^{12,33,34} This phase transition is not observed in our hydrostatic compression simulations up to pressures of 9 GPa. Munday *et al.*¹² have also observed that the Smith potential does not reproduce the phase transition under hydrostatic compression but that it is observed during uniaxial compression along the c -axis and when depressurizing starting from the γ -polymorph. Considering that the Smith potential reproduces the phase transition under conditions of

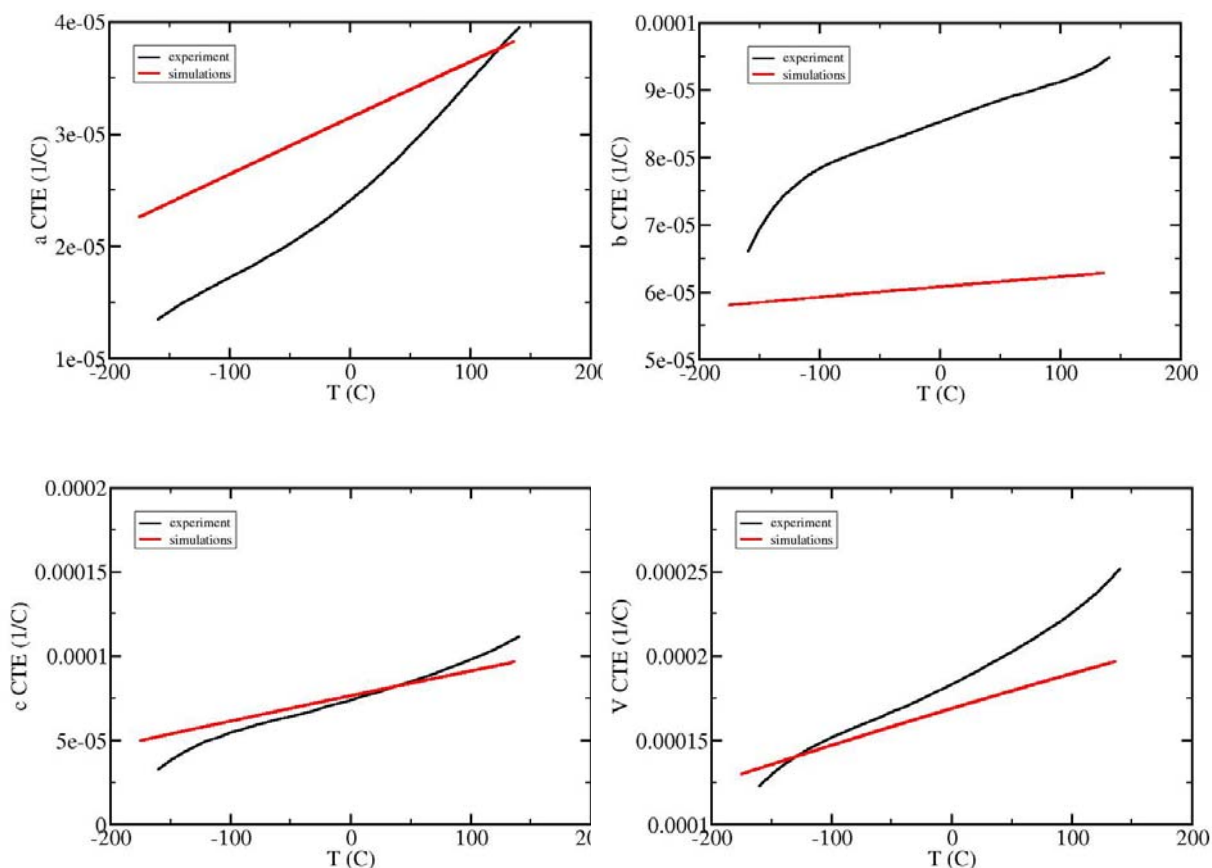


Figure 2.3 Linear and volumetric coefficients of thermal expansion for RDX obtained from NPT simulations at $P = 1$ atm compared to experimental values.³⁵

uniaxial compression and that the shocks studied in this research initially impart conditions of uniaxial compression, we are satisfied with the isothermal compression results from our simulations.

Linear and volumetric coefficients of thermal expansion were calculated and compared to experiment (Figure 2.3). The coefficient of thermal expansion ($\alpha = \frac{1}{V} \frac{\partial V}{\partial T}$) was calculated by performing an *NPT* simulation in which the temperature setting was increased at a constant rate to obtain the volume as a function of temperature. The volume was plotted versus temperature and the slope of the line was taken as dV/dT . Multiplying this slope by the reciprocal of the temperature-dependent volume produces the curves presented in Figure 2.3. The linear and volumetric coefficients of thermal expansion obtained from our simulations reproduce fairly well the experimental values.³⁵

The Hugoniot locus is presented in the u_s - u_p plane in Figure 2.4. As discussed in Chapter 1, the Hugoniot is the locus of final states available given an initial set of thermodynamic conditions. The result in Figure 2.4 is the shock wave velocity achieved given an initial piston velocity. The Hugoniot locus obtained from the simulations compares favorably to available experimental data.³⁶ In general, the agreement between thermo-mechanical properties calculated from our simulations and experiment, while not outstanding, is sufficient to give us confidence that the Smith nitramine force field was properly implemented in LAMMPS.

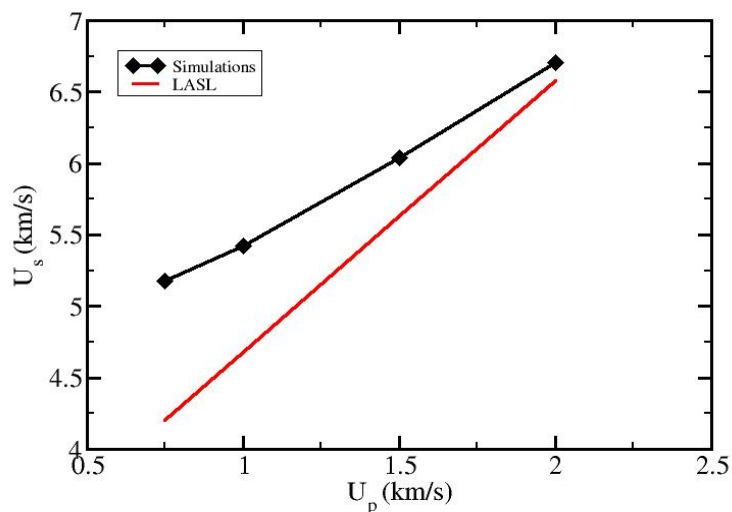


Figure 2.4 Hugoniot locus in the u_s - u_p plane for RDX shocked normal to the (100) plane. Initial Temperature $T_0 = 300$ K and Pressure $P_0 = 1$ atm. Red line is from *LASL Explosive Property Data*.³⁶

2.3.2 PETN force field

The principles applied in the selection and validation of a force field for RDX were also applied to PETN. Several force fields are available for PETN but Borodin *et al.*¹⁰ note that there are deficiencies in some predicted properties from these force fields, including the pressure dependence of unit cell lengths, heat of sublimation, heat of fusion, elastic constants, and bulk modulus. Borodin *et al.*¹⁰ developed a potential for PETN that overcame these deficiencies and could reliably be used for simulations of shock compression. This force field for the nitrate ester PETN uses the same functional forms to describe particle interactions as the nitramine force field²³ used for RDX and was developed using a similar methodology. Once again covalent bonds, three-body angles, and out-of-plane bends (improper dihedrals) are approximated as harmonic oscillators

while four-body dihedral angles are represented as a sum of cosine terms. Non-bonded interactions are also still approximated by a Buckingham-plus-Coulomb potential with fixed partial charges centered on the atoms. The form of the potential is the same as that in Equations 2.3 – 2.7, with the force constants and equilibrium distances now changed to parameterize conformational energies and molecular geometries of PETN. Borodin *et al.*¹⁰ validated the force field by calculating and comparing to experimental data the lattice parameters, isothermal compression curves, heat of sublimation and melting point, and the second-order elastic tensor.

The same thermodynamic and mechanical properties calculated to verify the RDX force field implementation were also calculated to validate the implementation of the PETN force field. The lattice parameters calculated from our implementation of the PETN force field are presented in Table 2.2. Note that PETN crystallizes into a tetragonal space group so that the a and b lattice parameters are equal to each other; therefore, only the a lattice parameter is usually reported. There is good agreement among parameters reported by the original force field authors,¹⁰ the experimental values,³⁷ and this work. All supercell constructions of PETN in this work used our calculated lattice parameters of $a = 0.9362$ nm and $c = 0.6847$ nm.

Isothermal compression curves up to 11 GPa calculated from our simulations are compared to those calculated by Borodin *et al.*¹⁰ and experimental values from Conant *et al.*³⁷ in Figure 2.5. Our results agree well with the experimental data and previous simulations, which gives confidence in the current implementation. A comparison of linear and volumetric coefficients of thermal expansion from our simulations and experimental data³⁵ is presented in Figure 2.6. Our values are in good agreement with the

experimental values for the temperature interval presented, indicating an accurate reproduction of the volume change as a function of temperature. Finally, the Hugoniot locus in the u_s - u_p plane is presented in Figure 2.7 where data from our simulations are compared to experimental data from Dick.³⁸ The good agreement indicates that the shock wave velocities produced in the present simulations are close to shock front velocities achieved for similar impact strengths in physical experiments on PETN.

Table 2.2 Lattice parameters for PETN (units of Å).

Lattice Parameter	Experiment ³⁷	Borodin ¹⁰	This work	Percent Error ^a
<i>a</i>	9.38	9.34	9.362	0.2%
<i>c</i>	6.71	6.86	6.847	2.0%
<i>V</i>	590.38	598.44	600.12	1.6%

a) Percentage error as defined in the footnote to Table 2.1

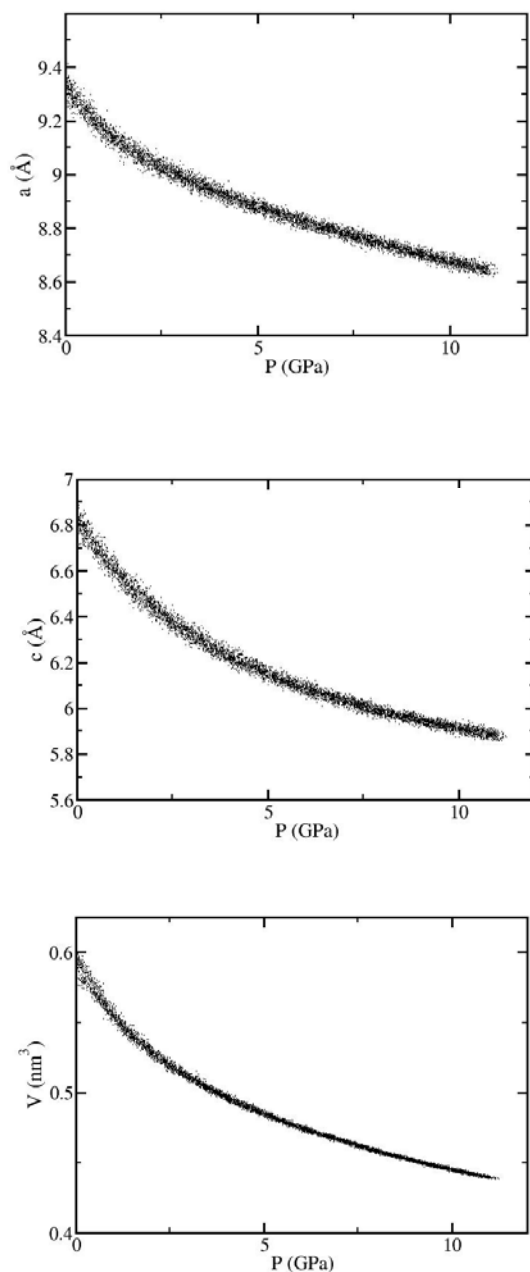


Figure 2.5 Isothermal linear and volumetric compression curves for PETN calculated from our simulations. at $T = 298$ K For reference, compare to curves calculated from experiment³⁹ and Borodin *et al*¹⁰ simulations.

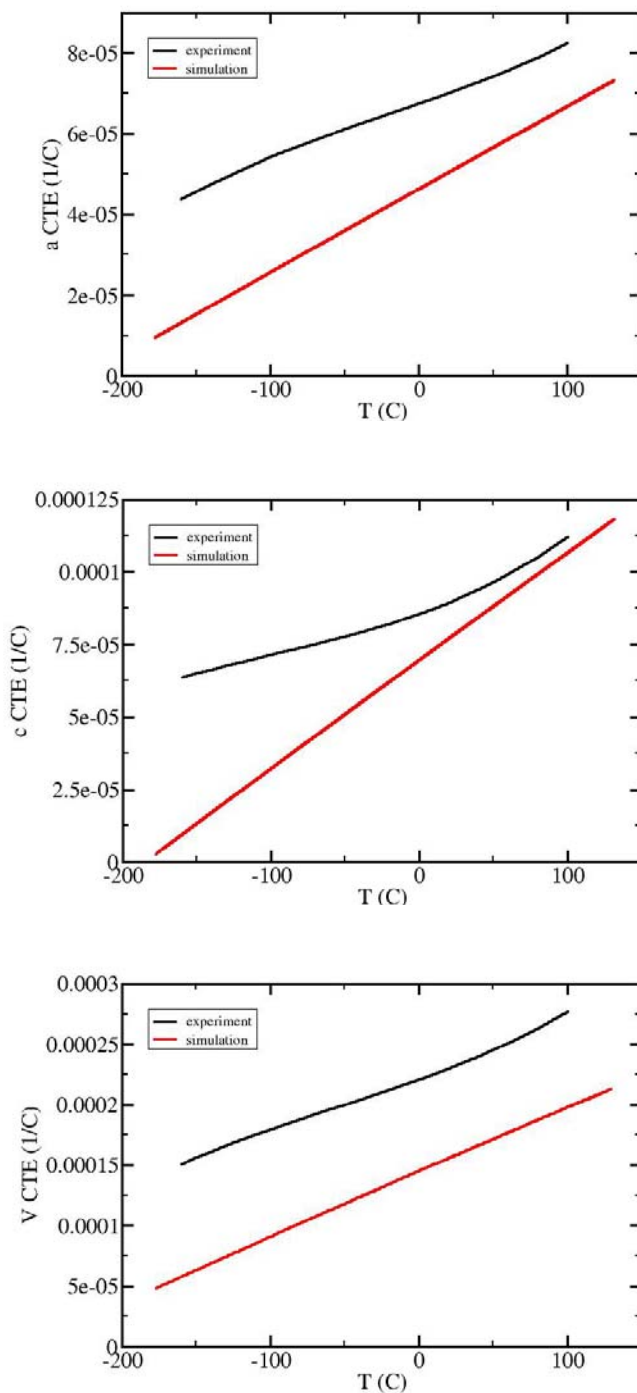


Figure 2.6 Linear and volumetric coefficients of thermal expansion for PETN calculated from NPT simulations at $P = 1$ atm compared to experimental values.³⁵

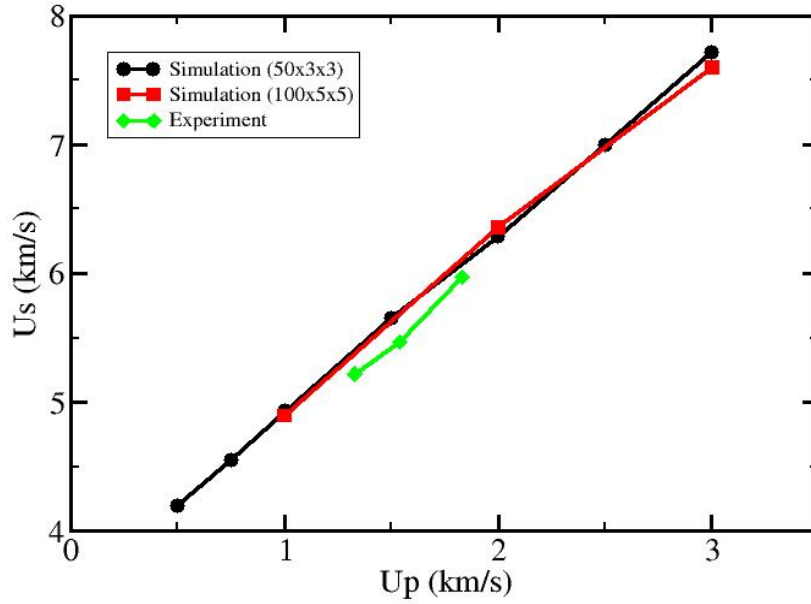


Figure 2.7 PETN Hugoniot locus in the u_s - u_p plane at initial temperature $T_0 = 300\text{K}$ and pressure $P_0 = 1$ atm compared to experiment.³⁸ All simulation data here was obtained from shocks traveling normal to the (100) plane. Here, $50 \times 3 \times 3$ and $100 \times 5 \times 5$ indicates the number of times the unit cell was replicated along the a , b , and c directions, respectively, to give the size of the computational domain.

References

- (1) Allen, M. P.; Tildesley, D. J. *Computer Simulation of Liquids*; Oxford University Press: New York, **1987**.
- (2) Frenkel, D.; Smit, B. *Understanding Molecular Simulation: From Algorithms to Applications*; First ed.; Academic Press: San Diego, **2002**.
- (3) Gill, S. *Mathematical Proceedings of the Cambridge Philosophical Society* **1951**, *47*, 96.
- (4) Verlet, L. *Physical Review* **1967**, *159*, 98.
- (5) Gear, C. W. *The Numerical Integration of Ordinary Differential Equations of Various Orders*, Argonne National Laboratory, **1966**.
- (6) van Gunsteren, W. F.; Berendsen, H. J. C. *Molecular Physics* **1977**, *34*, 1311.
- (7) Swope, W. C.; Andersen, H. C.; Berens, P. H.; Wilson, K. R. *The Journal of Chemical Physics* **1982**, *76*, 637.
- (8) Hairer, E.; Lubich, C.; Wanner, G. *Acta Numerica* **2003**, *12*, 399.
- (9) Sewell, T. D.; Bennett, C. M. *Journal of Applied Physics* **2000**, *88*, 88.
- (10) Borodin, O.; Smith, G. D.; Sewell, T. D.; Bedrov, D. *The Journal of Physical Chemistry B* **2007**, *112*, 734.
- (11) Pereverzev, A.; Sewell, T. D. *The Journal of Chemical Physics* **2011**, *134*, 014513.
- (12) Munday, L. B.; Chung, P. W.; Rice, B. M.; Solares, S. D. *The Journal of Physical Chemistry B* **2011**, *115*, 4378.
- (13) Cawkwell, M. J.; Sewell, T. D.; Zheng, L.; Thompson, D. L. *Physical Review B* **2008**, *78*, 014107.
- (14) He, L.; Sewell, T. D.; Thompson, D. L. *The Journal of Chemical Physics* **2011**, *134*, 124506.
- (15) Agrawal, P. M.; Thompson, D. L.; Raff, L. M. *The Journal of Chemical Physics* **1994**, *101*, 9937.
- (16) Rivera-Rivera, L. A.; Siavosh-Haghighi, A.; Sewell, T. D.; Thompson, D. L. *Chemical Physics Letters* **2014**, *608*, 120.
- (17) Rivera-Rivera, L. A.; Wagner, A. F.; Sewell, T. D.; Thompson, D. L. *Journal of Chemical Physics* **2015**, *142*, 1.
- (18) McQuarrie, D. A. *Statistical Mechanics*; University Science Books: Sausalito, CA, **2000**.
- (19) Rahman, A. *Physical Review* **1964**, *136*, A405.
- (20) Brooks, B. R.; Bruccoleri, R. E.; Olafson, B. D.; States, D. J.; Swaminathan, S.; Karplus, M. *Journal of Computational Chemistry* **1983**, *4*, 187.
- (21) Stuart, S. J.; Tutein, A. B.; Harrison, J. A. *The Journal of Chemical Physics* **2000**, *112*, 6472.
- (22) van Duin, A. C. T.; Dasgupta, S.; Lorant, F.; Goddard, W. A. *The Journal of Physical Chemistry A* **2001**, *105*, 9396.
- (23) Smith, G. D.; Bharadwaj, R. K. *The Journal of Physical Chemistry B* **1999**, *103*, 3570.
- (24) Bedrov, D.; Ayyagari, C.; Smith, G.; Sewell, T.; Menikoff, R.; Zaug, J. *Journal of Computer-Aided Materials Design* **2001**, *8*, 77.
- (25) Sewell, T. D.; Menikoff, R.; Bedrov, D.; Smith, G. D. *The Journal of Chemical Physics* **2003**, *119*, 7417.
- (26) Bedrov, D.; Smith, G. D.; Sewell, T. D. *The Journal of Chemical Physics* **2000**, *112*, 7203.
- (27) Bedrov, D.; Smith, G. D.; Sewell, T. D. *Chemical Physics Letters* **2000**, *324*, 64.
- (28) Sorescu, D. C.; Rice, B. M.; Thompson, D. L. *The Journal of Physical Chemistry B* **1997**, *101*, 798.
- (29) Sorescu, D. C.; Rice, B. M.; Thompson, D. L. *The Journal of Physical Chemistry B* **1998**, *102*, 6692.
- (30) Plimpton, S. *Journal of Computational Physics* **1995**, *117*, 1.

Chapter 2: Molecular Dynamics: Basic Principles and Application to Energetic Materials

- (31) Choi, C. S.; Prince, E. *Acta Crystallographica Section B* **1972**, *28*, 2857.
- (32) Olinger, B.; Roof, B.; Cady, H. H. In *Comportement des Milieux Denses sous Hautes Pressions Dynamiques*; Comisariat a l'Energie Atomique: Paris, **1978**.
- (33) Davidson, A. J.; Oswald, I. D. H.; Francis, D. J.; Lennie, A. R.; Marshall, W. G.; Millar, D. I. A.; Pulham, C. R.; Warren, J. E.; Cumming, A. S. *CrystEngComm* **2008**, *10*, 162.
- (34) Patterson, J. E.; Dreger, Z. A.; Gupta, Y. M. *The Journal of Physical Chemistry B* **2007**, *111*, 10897.
- (35) Cady, H. H. *Journal of Chemical & Engineering Data* **1972**, *17*, 369.
- (36) *LASL Explosive Property Data*; Gibbs, T. R.; Popolato, A., Eds.; University of California Press, Berkley, **1980**.
- (37) Conant, J. W.; Cady, H. H.; Ryan, R. R.; Yarnell, J. L.; Newsam, J. M. *The Atom Positions of Pentaerythritol Tetranitrate (PETN) Determined by X-Ray and by Neutron Diffraction*, Los Alamos National Labs, **1979**.
- (38) Dick, J. J.; Mulford, R. N.; Spencer, W. J.; Pettit, D. R.; Garcia, E.; Shaw, D. C. *Journal of Applied Physics* **1991**, *70*, 3572.
- (39) Olinger, B.; Halleck, P. M.; Cady, H. H. *The Journal of Chemical Physics* **1975**, *62*, 4480.

Chapter 3: Shock-Induced Inelastic Deformation in Oriented Crystalline Pentaerythritol Tetranitrate (PETN)^a

3.1 Introduction

Molecular energetic materials (EMs) are usually organic crystals with structures that often, but not always, contain nitro groups; for example, nitroaromatics, nitrate esters, and nitramines. They are the primary ingredient in propellant or plastic-bonded explosive formulations (PBXs), with the ideal PBX being one that combines high energy density with thermal and mechanical stability sufficient to render it safe to handle but sensitive enough to be reliably detonated under a well-defined mechanical stimulus.¹ The sensitivity of an explosive is closely related to its response to an applied dynamic or thermal stress. This response is strongly affected by material heterogeneities such as crystal defects or interfaces.²⁻⁴ Under dynamic load such heterogeneities can result in localized volumes of material with large thermal energies or high stress concentrations; these are referred to as *hot spots* and are generally thought to facilitate initiation and detonation of energetic materials.⁵⁻¹⁰

Responses to shocks can generally be classified as elastic or inelastic. An *elastic* deformation is one for which, neglecting the increase of temperature associated with the shock, an essentially reversible compression of the material occurs. *Inelastic* (or plastic) deformation involves an irreversible displacement or rearrangement of molecules in the material as a result of, for example, the glide of dislocations or shear band formation. The

a: Original publication – Eason, R.M., Sewell, T.D. *Journal of Physical Chemistry C* **2011**, 116, 2226

mechanisms of plastic deformation in crystalline metals are well understood both experimentally and theoretically.^{3,11-15} However, this knowledge is not as complete for organic crystals.¹⁶⁻¹⁸ Full understanding of the mechanisms of plastic deformation or other stress-induced changes in molecular materials is complicated by the presence of orientational (rotational) and internal (intramolecular) degrees of freedom that are not present in metals.¹⁹

There have been numerous theoretical studies of condensed phase energetic materials including nitromethane,²⁰⁻²⁸ octahydro-1,3,5,7-tetranitro-1,3,5,7-tetrazocine (HMX),²⁹⁻³³ hexahydro-1,3,5-trinitro-1,3,5-triazine (RDX),³⁴⁻⁴¹ 1,3,5-triamino-2,4,6-trinitrobenzene (TATB),^{42,43} and pentaerythritol tetranitrate (PETN),⁴⁴⁻⁵³ among others⁵⁴. These include studies based on static electronic structure,^{28,42,43,54} molecular dynamics (MD) simulations using empirical or electronic-structure-based force fields,^{23,27,55} and ones based on coarse-grained, particle-based methods.^{48,56,57} Recent review articles summarize much of this work.^{19,58} In the following we focus on MD simulations of mechanical deformation of energetic materials under dynamic loading.

Thompson and coworkers^{20,21} have developed a nonreactive, flexible-molecule force field for nitromethane for use in MD simulations. The force field has been validated against a wide variety of experimental data.^{20,59-61} Thompson and co-workers^{26,27} have used this force field to study structural relaxation and energy partitioning following shock excitation for seven different crystal orientations. Smith and Bharadwaj²⁹ (SB) have developed a fully-flexible, nonreactive force field for HMX that has been used to predict unit cell parameters, coefficients of thermal expansion, heats of sublimation,⁶² and elastic

Chapter 3: Shock-Induced Inelastic Deformation in Oriented Crystalline Pentaerythritol Tetranitrate (PETN)

properties³² of all three pure HMX polymorphs; and temperature-dependent thermal conductivity³⁰ and shear viscosity³¹ of the liquid. Jaramillo *et al.*³³ characterized the shock-induced plastic deformation in α -HMX at the atomic level by calculating relative nearest-neighbor molecular displacements and intramolecular and intermolecular temperatures. The SB HMX force field has been shown³⁶⁻⁴¹ to be transferable to RDX and has been used in several recent studies of the response of RDX to various kinds of mechanical loading.^{36,38,39} Cawkwell *et al.*³⁶ observed the formation of nanoscale shear bands for shocks propagating along [100]. They obtained radial distribution functions, rotational order parameters, and distributions of different intramolecular conformations to characterize the amount of shock-induced translational, orientational, and intramolecular disorder. Subsequently, Cawkwell *et al.*³⁸ and Ramos *et al.*³⁹ performed simulations for shock waves propagating normal to (111) and (021); they observed the homogeneous nucleation and spread of stacking faults above a well-defined shock threshold. The results of the (111) simulations were used to interpret an observed abrupt change in the shock response from a two-wave structure to a nearly overdriven response.³⁸ Based on the analysis of the (111) simulations Ramos *et al.*³⁹ predicted that a similar behavior should be expected for shocks in (021)-oriented RDX, a result that was confirmed experimentally.

Dick and coworkers^{44,63-65} have performed extensive studies on the shock loading of oriented single crystals of PETN (see Figure 3.1 for structure). In those studies it was observed that the threshold shock strength for initiation of detonation in PETN exhibits a strong dependence on the orientation of the crystal relative to the shock direction. The

material was found to be sensitive to shocks propagating along [110] and [001] directions but relatively insensitive to shocks propagating along any other direction studied.⁶³ Dick⁶⁴ proposed the *steric hindrance model* to explain this observed initiation anisotropy.

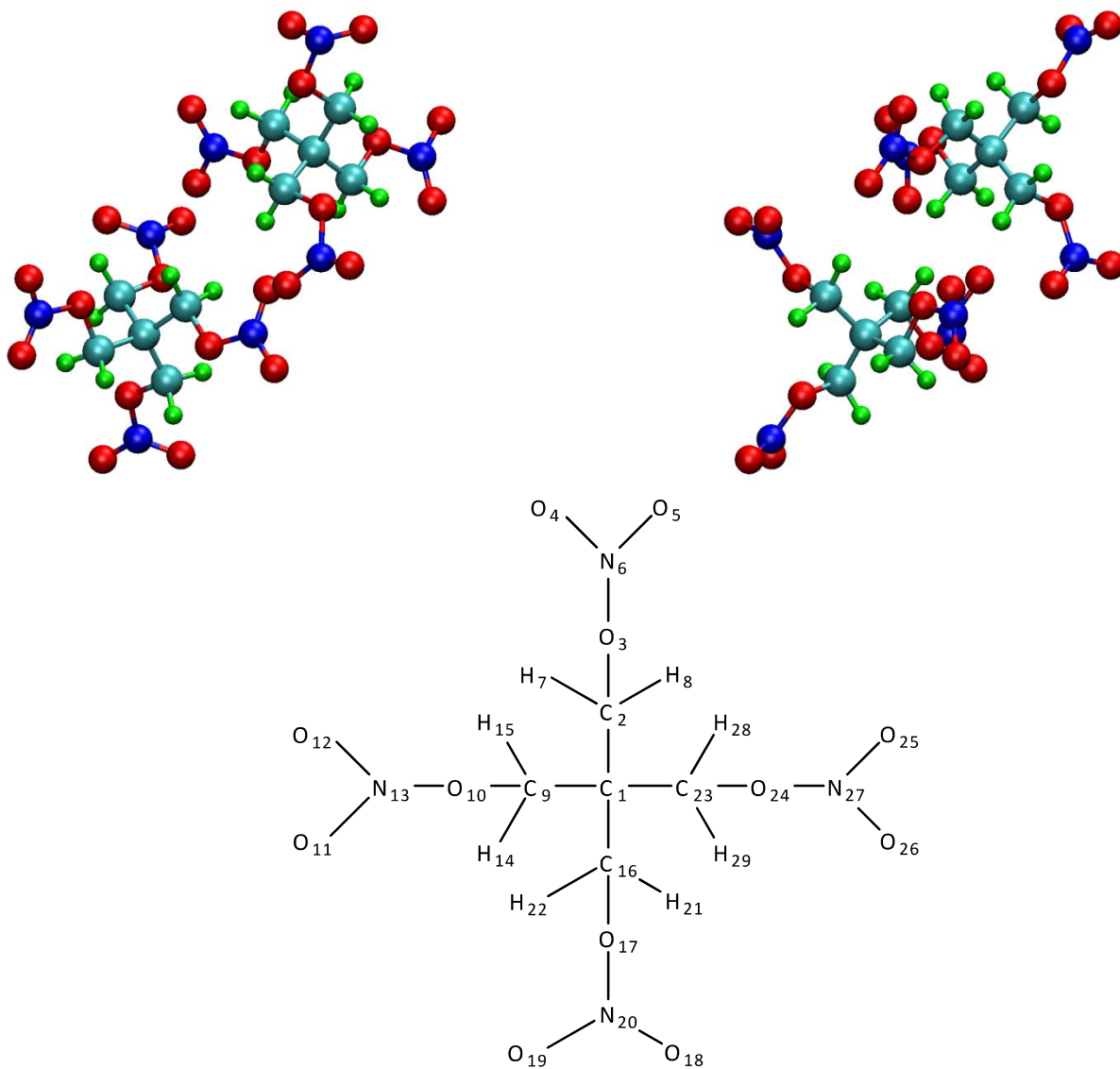


Figure 3.1. Depictions of PETN crystal. (a) Unit cell viewed down the [001] axis; (b) unit cell viewed down the [100] axis. Atoms colors are: carbon, cyan; nitrogen, blue, oxygen, red; hydrogen, green. (c) Covalent atomic connectivity and numbering scheme used in the simulations.

Chapter 3: Shock-Induced Inelastic Deformation in Oriented Crystalline Pentaerythritol Tetranitrate (PETN)

The steric hindrance model states that shock orientations insensitive to shock initiation in higher potential energy barriers compared to those for slip in insensitive directions. However, attempts to extend the steric hindrance model to other energetic materials have not been quite as successful.^{66,67} Cawkwell *et al.*³⁸ argued that PETN presents a special case due to its high symmetry compared to the other energetic materials that have been studied.

Subsequent studies on PETN have been performed to attempt to expand on the steric hindrance model originally proposed by Dick. Gruzdkov and Gupta⁴⁵ examined the polarity of the different molecular conformers that could possibly form as a result of shear stress along different directions. They proposed that shocks propagating along sterically hindered sensitive directions result in polar conformers that stabilize transition states, leading to increased reaction rates. They argued that because shear is not sterically hindered along insensitive orientations no polar conformations would result from shock passage.⁴⁵ Zybin and coworkers^{49,50} have used the ReaxFF reactive force field to determine the primary PETN reaction products resulting from shock compression⁴⁹ and rapid compression and shear.⁵⁰ They determined that breaking of the O-NO₂ bond to yield NO₂ is the principal primary reaction that occurs following strong shock loading along the [100] direction.⁴⁹ In the compress-and-shear simulations Zybin *et al.* first uniaxially compressed and then imposed large shear strains to activate potential slip systems corresponding to sensitive and insensitive orientations.⁵⁰ They observed a higher temperature and stress jump for the sensitive orientations that they attributed to the close intermolecular contacts that arise for those cases. Recently, ReaxFF has been used in

shock simulations of PETN containing spherical voids in which an enhanced chemical reactivity was observed compared to defect-free crystals.⁶⁸

In this chapter we report MD simulations of shock waves in crystalline PETN using a mechanically accurate but nonreactive force field.⁶⁹ The objective is to characterize in atomic detail the mechanical deformation processes that occur on ~ 20 ps time scales (shock propagation distances of ~ 0.1 micron) for supported shocks with Rankine-Hugoniot shock pressures $P_{R-H} \sim 9$ GPa. Simulations were performed for shocks propagating along [001] and [100] crystal directions, which are known experimentally^{63,64} to be, respectively, relatively sensitive and insensitive to shock initiation. The use of a nonreactive force field is justifiable given that, for shock input stresses comparable to those studied here, measured shock propagation distances required for detonation initiation are several millimeters.^{63,64}

3.2 Methods

All simulations were performed using the LAMMPS⁷⁰ code in conjunction with the nonpolarizable, nonreactive, flexible-molecule force field for alkyl nitrates developed by Borodin *et al.*⁶⁹ In this force field covalent bond stretches, three-center angles, and out-of-plane bends are approximated as harmonic oscillators; torsional motions are modeled using cosine expansions parameterized to reproduce energies and geometries for dihedral conformations obtained from quantum chemistry calculations; and nonbonded pair interactions, including intramolecular terms for atoms separated by three or more covalent bonds, are described by Buckingham-plus-Coulomb potentials with fixed partial

atomic charges located on the nuclei. The force field accurately predicts the lattice parameters and crystal structure, heat of sublimation and melting point, linear and volumetric isothermal compression curves, and the second-order elastic tensor at room temperature and atmospheric pressure.⁶⁹ The Borodin *et al.* force field was used without modification except that the particle-particle particle-mesh (PPPM⁷¹) algorithm was used with precision parameter 1×10^{-6} to evaluate both the electrostatic and the dispersion interactions; the cutoff distance for repulsive pair terms was 11.0 Å. Calculated lattice parameters for $T = 298$ K and atmospheric pressure are $a = b = 9.362$ Å and $c = 6.847$ Å, compared to the values $a = b = 9.34$ Å and $c = 6.86$ Å reported by Borodin *et al.*⁶⁹ and the experimental values⁷² $a = b = 9.3776$ Å and $c = 6.7075$ Å.

Simulations were performed for supported planar shock waves propagating parallel to [100] and [001] crystal directions, which correspond to insensitive and sensitive shock directions respectively.⁶³ Shock waves were generated using a reverse-ballistic configuration in which an oriented, thermally equilibrated crystalline slab of flexible molecules impacts from the right with impact speed $|U_p|$ onto a stationary, rigid piston comprised of crystalline material with the same orientation, initially commensurate with and contiguous to the flexible slab. Together the piston and flexible slab comprised 120 unit cells along the shock direction and 20 unit cells along the transverse directions; that is, supercell sizes of $120a \times 20b \times 20c$ for the [100] shock and $20a \times 20b \times 120c$ for the [001] shock. Hereafter we refer to these supercells as the *3D systems*. An additional shock along [100] was simulated using a supercell of size $120a \times 120b \times 6c$ (including

the piston); we refer to this supercell as the *quasi-2D system*. The computational procedure detailed below was applied consistently for all three simulations.

All trajectory integration was performed using the velocity Verlet integrator. Three-dimensional periodic boundary conditions were used in all cases; a 200 Å gap was introduced at the right-hand end of each system along the shock direction to minimize interactions between the left-hand end of the piston and the right-hand end of the flexible slab. Following introduction of the gap but prior to shock loading, equilibration of the entire system at $T = 298$ K was accomplished in two stages. First, five ps of isochoric-isoergic (NVE) trajectory integration was performed using a 0.5 fs time step during which the atomic velocities were scaled every 50 fs to yield the total kinetic energy predicted by classical equipartition, $E_k = 3N\kappa T/2$. Concurrently, completely new atomic velocities were selected every picosecond from the Maxwell distribution corresponding to $T = 298$ K; the purpose of this was to efficiently eliminate breathing motions parallel to the shock direction that resulted from introduction of the two free surfaces. Next, the system was simulated for 20 ps in the isothermal-isochoric (NVT) ensemble at $T = 298$ K using the Nosé-Hoover thermostat with a 0.5 fs time step and a thermostat relaxation time constant of 100 fs.

The shock simulations were performed in the NVE ensemble using a 0.1 fs time step. A rigid, stationary piston was created at the left-hand end of the system by setting to zero and fixing at zero the forces and velocities of all atoms in the first five unit cells along the shock direction. The remaining material comprised a flexible slab consisting of 92000 molecules for the 3D systems and 165600 molecules for the quasi-2D system. A velocity

$U_p = -1.0 \text{ km}\cdot\text{s}^{-1}$ along the shock direction was added to the thermal velocity of each atom of the flexible slab, leading to a shock wave propagating from left to right. Shock wave transit times across the flexible slab were approximately 22.0 ps and 16.0 ps, respectively, for the shocks propagating along [100] and [001]. Shock-front absorbing boundary conditions (SFABCs) as implemented by Cawkwell *et al.*³⁶ were used in the quasi-2D simulation to extend the total shock simulation time to 45.0 ps; the second piston required in the SFABC method was created from the region of the flexible slab corresponding to the five rightmost crystal unit cells along the [100] direction.

3.3 Results and Discussion for the 3D Systems

3.3.1 Relative Molecular Displacements

Inelastic deformation at the molecular scale was characterized by calculating relative displacements of nearest-neighbor molecular centers of mass using the method described by Jaramillo *et al.*³³. Relative molecular displacements (RMDs) are defined by:

$$\Delta_{ij}(t) = (r_{ij}(0) - \frac{l}{l_0} \hat{e}) - r_{ij}(t), \quad (1)$$

where i and j are first- and second-nearest-neighbor molecules in the unshocked tetragonal crystal structure; $r_{ij}(0)$ is the vector between centers of mass of those molecules at some reference time $t=0$, which we define as the time the shock wave was initiated in the flexible slab; and $r_{ij}(t)$ is the corresponding vector at some later analysis time t , which in the present study is the time of maximum compression. In order to accurately calculate Δ_{ij} it is necessary to account for the uniaxial compression of the material due to passage

of the elastic shock front. This was accomplished by determining the compression ratio l/l_0 along the shock direction and subtracting it vectorially from $r_{ij}(0)$; l/l_0 values for the [100] and [001] shocks were determined to be 0.797 and 0.799, respectively.

Components of the RMDs calculated at the times of maximum compression for the [001] and [100] shocks are shown in Figures 3.2(a)-(b) and 3.2(c)-(d), respectively. In all cases the abscissa corresponds to the shock direction. The two ordinates for a given shock correspond to the transverse directions; that is, the RMDs are projected into (010) and (100) planes for shocks propagating along [001], and (001) and (010) planes for shocks propagating along [100]. For shock propagation along [001] (Figures 3.2(a)-(b)) the RMDs in both planes cluster around zero, suggesting that only elastic compression has occurred in the material. By contrast, while [001] components of RMDs for the [100] shock are clustered relatively close to zero (Figure 3.2d), significant displacements are observed for [100] and [010] components (Figures 3.2(c)-(d)), meaning that relatively large translational displacements have occurred. Although the data in Figure 3.2c are noisy, they are predominately distributed along 45° angles relative to the shock direction and correspond to displacements in $\langle 110 \rangle$ crystal planes. Combined with the results in Figure 3.2d, we conclude that the dominant slip system activated for the [100] shock is $\{110\}\langle 1\bar{1}1 \rangle$. This is in agreement with the previous prediction by Dick and Ritchie⁴⁴ based on molecular mechanics simulations using the AMBER⁷³ force field.

The results in Figure 3.2 are consistent with expectations from the steric hindrance model.⁶⁴ For the impact strength considered, shocks along the sensitive [001] direction

do not activate any slip systems that would relieve the shear stress imparted by the shock (at least, not on the time scale and space scale of the present simulations, which were

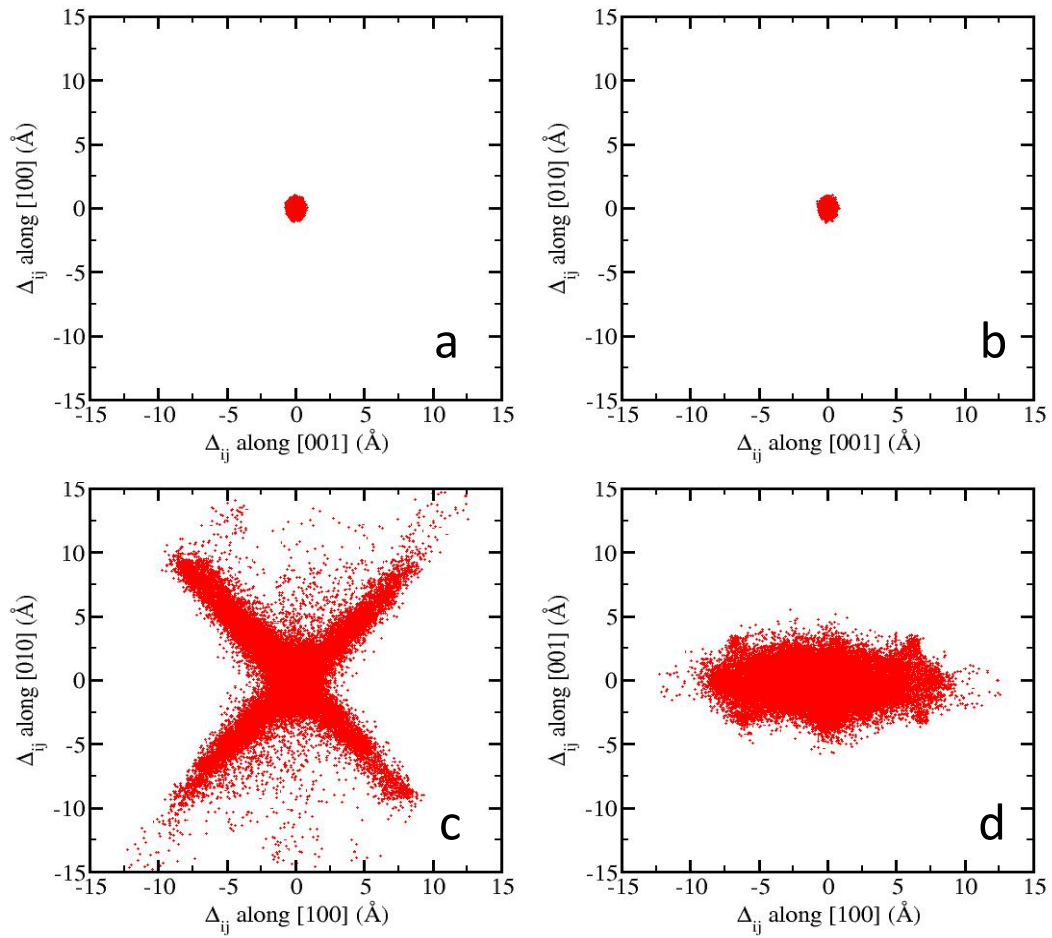


Figure 3.2. Relative molecular displacements at times of maximum compression. Panels (a) and (b): Projections into the (010) and (100) planes, respectively, for the [001] shock. Panels (c) and (d): Projections into the (001) and (010) planes, respectively, for the [100] shock.

performed for crystals with no pre-existing defects). Therefore, little or no inelastic deformation should occur, consistent with the results in Figures 3.2(a)-(b). By contrast, shocks along the insensitive [100] direction do activate a slip system that relieves the shock-induced shear stresses, leading to the inelastic deformation that is evident in Figures 3.2(c)-(d).

It is interesting to contrast the results obtained here with those reported by Jaramillo *et al.*³³ for (100)-oriented α -HMX shocked into the two-wave region. Specifically, whereas the results for (100)-oriented α -HMX exhibited clear localization of the molecular displacements that could be mapped to well-defined Burgers vectors $\frac{1}{2}[101]$ and $\frac{1}{2}[10\bar{1}]$, the wide spread of the molecular displacements in our calculations, while largely localized to $\langle 110 \rangle$ planes, does not allow unambiguous determination of a Burgers vector. This is discussed further in Sec. 3.4.1 in connection with results for the quasi-2D system.

The results of the RMD analysis provide a useful, albeit approximate basis for distinguishing molecules that have undergone only elastic compression from those that have undergone inelastic displacement. Specifically, based on the RMDs in a given plane at the time of maximum compression, individual molecules were classified as having undergone:

- (a) elastic compression if $r_{\Delta ij} < 2.15 \text{ \AA}$
- (b) inelastic displacement if $r_{\Delta ij} \geq 2.15 \text{ \AA}$.

Figure 3.3 contains snapshots of the 3D systems for [001] and [100] shocks (panels (a) and (b), respectively) at the times of maximum compression. Only molecular centers

of mass are shown. Elastically-compressed molecules are shown in blue while those deemed to have undergone inelastic displacements are colored red. Note that whereas for the [001] shock (Figure 3.3a) only elastic compression has occurred, for the [100] shock (Figure 3.3b) there are two distinct regions in the shocked material; a region of elastic compression immediately behind the shock front and a region further to the left in which plasticity is developing. Therefore, for the shock strength considered the (100)-oriented crystal is clearly in the two-wave elastic-plastic region of the shock Hugoniot locus. Because the two waves propagate at different speeds, it is not appropriate to regard as stationary a spatiotemporal reference frame centered on the shock front.

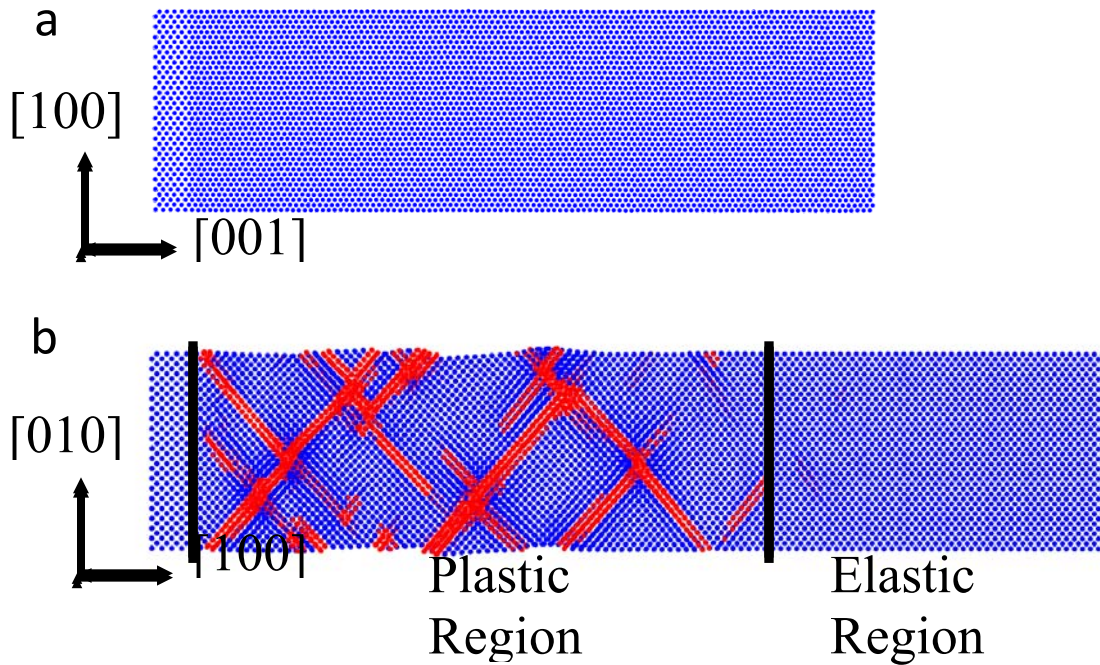


FIGURE 3.3. Orthographic projections of the pistons and flexible slabs at the times of maximum compression in the 3D systems. (a) [001] shock; (b) [100] shock. Only molecular centers of mass are shown. Elastically-compressed and inelastically-displaced molecules are colored blue and red, respectively

3.3.2 Spatial Profiles of Intermolecular and Intramolecular Temperatures

Spatially-resolved kinetic energies, expressed in temperature units for ease of presentation and henceforth referred to as temperatures (with reasonable justification, as discussed below in Sec. 3.4.4), were partitioned into translational and ro-vibrational components using the method due to Strachan and Holian.⁷⁴ The local velocity $\langle \mathbf{u} \rangle_i$ of a molecule i is defined in terms of its own velocity and the velocities \mathbf{u}_j of neighboring molecules and is given by

$$\langle \mathbf{u} \rangle_i = \frac{\sum_j w(r_{ij}) \mathbf{u}_j}{\sum_j w(r_{ij})} \quad (2)$$

The weighting function $w(r_{ij})$ is the same monotonically decreasing function of $r_{ij}=|r_i - r_j|$ as used by Strachan and Holian:⁷⁴

$$w(r) = \begin{cases} \frac{f(r)^4}{1 + f(r)^4} & \text{if } r \leq R \\ 0 & \text{if } r > R \end{cases} \quad (3)$$

where $f(R) = (r - R)/\sigma$. We used parameter values $R = 28.086 \text{ \AA}$ (three times the a unit cell length) and $\sigma = 0.9362 \text{ \AA}$ (one-tenth the a unit cell length) in eq 3. The local molecular velocity is then used to define an intermolecular temperature

$$\frac{3}{2} k \langle T \rangle_i^{\text{inter}} = \frac{\frac{1}{2} \sum_j M_j w(r_{ij}) |\mathbf{u}_j - \langle \mathbf{u} \rangle_i|^2}{\sum_j w(r_{ij})} \quad (4)$$

where M_j is the total mass of the molecule and k is Boltzmann's constant.

Intramolecular temperatures were calculated using the method originally described by Strachan and Holian⁷⁴ as implemented by Jaramillo *et al.*³³ The intramolecular temperature is given by

$$\frac{3}{2} N_i^{at} k T_i^{\text{intra}} = \frac{1}{2} \sum_{j=1}^{N_i^{at}} m_j (u_j - u_i^{c.m.})^2 \quad (5)$$

where N_i^{at} is the number of rotational and vibrational degrees of freedom, u_j is the velocity of atom j , and $u_i^{c.m.}$ is the center-of-mass velocity of molecule i containing atom j . The average local vibrational temperature in the neighborhood of molecule i is then given by

$$\langle T \rangle_i^{\text{intra}} = \frac{\sum_j w(r_{ij}) T_j}{\sum_j w(r_{ij})} \quad (6)$$

Instantaneous spatial profiles of the temperature measures defined in equations 4 and 6 are shown in Figure 3.4 at 5.0 ps intervals starting from $t = 0$. Results for the intermolecular and intramolecular temperatures for the [001] shock are shown in panels (a) and (b), respectively; corresponding quantities for the [100] shock are shown in panels (c) and (d). The rapid initial rise and subsequent decrease in intermolecular temperature (panels (a) and (c)) confirms expectations that energy from the shock wave is initially distributed principally among the lattice modes of the crystal. The intermolecular temperature for the [001] shock (panel (a)) decreases essentially monotonically toward the long-time value over a distance of approximately 650 Å. By contrast, the intermolecular temperature for the [100] shock (panel (c)) decreases from the maximum value associated with initial shock passage; reaches, for post-shock time $t = 20.0$ ps

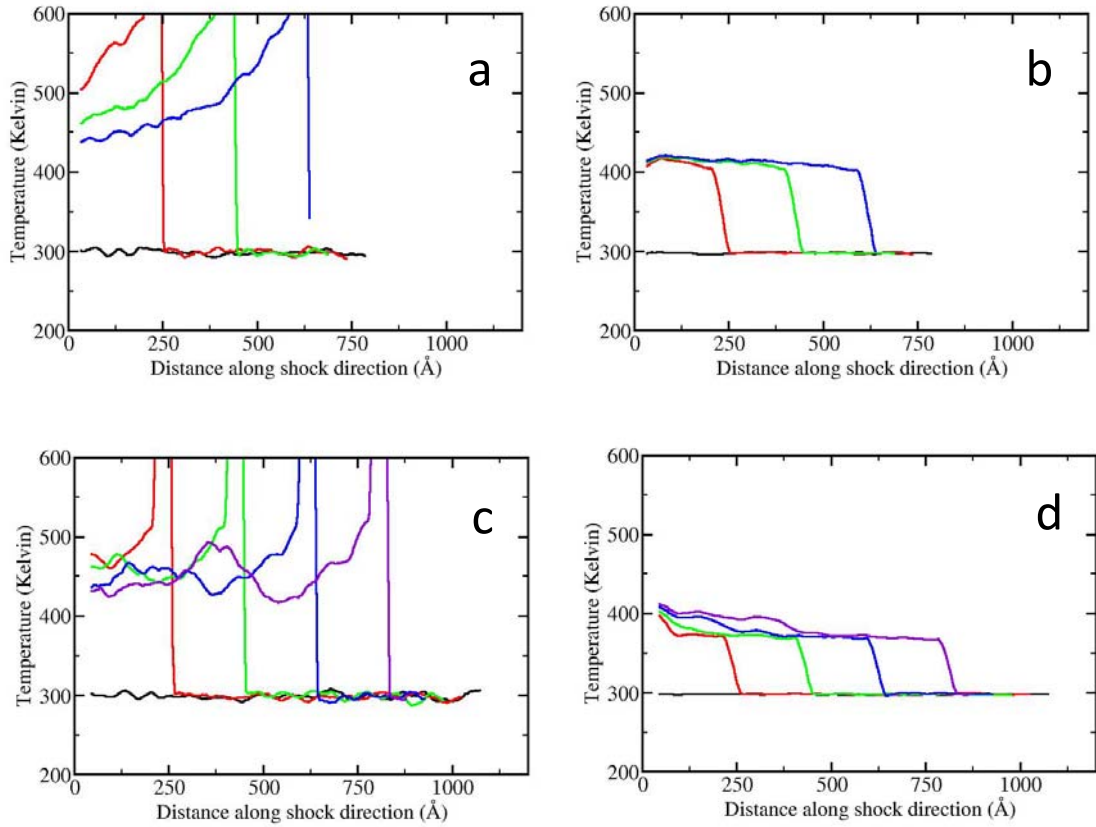


Figure 3.4. Instantaneous spatial profiles for intermolecular (eq 4, panels (a) and (c)) and intramolecular (eq 6, panels (b) and (d)) temperatures at 5.0 ps intervals starting from the time of shock initiation in the flexible slabs ($t = 0$). Panels (a) and (b): [001] shock; panels (c) and (d): [100] shock.

(purple curve), a local minimum at a distance about 300 Å behind the shock front; and subsequently exhibits an increase of ~ 75 K during evolution of the plastic wave. The intramolecular temperatures increase monotonically for both shock orientations; no transient excitation is observed. The intramolecular temperature for the [001] shock (panel (b)) exhibits an initial rise over a distance of approximately 50 Å with little

additional increase for increasing distances behind the shock front. The intramolecular temperature for the [100] shock (panel (d)) rises initially over a distance comparable to that for the [001] shock, although the value of the initial rise is about 30 K lower than that in the [001] shock. However, the intramolecular temperature for the [100] shock also increases during the evolution of the plastic wave such that the final intramolecular temperatures for the two shocks are nearly equal by the times of maximum compression. Note that complete equilibration between the intermolecular and intramolecular temperatures has not been established for either shock orientation by the respective times of maximum compression; in both cases the two temperature measures differ by 20-30 K. Overall, the qualitative features of the temperature profiles for the two shocks are consistent with the steric hindrance model, for which a split wave is anticipated in the [100] shock (insensitive orientation) but not in the [001] shock (sensitive orientation).

3.3.3. Dihedral Angle Distributions in Unshocked and Shocked Material

Distributions of CCON and CONO dihedral angles were calculated to assess the differences in intramolecular distortion caused by the shock waves; these internal coordinates are of particular interest due to the floppy nature of the PETN molecule (see Figure 1). There are four CCON and eight CONO dihedral angles per molecule. Results for the CCON and CONO dihedrals are presented in Figures 3.5 and 3.6, respectively. In both figures panel (a) corresponds to unshocked material and panel (b) to material in the [001] shock; panels (c) and (d) are for the [100] shock and correspond, respectively, to

elastically-compressed and inelastically-displaced molecules. Results in panels (b)-(d) were obtained at the times of maximum compression for the respective shocks.

The CCON dihedral angles are essentially *trans* in the unshocked crystal (peaks at $\pm 180^\circ$ in Figure 3.5a). Comparing panels (a) and (b), shock loading along [001] leads to modest splitting of the *trans* peak into two peaks with unequal amplitudes and shifted toward smaller angles by about 20° ; no new peaks emerge. Shocking along [100] leads to greater changes in the CCON dihedral distributions (panels (c) and (d)). The main peak still corresponds to the *trans* CCON dihedral both for the elastically-compressed and inelastically-displaced molecules (panels (c) and (d), respectively). In both cases new broad peaks emerge, centered about $\pm 90^\circ$; the amplitudes of these peaks for the inelastically-displaced molecules are much larger than for the elastically-compressed ones. Based on these results we conclude that the CCON dihedrals in [100]-shocked PETN crystal rotate with less hindrance than those in [001]-shocked crystal. The less hindered dihedral rotation about C-O bonds for shocks along the [100] direction compared to the [001] direction could play a role in facilitating slip in shocked (100)-oriented PETN as part of the mechanism for relieving the shock-induced shear stresses.

Each $\text{H}_2\text{C-O-NO}_2$ moiety in PETN has one *cis* and one *trans* CONO dihedral in the equilibrium crystal structure. Using the systematic atomic numbering scheme shown in Figure 3.1c these are readily distinguished as shown in Figure 3.6a, which contains independently normalized probability distributions for the *cis* and *trans* CONO dihedrals in the unshocked crystal. Shock loading along [001] has very little effect on the distributions at the instant of maximum compression (Figure 3.6b); the distributions are

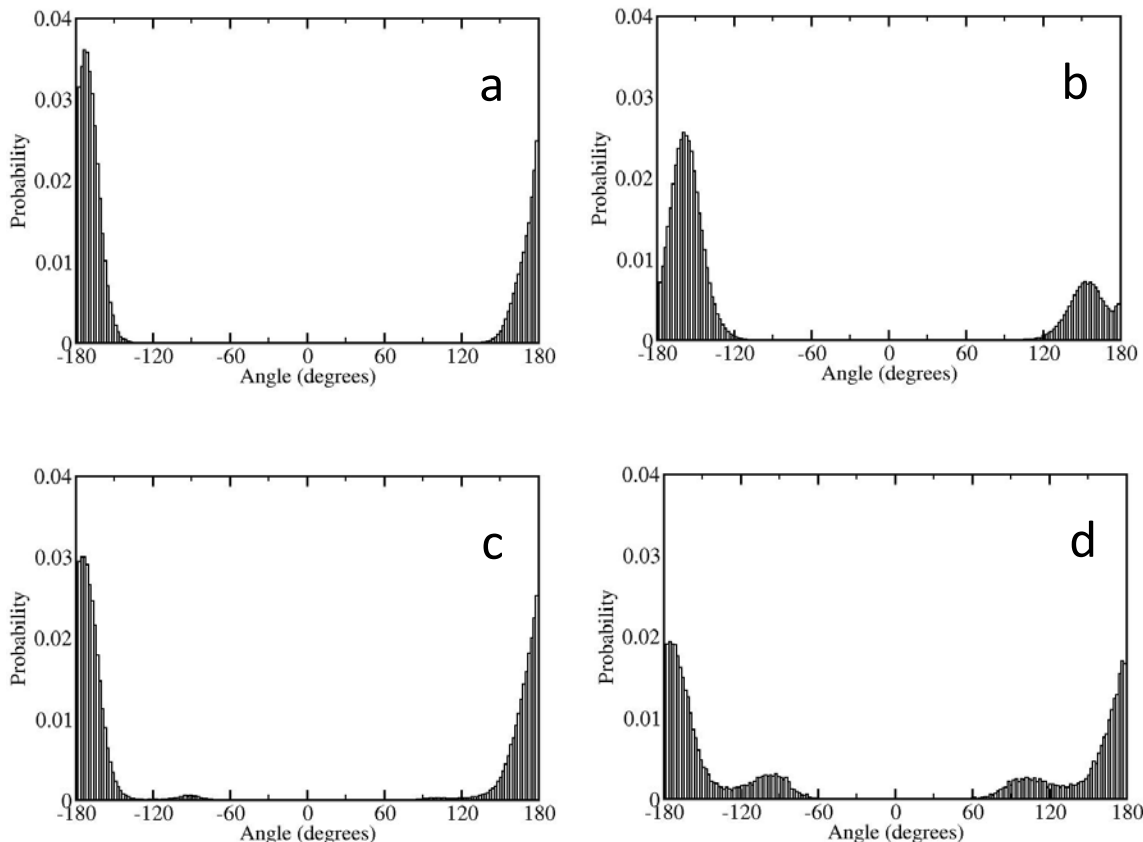


Figure 3.5. Distributions of CONO dihedral angles. (a) Unshocked material (equivalent for both shock orientations); (b) [001] shock; (c) and (d) [100] shock: molecules determined to have undergone (c) elastic compression and (d) inelastic displacement. Results in (b)-(d) correspond to instants of maximum compression in the respective simulations.

noticeably broadened, but all CONO dihedrals remain essentially *cis* or *trans* and there is no evidence for rotation of the NO₂ group. That is, there are no initially *cis* dihedrals that have become *trans* at the end of the simulation or *vice versa*. The situation is different for the [100] shock; while most CONO dihedrals at the time of maximum compression are

either *cis* or *trans*, the distribution exhibits nonzero probability for all angles in the domain. Moreover, a number of initially *trans* CONO dihedrals have become *cis* by the time of maximum compression and *vice versa*, indicating that NO₂ rotation does occur for molecules involved in inelastic deformation events.

3.4 Results and Discussion for the Quasi-2D System

Finite-size effects in the (001) plane are apparent in Figure 3.3b, which corresponds to the 3D shock along [100]. However, tests performed for simulation cells with sizes ranging from $120a \times 20b \times 5c$ to $120a \times 20b \times 20c$ confirmed that the defects generated filled the [001] zone irrespective of the thickness of the cell along the [001] direction. On this basis, a [100] shock simulation was performed using the $120a \times 120b \times 6c$ quasi-2D slab to eliminate any possible finite-size effects in the (001) plane and allow for more thorough characterization of the shock-induced inelastic deformation. The SFABC method as applied by Cawkwell *et al.*³⁶ was used in order to extend the length of the simulation time in the compressed state.

The overall results for the relative molecular displacements (RMDs) obtained for the quasi-2D system were similar to those presented for the 3D [100] shock in Figures 3.2(c)-(d). Likewise, the intermolecular and intramolecular temperatures were nearly identical to those presented in Figures 3.4(c)-(d). Therefore, results for those quantities obtained for the quasi-2D system are not shown. The same approach used to construct Figure 3.3 based on classification of individual molecules as either elastically compressed or inelastically displaced at the instant of maximum compression was used to generate

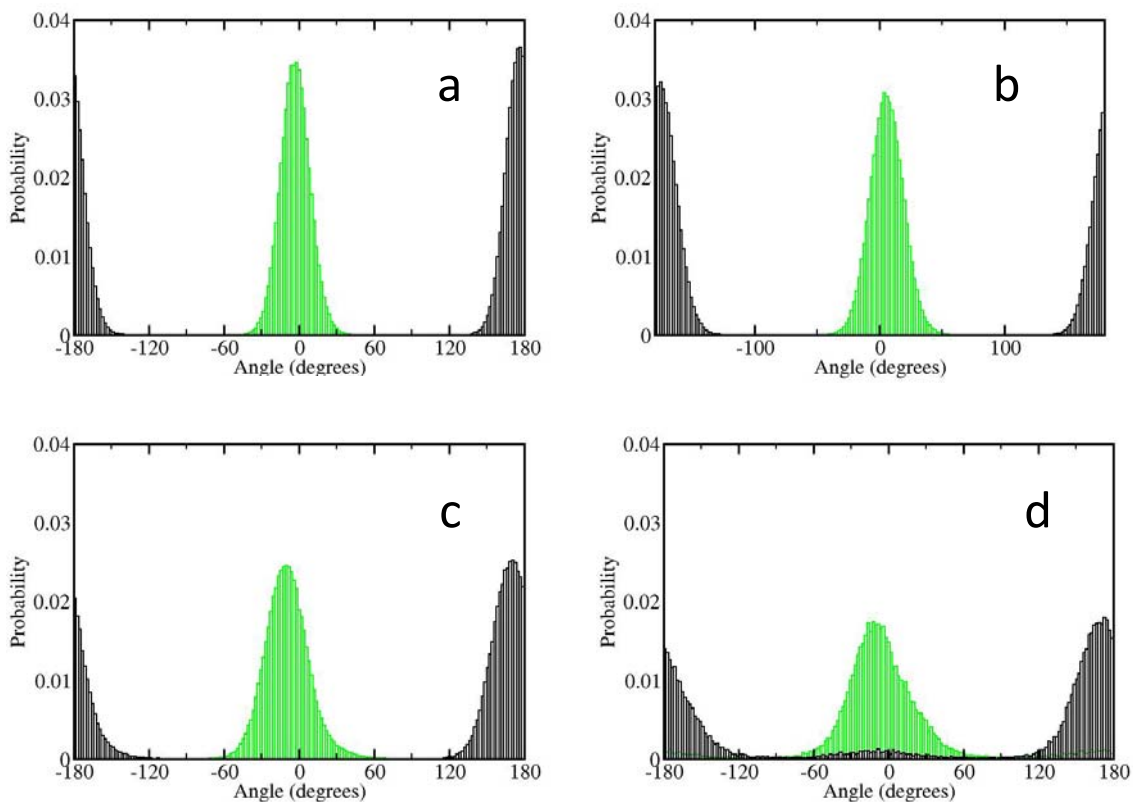


Figure 3.6. As in Figure 3.5 except results for CONO dihedral angles are shown. Green and black histograms correspond to molecules initially in *cis* and *trans* conformations, respectively.

Figure 3.7, where it is evident that finite-size effects in the (001) plane have been essentially, if not completely, eliminated; no defects propagate across the entire vertical dimension of the cell, approximately equal numbers of defects appear in (110) and $(1\bar{1}0)$ planes, and several nascent detached defects are apparent toward the left-hand end of the quiescent elastically-compressed region. Four subvolumes of material within the inelastic

deformation zone were selected for more detailed analysis; these are denoted as regions A, B, C, and D in Figure 3.7.

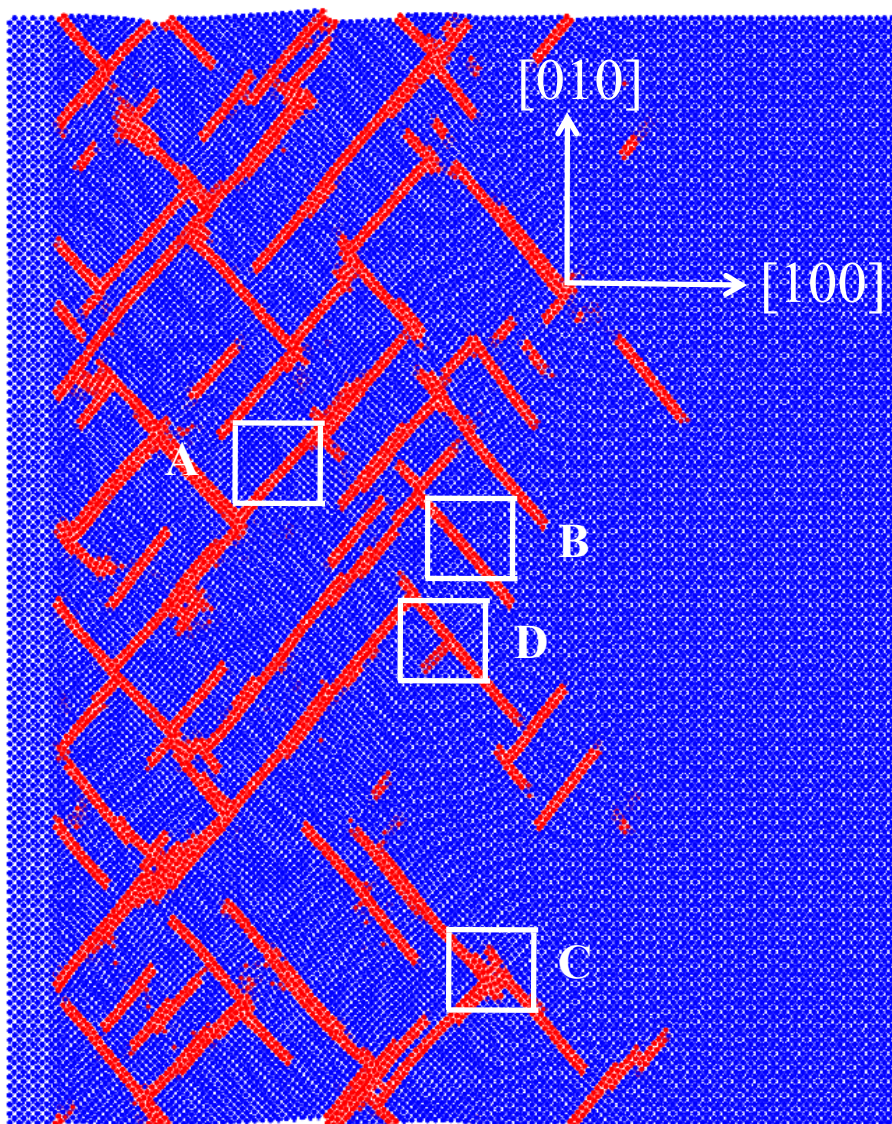


Figure 3.7. Orthographic projection of the piston and flexible slab for the quasi-2D shock at the instant of maximum compression. Elastically compressed and inelastically displaced molecules are colored blue and red, respectively. Regions A, B, C, and D are discussed in greater detail in connection with Figures 3.8 – 3.10.

3.4.1 Relative Molecular Displacements in Regions A-D

Relative molecular displacements for the molecules in each region at the time of maximum compression were calculated in the same manner as described in Sec. 3.3.1 and are presented in Figures 3.8(a)-(d) for regions A-D, respectively. For region A there are clusters of points centered about $(\pm 8, \pm 9)$ Å. Those displacements correspond closely to lattice lengths a and b in the compressed material, suggesting that the inelastically-displaced molecules in region A have undergone a full dislocation. For region B the displacements are clustered around $(\mp 6, \pm 7)$ Å, which implies that the defect in question is a partial dislocation. Because the displacements in inelastically-displaced molecules in region B did not change significantly even after ~ 23 ps of additional trajectory integration using SFABCs, we conclude that the partial dislocation is a metastable stacking fault. The displacements obtained for region C are not strongly localized to any particular region, presumably due to the large number of defects that intersect in that region. Finally, in Region D there is localization of points around $(\mp 6, \pm 7)$ Å indicating a stacking fault similar to that observed in Region B. Additional clustering of displacements in region D also occurs around $(\pm 2.5, \pm 2.5)$ Å suggesting that the propagation of the second plane of deformation has been halted due to intersection with the first one (see Figure 3.7 or trajectory animation).

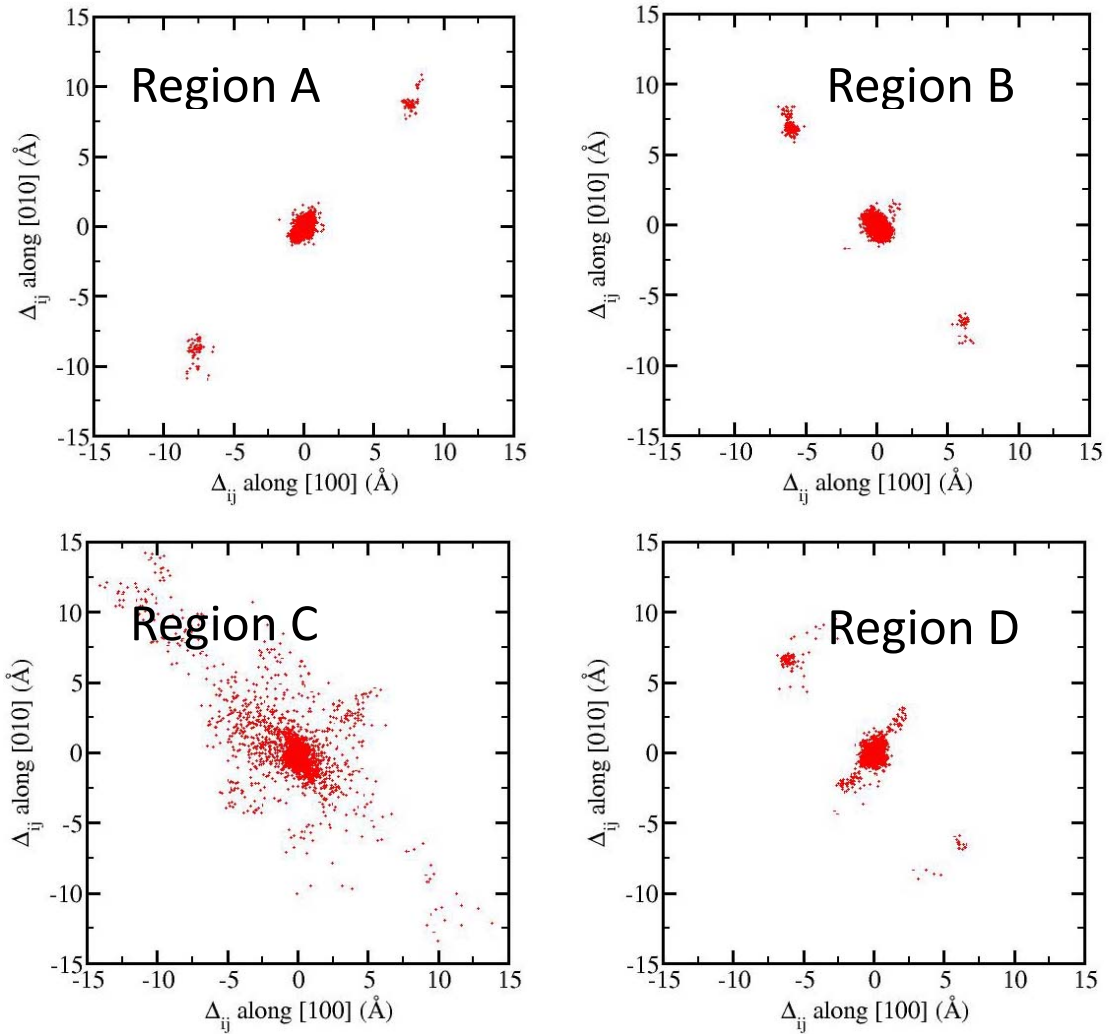


Figure 3.8. Relative molecular displacements for the quasi-2D [100] shock projected into the (001) plane at the time of maximum compression. Regions A, B, C, and D are defined in Figure 3.7.

3.4.2 Kinetic Energy Time Histories in Regions A-D

Time histories of total kinetic energies, expressed in temperature units using the equipartition theorem $T = 2E_k/(3Nk)$, were calculated separately for elastically-compressed and inelastically-displaced molecules in each region (see Figure 3.9). Note that in contrast to Figure 3.4, the ordinates in Figure 3.9 are labeled *Kinetic Energy* (with

Chapter 3: Shock-Induced Inelastic Deformation in Oriented Crystalline Pentaerythritol Tetranitrate (PETN)

units of degrees Kelvin) rather than *Temperature*, because of the net center-of-mass velocity in each region prior to shock passage. That is, the high apparent temperatures (total kinetic energies) at short times are due to the $-1.0 \text{ km}\cdot\text{s}^{-1}$ impact velocity assigned to the entire flexible slab at the beginning of the simulation; the sharp drops in kinetic energy in Figure 3.9 occur at the times the shock front passes through a given region, after which it is reasonable to discuss the results in terms of temperature. Passage of the elastic precursor wave leads to an initial shock heating to about 375 K in all cases, followed by increases in temperature due to passage of the plastic wave through the material.

The temperature of the inelastically-displaced molecules in regions A and B rises from 375 K to about 460 K in a time span of 4 ps followed by a slower cooling to a final temperature of about 425 K. The increase is due to the conversion of potential energy to kinetic energy during the localized slip process and the cooling is due to the subsequent energy equilibration with the surroundings. Region C exhibits a slower rate of heating than the other regions but settles at a higher final temperature ($\sim 450 \text{ K}$). The slower rate in region C is a result of the less-localized deformation, while the higher temperature overall arises due to the greater net plastic deformation in that region. Region D exhibits an initial rise in temperature as the process of slip begins. The increase ceases at a temperature of about 420 K when the intersection of the planes of deformation halts the growth of both slip zones.

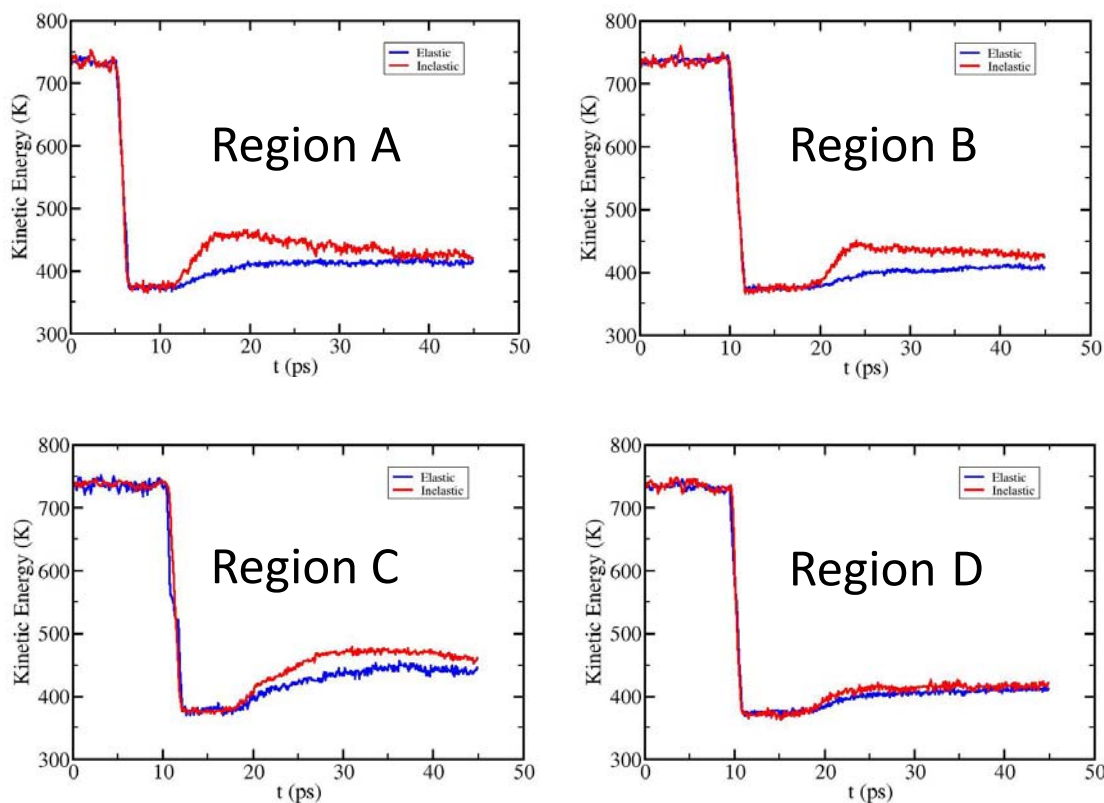


Figure 3.9. Time histories of total kinetic energies, expressed in temperature units, for molecules determined to be elastically (blue) and inelastically (red) displaced at the time of maximum compression in the quasi-2D [100] shock. Regions A, B, C, and D are defined in Fig. 3.7. SFABCs were applied at $t = 22.0$ ps.

3.4.3 Rotational Order in Regions A-D

Time histories for a rotational order parameter $P_2(t)$ were calculated separately for elastically-compressed and inelastically-displaced molecules in each region to characterize the amount of rotational (dis)order resulting from shock wave passage (Figure 3.10). The order parameter is given by

$$P_2(t) = \frac{1}{N} \sum_{i=1}^N \frac{1}{2} [3(\hat{n}_i(0) \cdot \hat{n}_i(t))^2 - 1] \quad (8)$$

where N is the number of molecules, $\hat{n}_i(0)$ is the unit vector between specified atoms at $t = 0$, and $\hat{n}_i(t)$ is the corresponding unit vector at analysis time t . Four vectors were defined per molecule corresponding to those between the central carbon atom and each of the four carbon atoms covalently bonded to it (see Figure 3.1c). Each vector was treated

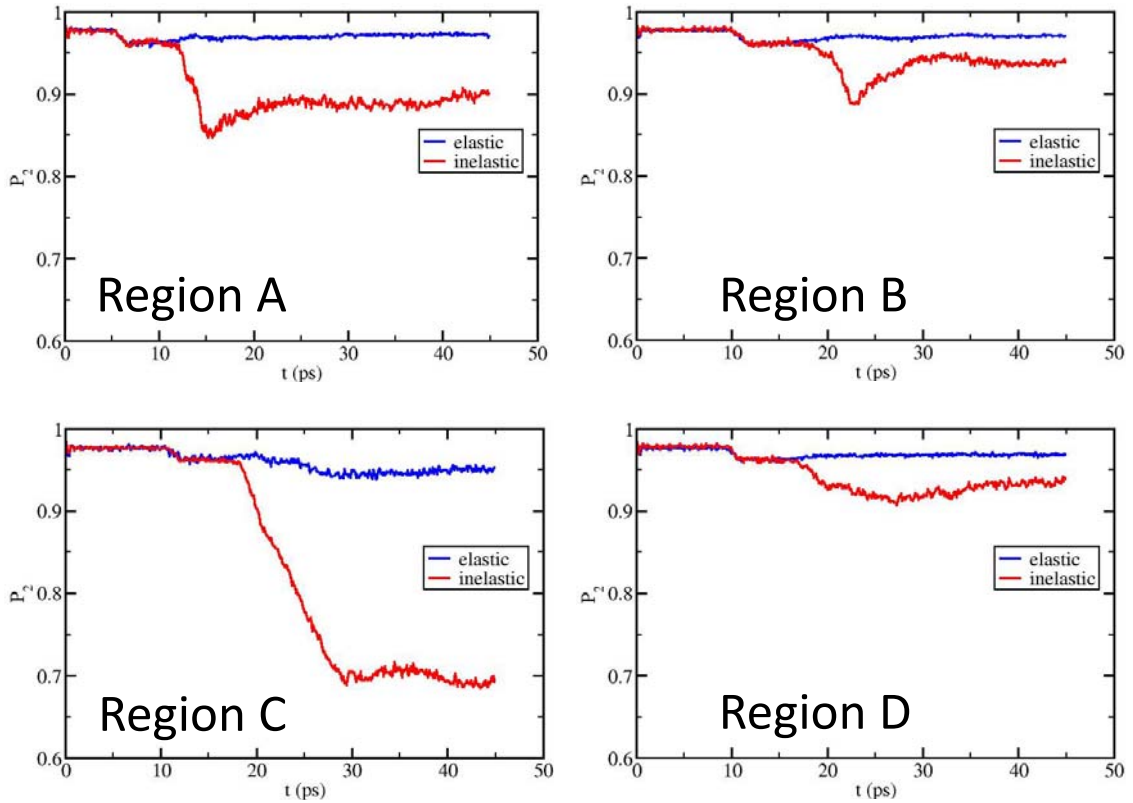


Figure 3.10. Time histories of the orientational order parameter $P_2(t)$ for molecules determined to be elastically (blue) and inelastically (red) displaced at the time of maximum compression in the quasi-2D [100] shock. Regions A, B, C, and D are defined in Figure 3.7. SFABCs were applied at $t = 22.0$ ps.

as an independently varying quantity; results in Figure 3.10 are arithmetic averages of eq 8 calculated separately for each vector. (We note that this definition does not account for symmetry-equivalent molecular orientations in the crystal structure.) The time $t = 0$ was taken to be the time at which shock was initiated in the system.

Results for $P_2(t)$ are shown in Figure 3.10. The first drop in the value of P_2 for each region is associated with passage of the elastic wave while the second drop results from passage of the slower plastic wave. In all cases except that for region C, for which relatively widespread inelastic deformation occurs, the results for molecules classified as elastically compressed are very similar.

Examination of trajectory animations for Regions A and B (see original paper) reveals that the molecules in the slip planes become rotationally disordered during slip and then largely recover after slip has completed. This is corroborated by the behavior of $P_2(t)$ seen for these regions in Figures 3.10(a)-(b). Both regions exhibit a loss of rotational order during passage of the plastic wave during slip followed by recovery to near pre-plastic-wave order after the process of slip has finished. A possible explanation for why region A appears to recover less order asymptotically than region B is the abovementioned failure to account for symmetry-equivalent orientations in the definition used for $P_2(t)$; this is currently being investigated. Region C exhibits the greatest amount of disorder among the regions examined. This is reasonable due to the intersection of several zones of deformation that results in a generalized plastic flow in this region. By contrast, a smaller amount of disorder occurs in Region D than for the other regions. Examination of the trajectory animation (see original paper) shows that the slip

displacement is interrupted by the intersection of the two planes of deformation, which in turn decreases the probability of molecular rotation.

3.4.4 Time Scales for Re-Establishing the Maxwell-Boltzmann Distribution of Kinetic Energies Behind the Shock

In Secs. 3.3.2 and 3.4.2 the kinetic energies, partitioned in various ways, were expressed in temperature units; this was done for convenience. Those quantities should not necessarily be associated with an assumption of local thermal equilibrium in the material insofar as they are based only on the average kinetic energy and not the distribution of kinetic energy, which may not be Maxwell-Boltzmann distributed in the instants following shock wave passage. This point has been discussed by Klimenko and Dremir^{75,76} in connection with MD simulations of shock waves in Lennard-Jones “argon”. In the following we present normalized distributions of instantaneous atomic and molecular center-of-mass kinetic energies, calculated for several molecular layers near the shock front in the quasi-2D system for a phase space point close to the time of maximum compression. The purpose is to address the question of whether, for the conditions immediately behind the quasi-2D [100] shock studied here, the kinetic energies are in fact Maxwell-Boltzmann distributed; or, if they are not, to estimate the distance over which the Maxwell-Boltzmann distribution is recovered. The normalized Maxwell-Boltzmann (MB) distribution for kinetic energy is given by⁷⁷

$$P(E_k) = 2\sqrt{\frac{E_k}{\pi(kT)^3}} \exp\left(\frac{-E_k}{kT}\right) \quad (9)$$

Chapter 3: Shock-Induced Inelastic Deformation in Oriented Crystalline Pentaerythritol Tetranitrate (PETN)

where $P(E_k)$ is the probability of kinetic energy E_k , k is Boltzmann's constant, and T is temperature.

The PETN unit cell contains two molecules with centers of mass separated by a distance $a/2$ along the [100] crystal direction. Based on this, for the [100] shock we define molecular layers in the (100) plane such that there are two layers per unit cell. For the quasi-2D system, this corresponds to $120 \times 6 = 720$ molecules (20880 atoms) per layer. Assignment of a particular molecule to a given layer was based on the ideal crystal structure; this is sufficient for the analysis presented here because we only consider post-shock times for which relative molecular displacements are small. For the calculation of instantaneous atomic kinetic energies (referred to hereafter as AKEs) in a given layer the instantaneous center-of-mass velocity of that entire layer was removed, after which the kinetic energy for the i th atom in the layer was computed using $^{atom}E_{k,i} = m_i \mathbf{v}_i \cdot \mathbf{v}_i / 2$ where m_i is the atomic mass and \mathbf{v}_i is the velocity vector. For the calculation of instantaneous molecular center-of-mass kinetic energies (referred to hereafter as CMKEs) in a given layer the center-of-mass velocity of that entire layer was removed, after which the CMKE of the j th molecule was computed using $^{cm}E_{k,j} = M \mathbf{v}_{cm,j} \cdot \mathbf{v}_{cm,j} / 2$ where M is the molecular mass and $\mathbf{v}_{cm,j}$ is the molecular center-of-mass velocity.

Normalized histograms of the AKEs and CMKEs are presented in Figures 3.11 and 3.12, respectively. Also shown in Figures 3.11 and 3.12 are the Maxwell-Boltzmann distributions obtained in two ways: (1) by using the "temperature" calculated from the appropriate instantaneous kinetic energy; and (2) by fitting the histogram data directly to eq 9, for which the temperature T is the only parameter. The panels in Figure 3.11

correspond to material five molecular layers in front of the shock front (Figure 3.11a), material in the layer containing the shock front (Figure 3.11b), and material one layer behind the shock front (Figure 3.11c). The panels in Figure 3.12 correspond to material five layers in front of the shock front (Figure 3.12a), material in the shock front (Figure 3.12b), and material one and two layer behind the shock front (Figures 3.12c and 3.12d, respectively).

Prior to shock excitation the AKEs (Figure 3.11a) and CMKEs (Figure 3.12a) clearly are distributed according to the MB distribution; the temperatures predicted using equipartition and from direct fit of the histogram data to eq 9 agree to within 3 K and 9 K for the AKEs and CMKEs, respectively. For the case of AKEs this is also true in the layer containing the shock front, the layer immediately behind it (Figures 3.11b and 3.11c, respectively), and all other layers further behind the shock that were examined; the equipartition-based and MB-fitted temperatures are both 384 K in the layer containing the shock front and both 383 K in the first layer behind the shock front. Given a shock velocity of $4.89 \text{ km}\cdot\text{s}^{-1}$ and a molecular layer thickness of approximately 3.8 \AA , we conclude that – for the 8.7 GPa shock strength considered – re-establishment of the Maxwell-Boltzmann distribution of atomic kinetic energies occurs on a time scale less than 80 fs. (For reference, the vibrational period of a C-H bond in PETN is approximately 11 fs.)

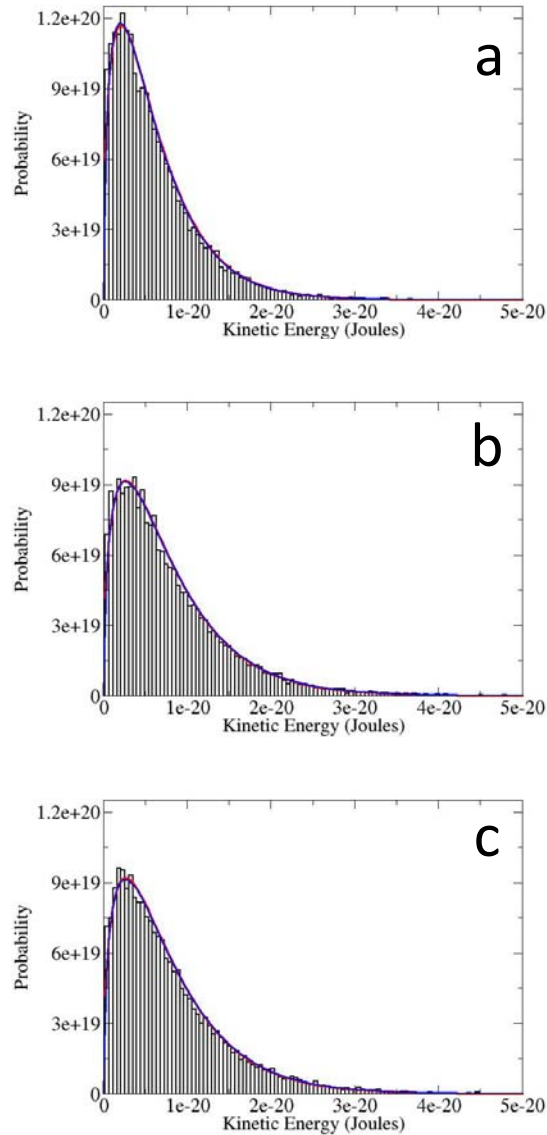


Figure 3.11. Normalized histograms of atomic kinetic energies for [100]-shocked material: (a) five molecular layers in front of the shock front, (b) in the layer containing the shock front, and (c) one molecular layer behind the shock front. Blue curves are Maxwell-Boltzmann distributions (eq 9) with the temperature defined in terms of the average kinetic energy in a given layer. Red curves are fits of eq 9 directly to the histogram data, with temperature as the only fitting parameter.

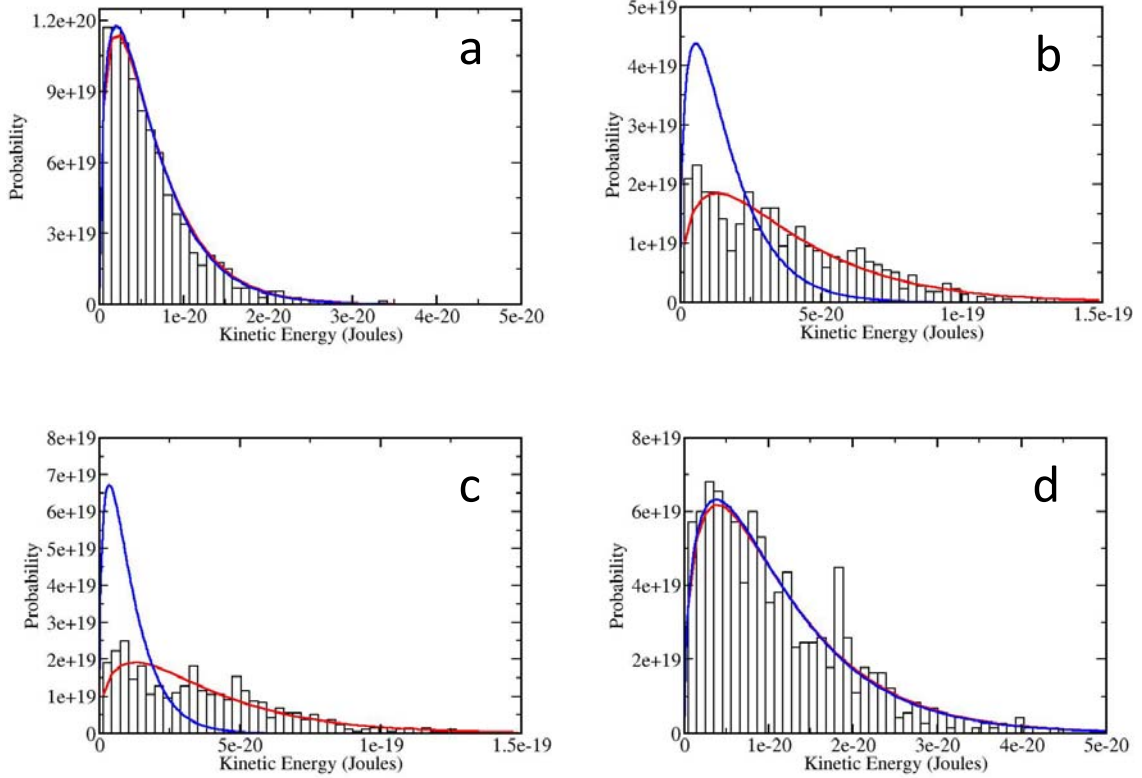


Figure 3.12. Normalized histograms of molecular center-of-mass kinetic energies for [100]-shocked material: (a) five molecular layers in front of the shock front, (b) in the layer containing the shock front, (c) one molecular layer behind the shock front, and (d) two layers behind the shock front. Blue curves are Maxwell-Boltzmann distributions (eq 9) with the temperature defined in terms of the average kinetic energy in a given layer. Red curves are fits of eq 9 to the histogram data, with temperature as the only fitting parameter. Note that abscissa and ordinate scales vary from one panel to the next.

The result for the CMKEs is considerably different. As already noted, prior to shock passage the distribution of those energies is entirely consistent with the MB distribution (Figure 3.12a). However, in the molecular layer containing the shock front (Figure 3.12b) and the first layer behind the shock (Figure 3.12c) there is a major discrepancy between

the “temperatures” predicted based on equipartition and those corresponding to best fits of the CMKE data to the MB distribution; for the layer containing the shock front the equipartition-based value (800 K) is much lower than the best fit to eq 9 (1861 K). The MB distributions obtained using the equipartition-based temperatures (blue curves) do not even approximately mirror the simulation data. The best-fit MB distributions (red curves) are in much better agreement with the data, although in both Figure 3.12b and 3.12c there appears to be a region of decreased probability at $E_k \sim 2.5 \times 10^{-20}$ J that is inconsistent with the MB distribution at any temperature. (It is possible that this is an artifact of the relatively small number of particles used to generate the histograms.) In the second layer behind the shock front the CMKE distribution is approximately MB-distributed (Figure 3.12d); temperature predictions based on equipartition and the best fit to eq 9 are 554 K and 557 K, respectively. It is important to note, however, that while the CMKEs for this layer and ones further behind the shock are approximately MB distributed (increasingly so with increasing distance behind the shock), not all of them yield as close agreement between the two temperature measures as is shown in Figure 3.12d.

From the results in Figure 3.11 we conclude that, for the case studied here, equipartition among AKEs occurs within about 80 fs of shock wave passage and from Figure 3.12 that the analogous process among CMKEs occurs on a time scale just a few to several times larger. However, from Figures 3.11, 3.12, and 3.4 it is also clear that those two partitionings of energy come to overall thermal equilibrium comparatively

quite slowly – time scales of approximately tens of ps – such that, to a good approximation, they can be treated as weakly interacting subsystems.

3.5 Conclusions

Molecular dynamics simulations of shock propagation in oriented crystalline PETN along directions known to exhibit relatively high ([001]) and low ([100]) detonation initiation sensitivities yield results that are generally consistent with the steric hindrance model proposed by Dick and co-workers.⁶⁴ The simulations were performed using the mechanically accurate, nonpolarizable form of the nonreactive force field developed by Borodin *et al.*⁶⁹ For shock pressures $P_{R-H} \sim 9$ GPa and pre-shock temperature $T = 298$ K in initially defect-free crystal, shock propagation along [001] results in a single compressive wave; whereas shock propagation along [100] results in homogeneous nucleation and spread of numerous defect structures in the [001] zone of the crystal and consequently a two-wave elastic-plastic wave structure along the [100] direction. Analysis of relative molecular center-of-mass displacements at the time of maximum compression in the crystal provides atomic-level views of the deformation processes and allows approximate classification of individual molecules as being either elastically compressed or inelastically displaced.

Spatial profiles of intermolecular and intramolecular temperature were calculated for both crystal orientations. Shock passage leads to large transient excitation of the intermolecular degrees of freedom. Excitation of intramolecular motions occurs more slowly and without transient overheating. Passage of the plastic wave through material in

the [100] shock leads to secondary heating of both intermolecular and intramolecular modes.

Distributions of CCON and CONO dihedral angles calculated in unshocked crystal and at the times of maximum compression reveal torsional defects induced by shock passage along [100] but not [001]. In the [100] shock new peaks centered at $\pm 90^\circ$ emerge in the distribution of CCON dihedrals, which initially are all *trans*, and *cis-trans* isomerization of CONO dihedral angles occurs in some of the inelastically-displaced molecules. These observations are qualitatively consistent with the notion of more hindered shear in the sensitive [001] direction.

A simulation of a [100] shock in a quasi-2D system designed to minimize finite-size effects in the transverse direction [010] was performed to provide greater insight into the kinds of shock-induced defect structures that occur in the crystal. The results revealed several types of deformation processes in the plastic zone including full dislocations, stacking faults, intersecting slip zones, and regions of more generalized plastic flow. Subregions of material containing these defects were identified for additional study. Specifically, time histories for total kinetic energy (expressed in temperature units) and rotational order were calculated in each identified region, with results obtained separately for molecules determined to be inelastically displaced *versus* elastically compressed. Maximum temperatures were higher for molecules that were inelastically displaced. Loss of rotational order occurs during dislocation slip but is nearly completely recovered within a few tens of ps.

Chapter 3: Shock-Induced Inelastic Deformation in Oriented Crystalline Pentaerythritol Tetranitrate (PETN)

For the [100] shock strength considered here, $P_{R-H}^{[100]} = 8.7$ GPa, distributions of atomic kinetic energies calculated for molecularly-thin layers of material located in and just behind the shock front remain in local thermal equilibrium during the shock heating process; that is, they remain Maxwell-Boltzmann distributed on all time scales greater than ~ 80 fs . By contrast, molecular center-of-mass kinetic energies do not remain in local thermal equilibrium during the shock rise. Distribution functions for that quantity calculated in the shock front exhibit pronounced deviations from the Maxwell-Boltzmann distribution that persist for a few to several molecular layers (*i.e.*, a few hundred to several hundred fs) behind the shock front.

References

- (1) Bottaro, J. In *Overviews of Recent Research on Energetic Materials*; Shaw, R. W., Brill, T. B., Thompson, D. L., Eds.; World Scientific Publishing Co. Pte. Ltd.: **2005**; Vol. 16, p 501.
- (2) Hirth, J. P.; Lothe, J. *Theory of Dislocations*; John Wiley & Sons: New York, **1982**.
- (3) Hull, D.; Bacon, D. J. *Introduction to Dislocations*; Third ed.; Pergamon Press: New York, **1984**.
- (4) Armstrong, R. W. *Rev. Adv. Mater. Sci.* **2009**, *19*, 13.
- (5) Sandusky, H. W.; Glancy, B. C.; Carlson, D. W.; Elban, W. L.; Armstrong, R. W. *J. Propulsion* **1991**, *7*.
- (6) Holian, B. L.; Germann, T. C.; Maillet, J. B.; White, C. T. *Physical Review Letters* **2002**, *89*, 285501.
- (7) Tran, L.; Udaykumar, H. S. *Journal of Propulsion and Power* **2006**, *22*, 947.
- (8) Tran, L.; Udaykumar, H. S. *Journal of Propulsion and Power* **2006**, *22*, 959.
- (9) Menikoff, R. *Combustion Theory and Modelling* **2006**, *10*, 1003.
- (10) Hu, Y.; Brenner, D. W.; Shi, Y. *The Journal of Physical Chemistry C* **2011**, *115*, 2416.
- (11) Duesbery, M. S.; Vitek, V. *Acta Materialia* **1998**, *46*, 1481.
- (12) Ismail-Beigi, S.; Arias, T. A. *Physical Review Letters* **2000**, *84*, 1499.
- (13) Schiotz, J.; Jacobsen, K. W. *Science* **2003**, *301*, 1357.
- (14) Bringa, E. M.; Caro, A.; Wang, Y.; Victoria, M.; McNaney, J. M.; Remington, B. A.; Smith, R. F.; Torralva, B. R.; Van Swygenhoven, H. *Science* **2005**, *309*, 1838.
- (15) Cawkwell, M. J.; Nguyen-Manh, D.; Woodward, C.; Pettifor, D. G.; Vitek, V. *Science* **2005**, *309*, 1059.
- (16) Ramos, K. J.; Bahr, D. F. *Journal of Materials Research* **2007**, *22*, 2037.
- (17) Ramos, K. J.; Hooks, D. E.; Bahr, D. F. *Philosophical Magazine* **2009**, *89*, 2381.
- (18) Lei, L.; Koslowski, M. *Philosophical Magazine* **2011**, *91*, 865
- (19) Rice, B. M.; Sewell, T. D. In *Static Compression of Energetic Materials*; First ed.; Peiris, S. M., Piermarini, G. J., Eds.; Springer-Verlag: 2008, p 330.
- (20) Sorescu, D. C.; Rice, B. M.; Thompson, D. L. *The Journal of Physical Chemistry B* **2000**, *104*, 8406.
- (21) Agrawal, P. M.; Rice, B. M.; Thompson, D. L. *The Journal of Chemical Physics* **2003**, *119*, 9617.
- (22) Zheng, L.; Luo, S. N.; Thompson, D. L. *The Journal of Chemical Physics* **2006**, *124*, 154504.
- (23) Desbiens, N.; Bourasseau, E.; Maillet, J. B. *Molecular Simulation* **2007**, *33*, 1061.
- (24) Hervouet, A.; Desbiens, N.; Bourasseau, E.; Maillet, J. B. *The Journal of Physical Chemistry B* **2008**, *112*, 5070.
- (25) Desbiens, N.; Bourasseau, E.; Maillet, J. B.; Soulard, L. *Journal of Hazardous Materials* **2009**, *166*, 1120.
- (26) Siavosh-Haghighi, A.; Dawes, R.; Sewell, T. D.; Thompson, D. L. *The Journal of Chemical Physics* **2009**, *131*, 064503.
- (27) He, L.; Sewell, T. D.; Thompson, D. L. *The Journal of Chemical Physics* **2011**, *134*, 124506.
- (28) Slough, W.; Perger, W. F. *Chemical Physics Letters* **2010**, *498*, 97.
- (29) Smith, G. D.; Bharadwaj, R. K. *The Journal of Physical Chemistry B* **1999**, *103*, 3570.
- (30) Bedrov, D.; Smith, G. D.; Sewell, T. D. *Chemical Physics Letters* **2000**, *324*, 64.
- (31) Bedrov, D.; Smith, G. D.; Sewell, T. D. *The Journal of Chemical Physics* **2000**, *112*, 7203.

Chapter 3: Shock-Induced Inelastic Deformation in Oriented Crystalline Pentaerythritol Tetranitrate (PETN)

- (32) Sewell, T. D.; Menikoff, R.; Bedrov, D.; Smith, G. D. *The Journal of Chemical Physics* **2003**, *119*, 7417.
- (33) Jaramillo, E.; Sewell, T. D.; Strachan, A. *Physical Review B* **2007**, *76*, 064112.
- (34) Strachan, A.; van Duin, A. C. T.; Chakraborty, D.; Dasgupta, S.; Goddard III, W. A. *Physical Review Letters* **2003**, *91*, 098301.
- (35) Strachan, A.; Kober, E. M.; van Duin, A. C. T.; Oxgaard, J.; Goddard III, W. A. *The Journal of Chemical Physics* **2005**, *122*, 054502.
- (36) Cawkwell, M. J.; Sewell, T. D.; Zheng, L.; Thompson, D. L. *Physical Review B* **2008**, *78*, 014107.
- (37) Bedrov, D.; Hooper, J. B.; Smith, G. D.; Sewell, T. D. *The Journal of Chemical Physics* **2009**, *131*, 034712.
- (38) Cawkwell, M. J.; Ramos, K. J.; Hooks, D. E.; Sewell, T. D. *Journal of Applied Physics* **2010**, *107*, 063512.
- (39) Ramos, K. J.; Hooks, D. E.; Sewell, T. D.; Cawkwell, M. J. *Journal of Applied Physics* **2010**, *108*, 066105.
- (40) Munday, L. B.; Chung, P. W.; Rice, B. M.; Solares, S. D. *The Journal of Physical Chemistry B* **2011**, *115*, 4378.
- (41) Mathew, N.; Picu, R. C. **2011**.
- (42) Byrd, E. F. C.; Rice, B. M. *The Journal of Physical Chemistry C* **2007**, *111*, 2787.
- (43) Budzevich, M. M.; Landerville, A. C.; Conroy, M. W.; Lin, Y.; Oleynik, I. I.; White, C. T. **2010**.
- (44) Dick, J. J.; Ritchie, J. P. *Journal of Applied Physics* **1994**, *76*, 2726.
- (45) Gruzdkov, Y. A.; Gupta, Y. M. *The Journal of Physical Chemistry A* **2000**, *104*, 11169.
- (46) Winey, J. M.; Gupta, Y. M. *Journal of Applied Physics* **2001**, *90*, 1669.
- (47) Winey, J. M.; Gupta, Y. M. *Journal of Applied Physics* **2010**, *107*, 103505.
- (48) Gee, R. H.; Wu, C.; Maiti, A. *Applied Physics Letters* **2006**, *89*, 021919.
- (49) Budzien, J.; Thompson, A. P.; Zybin, S. V. *The Journal of Physical Chemistry B* **2009**, *113*, 13142.
- (50) Zybin, S. V.; Goddard III, W. A.; Xu, P.; van Duin, A. C. T.; Thompson, A. P. *Applied Physics Letters* **2010**, *96*, 081918.
- (51) Piryatinski, A.; Tretiak, S.; Sewell, T. D.; McGrane, S. D. *Physical Review B* **2007**, *75*, 214306.
- (52) Velizhanin, K. A.; Kilina, S.; Sewell, T. D.; Piryatinski, A. *The Journal of Physical Chemistry B* **2008**, *112*, 13252.
- (53) Pereverzev, A.; Sewell, T. D. *The Journal of Chemical Physics* **2011**, *134*, 014513.
- (54) Perger, W. F.; Vutukuri, S.; Dreger, Z. A.; Gupta, Y. M.; Flurchick, K. *Chemical Physics Letters* **2006**, *422*, 397.
- (55) Herring, S. D.; Germann, T. C.; Grønbech-Jensen, N. *Physical Review B* **2010**, *82*, 214108.
- (56) Lynch, K.; et al. *Modelling and Simulation in Materials Science and Engineering* **2009**, *17*, 015007.
- (57) Izvekov, S.; Chung, P. W.; Rice, B. M. *The multiscale coarse-graining method: Assessing its accuracy and introducing density dependent coarse-grain potentials*; AIP, 2010; Vol. 133.
- (58) Bouma, R. H. B.; van der Heijden, A. E. D. M.; Sewell, T.; Thompson, D. L. In *Numerical Simulations*; Awrejcewicz, J., Ed.; InTech: 2011, p 29.
- (59) Jones, W. M.; Giauque, W. F. *Journal of the American Chemical Society* **1947**, *69*, 983.

Chapter 3: Shock-Induced Inelastic Deformation in Oriented Crystalline Pentaerythritol Tetranitrate (PETN)

- (60) McCullough, J. P.; Scott, D. W.; Pennington, R. E.; Hossenlopp, I. A.; Waddington, G. *Journal of the American Chemical Society* **1954**, *76*, 4791.
- (61) Trevino, S. F.; Prince, E.; Hubbard, C. R. *Refinement of the structure of solid nitromethane*; AIP, **1980**; Vol. 73.
- (62) Bedrov, D.; Ayyagari, C.; Smith, G.; Sewell, T. D.; Menikoff, R.; Zaug, J. *Journal of Computer-Aided Materials Design* **2001**, *8*, 77.
- (63) Dick, J. J. *Applied Physics Letters* **1984**, *44*, 859.
- (64) Dick, J. J.; Mulford, R. N.; Spencer, W. J.; Pettit, D. R.; Garcia, E.; Shaw, D. C. *Journal of Applied Physics* **1991**, *70*, 3572.
- (65) Dick, J. J. *Journal of Applied Physics* **1997**, *81*, 601.
- (66) Dick, J. J.; Hooks, D. E.; Menikoff, R.; Martinez, A. R. *Journal of Applied Physics* **2004**, *96*, 374.
- (67) Hooks, D. E.; Ramos, K. J.; Martinez, A. R. *Journal of Applied Physics* **2006**, *100*, 024908.
- (68) Shan, T. R.; Thompson, A. P. *Journal of Physics: Conference Series* **2014**, *500*, 172009.
- (69) Borodin, O.; Smith, G. D.; Sewell, T. D.; Bedrov, D. *The Journal of Physical Chemistry B* **2007**, *112*, 734.
- (70) Plimpton, S. *Journal of Computational Physics* **1995**, *117*, 1.
- (71) Hockney, R. W.; Eastwood, J. W. *Computer Simulations Using Particles*; McGraw-Hill: New York, **1981**.
- (72) Conant, J. W.; Cady, H. H.; Ryan, R. R.; Yarnell, J. L.; Newsam, J. M. *The Atom Positions of Pentaerythritol Tetranitrate (PETN) Determined by X-Ray and by Neutron Diffraction*, Los Alamos National Labs, **1979**.
- (73) Perlman, D. A.; Case, D. A.; Caldwell, J. C.; Seibel, G. L.; Singh, U. C.; Weiner, P.; Kollman, P. A. University of California, San Francisco, **1991**.
- (74) Strachan, A.; Holian, B. L. *Physical Review Letters* **2005**, *94*, 014301.
- (75) Klimenko, V. Y.; Dremin, A. N. *Sov. Phys. Dokl.* **1979**, *24*, 984.
- (76) Klimenko, V. Y.; Dremin, A. N. *Sov. Phys. Dokl.* **1980**, *25*, 288.
- (77) McQuarrie, D. A. *Statistical Mechanics*; University Science Books: Sausalito, California, **2000**.

Chapter 4: Molecular Dynamics Simulations of the Collapse of a Cylindrical Pore in the Energetic Material α -RDX^a

4.1 Introduction

The role of *hot spots* in the initiation of detonation in solid energetic materials has been of interest since their existence was proposed by Bowden and Yoffe.¹ Hot spots are, in essence, localized regions of high temperature and pressure in a material that serve as nucleation sites for initiating and possibly sustaining rapid chemistry. Whether a hot spot will grow or quench depends on a sensitive balance between energy release due to local physical and chemical processes and energy transport away from the hot spot due to various dissipation mechanisms.² Bowden and Yoffe identified critical hot spots as having sizes of 0.1–10 μm , lifetimes of 0.1–10 ms, and temperatures greater than 700 K.¹ Tarver *et al.*³ developed chemical kinetic decomposition models of 1,3,5,7-tetranitroperhydro-1,3,5,7-tetrazocine (HMX) and 1,3,5-triamino-2,4,6-trinitrobenzene (TATB) to estimate the critical conditions for hot spots in those materials. They estimated sizes in the μm range and temperatures above 700 K, similar to the values proposed by Bowden and Yoffe.

Accurate determination of hot spot critical parameters is difficult due to the small spatio-temporal scale and difficulty in defining exactly what constitutes a hot spot in a given material under a given loading condition. Field⁴ provides a list summarizing works that identify several possible sources of hot spots including pore collapse^{5,6}, adiabatic

a: Original publication – Eason, R. M., Sewell, T.D. *Journal of Dynamic Behavior of Materials* **2015**, 1, 423

Chapter 4: Molecular Dynamics Simulations of the Collapse of a Cylindrical Pore in the Energetic Material α -RDX

shear bands⁷, dislocation pileups⁸, and friction⁹. Further insights into the multi-scale interactions between shock waves, defects and interfaces, and the resulting energy localization are essential to forming a more complete understanding of complex detonation initiation processes. Furthermore, the integral role of hot spots in detonation initiation provides strong motivation for understanding the dominant formation mechanisms for a given kind of material and loading scenario.

The relationship between pore collapse and the generation of hot spots has received considerable attention. Bourne, Field, and co-workers¹⁰⁻¹³ have employed high-speed photography to characterize cavity collapse processes in 12% by weight mixtures of gelatin in water and ammonium nitrate/sodium nitrate emulsions for pores ranging in diameter from 3 to 12 mm. They used photoluminescence to identify areas where reaction occurred during collapse, and determined that the principal ignition mechanism is the ejection of material from the upstream wall of the pore to form a hydrodynamic jet that impacts the downstream wall. Swantek and Austin¹⁴ extended the work of Bourne and Field by supplementing high-speed photography results with data from particle image velocimetry measurements of the collapse of 3 mm diameter cylindrical cavities arranged in various array structures in a mixture of agarose and glycerol gradient buffer. For pores aligned parallel to the impact direction the velocity fields exhibited a defracted wave structure from the upstream pore that partially shielded, and slowed, the collapse of the downstream pore. The collapse was faster when the pores were arranged in a staggered pattern. Dattelbaum *et al.*¹⁵ mixed solid silica beads and microballoons into liquid nitromethane to act as micron-scale hot spot sources. While both types of nitromethane mixtures were more sensitive compared to the pure liquid, the effect was larger when

Chapter 4: Molecular Dynamics Simulations of the Collapse of a Cylindrical Pore in the Energetic Material α -RDX

hollow microballoons were used. This was attributed to the pore collapse that occurred after shock passage.

The mm-scale pores mentioned in the preceding paragraph are orders of magnitude larger than the ones that exist in a real composite explosive.¹⁶⁻¹⁸ Direct experimental observation of pore collapse in real explosives is extremely difficult due to the high strain rates and small spatio-temporal scales over which pore collapse occurs, and because the phenomena of interest occur in the bulk of an optically impenetrable material. Computer simulations provide a practical approach for elucidating the details of pore collapse with essentially arbitrary spatial and temporal resolution. Hydrocodes are appropriate for and widely applied to continuum-scale problems. Menikoff¹⁹ has simulated shock-induced pore collapse in HMX and emphasized the importance of mesh resolution and correct dissipative mechanisms for accurate predictions of the tail regions of hot spot mass fraction and temperature distributions. Ball *et al.*²⁰ used computational fluid dynamics to simulate the experimental setup of Bourne and Field.²¹ They obtained agreement between the locations of hot gas predicted by their simulations and the areas of luminescence seen in the Bourne and Field experiment. Tran and Udaykumar^{22,23} simulated pore collapse for both reactive and inert cases in a material with mechanical properties similar to HMX. They reported the pressures, temperatures, and ratios of internal energy to kinetic energy observed during the collapse of a 5 μm diameter pore. The formation of a hydrodynamic jet was found to be responsible for the greatest increase in internal energy. Jackson *et al.*²⁴ have recently developed a model for which the goal is to reproduce data from sensitivity tests to gain a better understanding of the factors that determine material sensitivity. They used parameters from micro-scale simulations as

Chapter 4: Molecular Dynamics Simulations of the Collapse of a Cylindrical Pore in the Energetic Material α -RDX

input to macro-scale simulations in which shocks produced by the collapse of hot spots were strengthened by interacting with downstream hot spots where ignition had begun but not completed.

Barton *et al.*²⁵ have developed a crystal-level model of defect-containing HMX that incorporates strain localization to predict heat generation from pore collapse. Austin *et al.*^{26,27} recently developed a reactive model that includes anisotropic, thermoelastic-viscoplastic response to study the temperature localization that results from shock-induced collapse of a 1 μm diameter pore in β -HMX. They considered shocks normal to the (111) plane in the $P2_1/c$ space group setting and a shock pressure of 9.4 GPa. They determined that the dominant deformation mechanism was shear bands that nucleate at and grow away from the pore. The model was found to be insensitive to initial crystal orientation but was sensitive to the temperature-dependent liquid viscosity, which was found to affect the extent of chemical reactions in the liquid shear band regions. Most simulations of pore collapse consider idealized spherical pores in 3-D or cylindrical pores with the cylinder axis oriented normal to the shock direction in 2-D. However, Levesque and Vitello²⁸ analyzed temperature maps obtained from continuum simulations of shocked-induced pore collapse in TATB containing other pore morphologies and determined that higher temperatures are achieved for certain oriented non-spherical pore shapes including elliptical, cylindrical, and conical.

Two limitations of continuum-scale models are the fundamental inability to resolve features that occur on the molecular scale and the associated requirement to formulate and parameterize physical models that effectively capture the sub-scale

Chapter 4: Molecular Dynamics Simulations of the Collapse of a Cylindrical Pore in the Energetic Material α -RDX

physical phenomena. At the other extreme, molecular dynamics (MD) simulations can be used to study materials with atomic-scale resolution, but typically only for sub-micron space and sub-nanosecond time scales. (This statement applies to the situation studied here, wherein molecular systems are described using empirical all-atom potential energy functions that include intramolecular flexibility and long-range intermolecular interactions but not chemical reactivity; for reactive potentials the simulation domains are typically much smaller.) However, MD simulations can still provide useful information concerning the mechanisms involved in nano-scale pore collapse processes. For example, Holian *et al.*²⁹, employing MD simulations of ejecta release and recompression across a planar gap in a Lennard-Jones system, determined that vaporization of material into the pore during collapse and the subsequent PV work involved in recompressing the vapor was responsible for the extreme heating that occurs in hot spots. Hatano³⁰ posited that temperature alone is not sufficient to quantify the amount of chemistry occurring in simulations of pore collapse and supplemented temperature profiles with a measure of the number of energetic collisions in the pore (normalized by initial pore volume). He performed simulations on 3-D Lennard-Jones systems containing cuboid-shaped pores of varying size and found that increased cross-sectional area normal to the shock direction increases the number of energetic intermolecular collisions whereas longer pore length parallel to the shock direction increases the peak temperature resulting from the collapse. Shi and Brenner³¹ reported 2-D MD simulations of the collapse of nanometer-scale square pores in nitrocubane crystals in which they observed the jetting commonly seen at larger scales in experiments and continuum simulations. Mintmire *et al.*³² performed MD simulations of cylindrical pore collapse in a model diatomic material in which the

Chapter 4: Molecular Dynamics Simulations of the Collapse of a Cylindrical Pore in the Energetic Material α -RDX

mechanism of collapse was found to vary with shock strength. Strong shocks resulted in a turbulent collapse that produced vibrational excitation in the molecules initially near the pore. Herring *et al.*³³ performed MD shock simulations using a reactive potential on systems of diatomic molecules for samples that contained pores of various sizes and arrangements. Increasing pore size was found to lower the minimum piston velocity needed to initiate detonation, reduce the time to detonation, and increase the extent of reaction in the samples. Shan and Thompson performed MD simulations with the ReaxFF reactive force field^{34,35} to study the effect of 3-D spherical pore collapse on reactivity of pentaerythritol tetranitrate (PETN)³⁶ and ammonium nitrate/fuel oil (ANFO).³⁷ At an impact velocity of $U_p = 2.0 \text{ km}\cdot\text{s}^{-1}$ along the [110] direction in PETN, which is insufficient to initiate widespread chemistry in a defect-free crystal on the $\approx 10.9 \text{ ps}$ time scale of their simulations, Shan and Thompson observed collapse of a 20.0 nm spherical pore produced enhanced chemical reactivity compared to defect-free PETN.³⁶ Shocks propagating along [100] in ammonium nitrate containing a 10.0 nm diameter spherical inclusion filled with fuel oil resulted in enhanced reactivity compared to defect-free ammonium nitrate. The highest temperatures were found to occur at the interface between the ammonium nitrate and the fuel oil.³⁷

The energetic material 1,3,5-trinitroperhydro-1,3,5-triazine (RDX, see Figure 4.1(a)) has been widely studied both experimentally³⁸⁻⁴⁵ and theoretically.^{35,46-52} There are four known polymorphs of RDX, denoted α ⁵³, β ⁵⁴, ϵ ⁵⁵, and γ ⁵⁶. The α -phase is the stable form at room temperature and atmospheric pressure and has received the most study. Hooks and co-workers examined α -RDX (hereafter, RDX) shock response using impact experiments,³⁸ identified deformation mechanisms using nanoindentation,³⁹ and studied

Chapter 4: Molecular Dynamics Simulations of the Collapse of a Cylindrical Pore in the Energetic Material α -RDX

decomposition using time-resolved emission spectroscopy.⁴⁰ Munday *et al.*⁵⁷ calculated generalized stacking fault energy surfaces using MD simulations to identify likely cleavage planes and slip planes to predict whether a given slip system will be brittle or ductile. Results obtained for the (010)[100], (021)[100], and (011)[100] slip planes were in good agreement with experiment. For the (010)[001] system, the authors predicted brittle response whereas experiments^{39,58} indicate this is a slip system. Theoretical calculations of Peierls stresses from atomic simulations to rank activated slip systems in RDX show agreement with the anisotropic plastic deformation response observed in experiment.⁵⁹ Strachan *et al.*³⁵ employed the ReaxFF³⁴ reactive force field to perform computer simulations on the thermal decomposition of RDX crystals. They observed an Arrhenius temperature dependence of the calculated characteristic reaction time.

Sewell and co-workers^{41,47-49} used MD simulations to identify and characterize plastic deformation mechanisms in single crystals of RDX subjected to shock waves propagating normal to the (100), (111), and (021) crystal planes. Cawkwell *et al.*⁴⁷ reported the formation of nano-scale shear bands for shocks propagating normal to (100). Cawkwell *et al.*⁴⁹ performed MD simulations in an attempt to explain an anomalous elastic-plastic response in the measured shock profiles for (111)-oriented RDX reported by Hooks *et al.*³⁸, and determined that this response resulted from a hardening effect created by the homogeneous nucleation of partial dislocation loops in the crystal at a well-defined shock strength. Ramos *et al.*⁴¹ predicted using MD and verified experimentally using plate-impact experiments that a similar anomalous response would be obtained for shocks in (021)-oriented RDX due to commonalities in the slip systems activated by shocks on the (111) and (021) crystal planes. All of the shocks studied by

Chapter 4: Molecular Dynamics Simulations of the Collapse of a Cylindrical Pore in the Energetic Material α -RDX

Sewell and co-workers^{41,47-49} were performed using a non-reactive force field at low impact strengths; Rankine-Hugoniot shock pressures P_{RH} ranging from 1.34 to 9.7 GPa, similar to those that might exist in accident scenarios. Nomura *et al.*⁵¹ examined stronger impact strengths ($U_p = 1.0$ and $3.0 \text{ km}\cdot\text{s}^{-1}$) using MD simulations with the ReaxFF force field to study shock propagation in (100)-oriented RDX that contained an initially 8 nm diameter spherical pore. They reported shock-induced vibrational excitation leading to bond breakage and the formation of NO_2 , N_2 , and H_2O in the vicinity of the pore collapse. They also reported an impact-strength-dependent pinning/de-pinning effect on the shock front due to passage over the pore surface and subsequent collapse.

In this study we performed MD simulations of pore collapse in (100)-oriented α -RDX for the case of shock wave passage over an initially 35 nm diameter cylindrical pore with the cylinder axis aligned parallel to the [010] crystal direction in the orthorhombic crystal (see Figure 4.1). Impact velocities $U_p = 1.0 \text{ km}\cdot\text{s}^{-1}$, $2.0 \text{ km}\cdot\text{s}^{-1}$, and $3.0 \text{ km}\cdot\text{s}^{-1}$, corresponding to nominal shock pressures $P_s = 9.71$, 24.00, and 42.48 GPa in defect-free crystal, were considered as representative of weak, moderate, and strong shocks. Our main interest is in characterizing the nature of material flow, the nature and extent of energy and pressure localization, and molecular-scale disorder induced by the shock. The force field used for this work is non-reactive. Neglect of chemistry is reasonable at the lower shock pressures but is a gross approximation for the strong shock. Nevertheless, the qualitative information on material flow and energy localization as a function of impact strength is still a useful contribution to the knowledge base for pore collapse in an anisotropic molecular crystal.

4.2 Methods

All simulations were performed using the Large-scale Atomic/Molecular Massively Parallel Simulator (LAMMPS)⁶⁰ code in conjunction with the fully flexible non-reactive nitramine force field developed by Smith and Bharadwaj (S-B)^{61,62}. Three-dimensional periodic boundary conditions were used in all cases. Potentials for covalent bonds, three-center angles, and improper dihedrals are represented as harmonic functions. Dihedral potentials are represented by a sum of cosine terms. Non-bonded interactions are described by the Buckingham-plus-Coulomb potential with fixed atomic partial charges located on the nuclei. The non-bonded interactions apply to all intermolecular atom pairs as well as intramolecular atom pairs separated by three or more covalent bonds within a molecule (often called 1-4 interactions). A 1.0 nm cutoff was used for the repulsion terms and the real part of the dispersion and electrostatic interactions. Long-range interactions were evaluated with the particle-particle particle-mesh (PPPM)⁶³ algorithm with the relative RMS error in the forces set to 1×10^{-4} . While the S-B force field was originally developed for HMX, the methods by which it was formulated and parameterized were such that it should also be applicable to RDX; and Cawkwell *et al.*⁴⁷ and Munday *et al.*⁵⁰ determined that this is the case for both α - and γ -RDX. We obtained (300 K, 1 atm) lattice parameters $a = 1.3498$ nm, $b = 1.1554$ nm, and $c = 1.0564$ nm based on simulations for a 3-D periodic $4a \times 4b \times 5c$ supercell in the isostress-isothermal ($N\sigma T$) ensemble in which separate barostats were applied to each lattice direction and the cell overall was treated as triclinic. (The thermostat and barostat coupling parameters were set to 100.0 and 100.0 fs, respectively.) These lattice parameters compare well with the experimental values⁵³ $a = 1.320$ nm, $b = 1.160$ nm, and $c = 1.072$ nm; the values $a =$

Chapter 4: Molecular Dynamics Simulations of the Collapse of a Cylindrical Pore in the Energetic Material α -RDX

1.3400 nm, $b = 1.1517$ nm, and $c = 1.0623$ nm reported by Cawkwell *et al.*⁴⁷; and $a = 1.345$ nm, $b = 1.153$ nm, and $c = 1.053$ nm reported by Munday *et al.*⁵⁰ for the same conditions. The calculated lattice parameters we obtained were used in the construction of all supercells described below.

Shock waves were generated in a reverse-ballistic configuration by impacting from the right with speed U_p a thermalized slab of flexible molecules (hereafter the *flexible slab*) onto a rigid, stationary piston composed of the same material (the *piston*). This results in a shock wave that propagates from left to right through the flexible slab with shock speed $U_s = U_w + U_p$, where U_w is the speed of the wave measured in the frame of the stationary piston. Impact speeds $U_p = 1.0 \text{ km}\cdot\text{s}^{-1}$, $2.0 \text{ km}\cdot\text{s}^{-1}$, and $3.0 \text{ km}\cdot\text{s}^{-1}$ were studied. Corresponding shock pressures, calculated using the Rankine-Hugoniot relation $P_s = \rho_0 U_s U_p$, where ρ_0 is the pre-shock density of the crystal, were $P_s = 9.71$, 24.00 , and 42.48 GPa, respectively. These pressures are within 1.94% of the longitudinal stress components P_{xx} calculated directly from the atomic stress tensor for defect-free crystal.

The supercell for the shock simulations was obtained by replicating the crystal unit cell by factors of 120, 3, and 135 along the \hat{a} , \hat{b} , and \hat{c} crystal directions, respectively, then adding a 20.0 nm vacuum pad parallel to the \hat{a} crystal direction. The purpose of the vacuum pad is to minimize interactions between the piston (which is created after equilibration just prior to initiation of the shock) and right-hand side of the flexible slab across the periodic boundary along \hat{a} . We aligned the \hat{a} , or [100], crystal direction with the x -axis; the \hat{b} , or [010], crystal direction with the y -axis; and the \hat{c} , or [001], crystal direction with the z -axis. The size of the resulting slab of material,

excluding the vacuum, was approximately $162.0 \text{ nm} \times 3.5 \text{ nm} \times 142.6 \text{ nm}$ (see Figure 4.1(b)). Justification for using a simulation cell that is thin along $[010]$ comes from

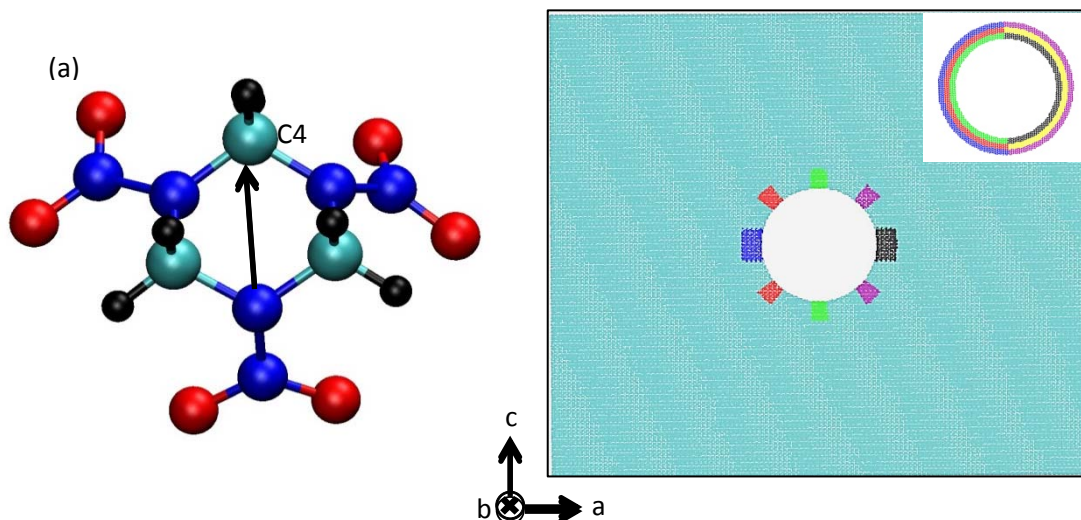


Figure 4.1. (a) An RDX molecule. Carbon is cyan, nitrogen is dark blue, oxygen is red, and hydrogen is black. Atoms N1 and C4 are used to define the vector discussed in Section III.B. (b) Snapshot of the molecular center-of-mass locations in the simulation cell prior to shock. The colored regions around the pore surface and inside the black square define sets of molecules for which properties are monitored during collapse. In the chosen frame of reference the red, green, and purple arrows define angles of 45° , 90° , and 135° , respectively, with the horizontal pore centerline that points toward the piston. The inset at the top right depicts concentric half-annuli around the pore surface that are also tracked as functions of time and provide a complementary view of the collapse. There is no relation between colors used in the main panel and those used in the inset.

previous studies⁴⁷ where it was shown that, for shocks along $[100]$, using a simulation cell that is thin along $[010]$ does not lead to appreciable finite-size effects. A 35.0 nm diameter cylindrical pore with the cylinder axis aligned parallel to $[010]$ was introduced by removing all molecules with center of mass within 17.5 nm of the midpoint of the slab in the x and z directions. Following the thermalization procedure described in the

following paragraph, molecules in the first three unit cells (≈ 4.0 nm) from the left end of the simulation cell were defined as belonging to the piston and all others as belonging to the flexible slab.

The simulation cell construction described in the preceding paragraph was used as the starting point for all three shock simulations. Different pseudorandom number seeds were used for each simulation. A 10.0 ps equilibration was performed in the isochoric-isoergic (NVE) ensemble using a 0.5 fs time step. During this equilibration instantaneous velocity re-scaling to yield total kinetic energy E_k corresponding to “300 K” (based on $E_k = 3N\kappa T/2$, where N is the number of atoms and κ is the Boltzmann constant), was applied every 50.0 fs and complete velocity re-selection from the 300K Maxwell distribution was performed every 1.0 ps. The purpose of the velocity re-selection in addition to velocity scaling was to damp out the “breathing motion” along [100] that results from introducing the free surfaces. Next, 20.0 ps of Nosé-Hoover isochoric-isothermal (NVT) equilibration was performed using a 0.5 fs time step with the thermostat coupling parameter set to 100.0 fs. Finally, starting from the phase space point at the end of the NVT equilibration, the shock wave was initiated by zeroing (and holding at zero) the velocities of atoms belonging to the piston and adding the impact velocity vector $(-U_p, 0, 0)$ to the instantaneous velocities of the atoms in the flexible slab. The shock simulations were performed in the NVE ensemble using a 0.2 fs time step.

4.3 Results and Discussion

4.3.1 Snapshots of Molecular Center-of-Mass Positions and Local Velocity Fields

Chapter 4: Molecular Dynamics Simulations of the Collapse of a Cylindrical Pore in the Energetic Material α -RDX

Molecular center-of-mass positions, recorded at 0.2 ps intervals during the shock simulations, were used to monitor the progress of the shock. Snapshots of material in the vicinity of the pore at selected instants are shown for the 1.0 km·s⁻¹ shock in Figures 4.2(a,c,e), the 2.0 km·s⁻¹ shock in Figures 4.3(a,c,e), and the 3.0 km·s⁻¹ shock in Figures 4.4(a,c,e). For each shock strength the snapshots correspond to times: (a) during collapse approximately halfway to pore closure; (c) immediately after pore closure; and (e) at the time of maximum compression (that is, when the leading edge of the shockwave, which is curved immediately after passage over the pore, reaches the right-hand end of the sample). Only the upper halves of the simulation cells are shown due to symmetry about the equator of the pore. The colors in the snapshots correspond to those in Figure 4.1(b), which also serves as a reference for the positions of molecules prior to shock passage. The colored regions on the pore surface and inside the black square in the main panel of Figure 4.1(b) designate sets of molecules that will be the focus of much of the analysis and are labeled as follows: the ejection point (blue, *Set I*); $\pm 45^\circ$ to the centerline of the pore (red, *Set II*); the upper and lower poles of the pore (green, *Set III*); $\pm 135^\circ$ to the *Set I*; and bulk material away from the pore (*Set VI*). These regions were used to characterize the response of material as a function of initial position on the pore surface. The inset in the top-right corner of Figure 4.1(b) contains a second scheme for coloring the molecules that highlights different aspects of the collapse. The molecules in both

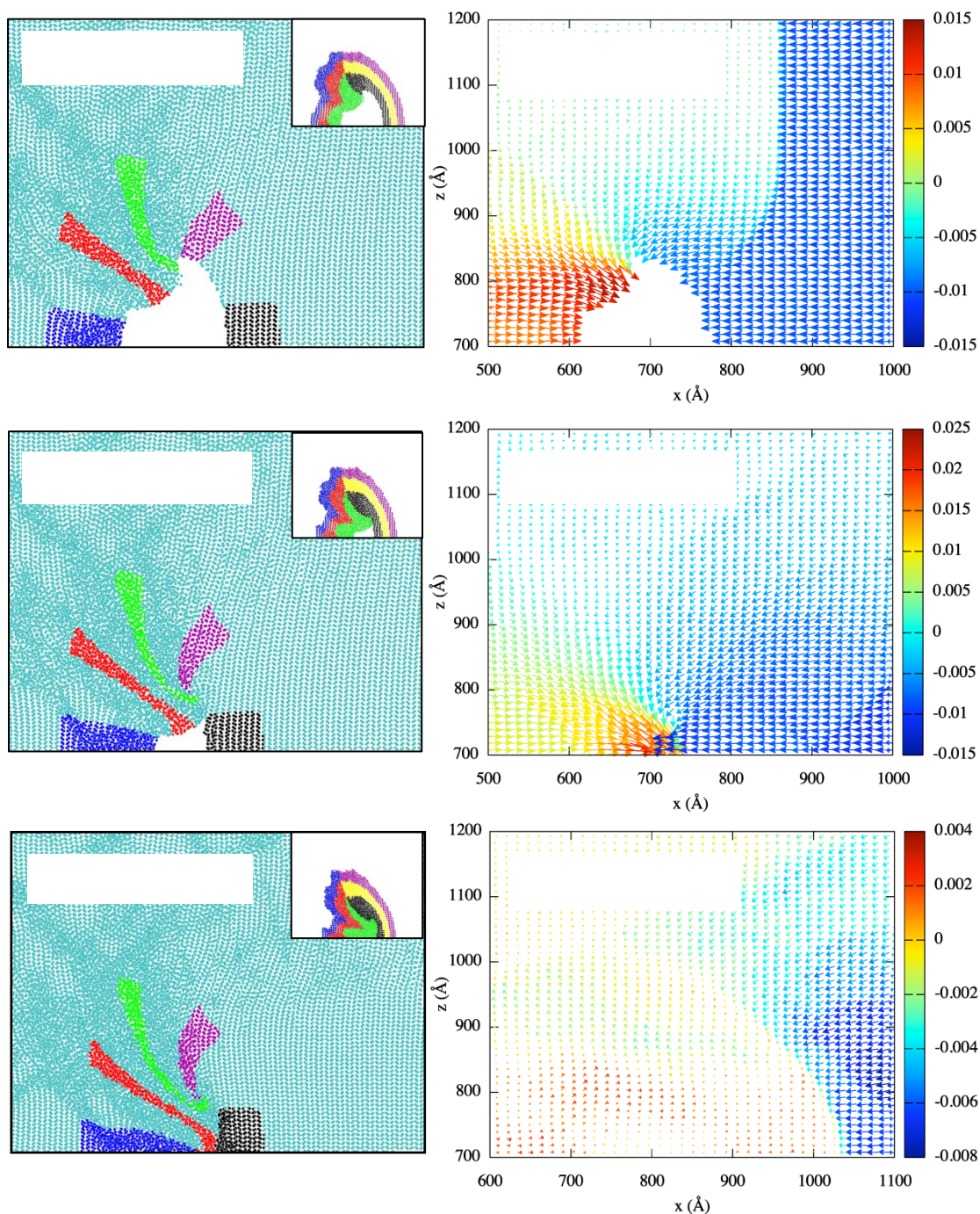


Figure 4.2. Left, panels (a), (c), and (e): Snapshots of molecular centers of mass during pore collapse at three instants of time for the $1.0 \text{ km}\cdot\text{s}^{-1}$ shock. Colors correspond to those shown in Figure 1(b) and illustrate the qualitative features of the mass flow during collapse. Right, panels (b), (d), and (f): Velocity fields for the same instants of time as in the left column. Units for the velocity vector are $\text{\AA}\cdot\text{fs}^{-1}$. Times are relative to the instant when the shock is initiated. Only the upper half of the simulation cell is shown and the view is restricted to material in the vicinity of the pore.

Chapter 4: Molecular Dynamics Simulations of the Collapse of a Cylindrical Pore in the Energetic Material α -RDX

representations retain their color-ID during the simulations and thus convey qualitative information about the nature of overall material deformation during collapse. There is no relationship between the colors used in the two representations. Where appropriate below, averaging over symmetry-equivalent regions of material above and below the equator was performed to improve the statistics.

Local velocity fields, calculated at the same instants as shown in panels (a,c,e) of Figures 4.2-4.4, are shown in panels (b,d,f) of those figures and are used to convey instantaneous flow on the microscopic scale. The velocity fields were calculated in an Eulerian frame by dividing the simulation cell into a 3-D grid of smaller cells in the (x - z) plane. The width and height for each cell are equal to the lattice spacing in the corresponding direction, that is, 1.3498 nm along the x -axis and 1.0564 nm along the z -axis, and the depth extends all the way through the sample in the y -direction. Entire molecules were assigned to the cells based on their instantaneous center-of-mass positions. The x - and z - components of the center-of-mass velocity, v_x and v_z , respectively, were calculated for the material in each cell at a given instant of time and plotted as a vector, with the origin of a given vector located at the geometric center of the corresponding cell.

Many of the experiments and simulations referenced in the Introduction observed a hydrodynamic response during pore collapse, characterized by the focusing of upstream wall material into a fluid-like jet directed along the centerline of the pore. The collapse resulting from the weakest shock we studied ($1.0 \text{ km}\cdot\text{s}^{-1}$, Figure 4.2) shows no signs of jet formation and is dominated by convergence of mainly upstream-side wall material

Chapter 4: Molecular Dynamics Simulations of the Collapse of a Cylindrical Pore in the Energetic Material α -RDX

toward the centerline and downstream wall (Figures 4.2(a,c,e)). In terms of the sets of molecules identified in Figure 4.1(b), the collapse is led by material in Set II flowing into the pore at an angle of approximately 45° to the horizontal. Material initially located in the ejection zone (Set I) initially lags behind but accelerates as the collapse progresses such that ‘frontier’ molecules in Sets I and II arrive at the downstream wall at approximately the same time. Although material in the vicinity of the upstream side of the pore shows signs of intense plastic deformation (*i.e.*, translational disorder), note the persistence of regions of local crystallinity (*i.e.*, relatively high translational order) in some of the material located between Sets I and II throughout the collapse. Velocities in the vicinity of the collapse zone (Figures 4.2(b,d,f)) are close to zero confirming that net translational motion (local mass flow) has halted shortly after collapse. At the time of maximum compression the ‘translational strain’ in the defined sets of molecules initially located at the pore surface is greatest for Sets II and III (red and green, respectively) and least for Set V (black).

The moderate shock ($2.0 \text{ km}\cdot\text{s}^{-1}$, Figure 4.3) results in stronger material focusing during collapse compared to the result obtained for the weak shock case. The molecular velocities of the ejection zone (Set I) and Set II are more strongly oriented along a common axis parallel to the shock direction (Figure 4.3(b)). The material initially in the pole region (Set III) flows toward the centerline with the upstream wall material, producing an enhanced focusing of material with a large component of motion parallel to the centerline. Regions of vorticity are evident in the velocity field during collapse (Figures 4.3(b) and 4.3(d)) as material in Sets III and IV flow toward the centerline after entrainment with ejection zone material. The impact of the ejection zone material on to

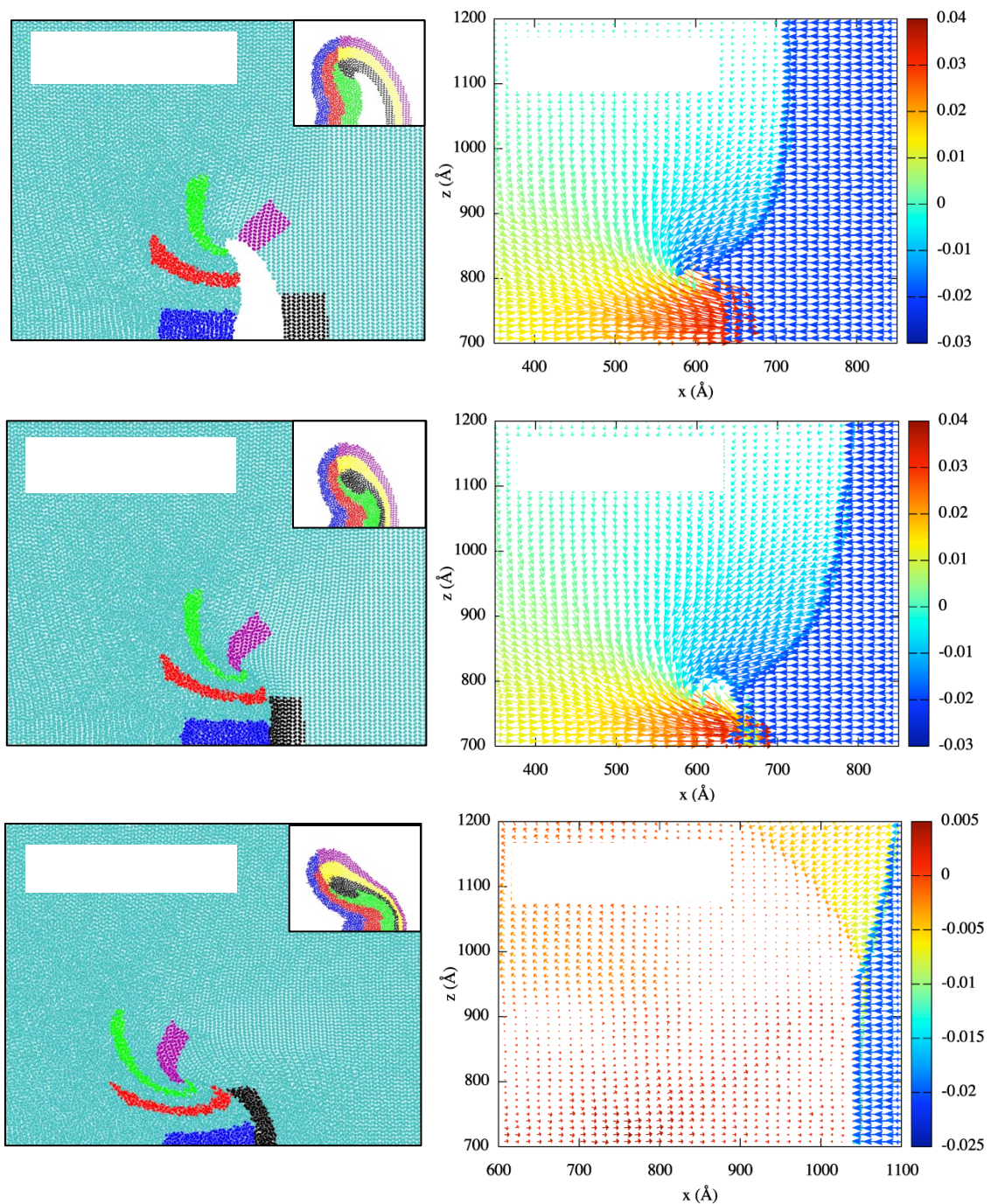


Figure 4.3. As in Figure 4.2, but for the 2.0 km·s⁻¹ impact.

the downstream wall is much stronger than for the weak shock, resulting in more significant deformation of downstream wall material (Figure 4.3(e)). A subsequent flow develops in the vicinity of the impact zone (Figure 4.3(d)) that has stagnated by the time of maximum compression as evidenced by velocities that are near zero in Figure 4.3(f).

The strong shock ($3.0 \text{ km}\cdot\text{s}^{-1}$, Figure 4.4) exhibits an even stronger focusing of material along the pore centerline. Ejection of molecules in Set I with high velocities (Figure 4.4(b)) in conjunction with convergence of the flow of most of the upstream wall material parallel to the horizontal centerline of the pore causes the near-pore material to involute and form a jet (Figures 4.4(a,c)). Compared to the weaker shocks, impact produces a much more severe deformation of the downstream wall material that severely displaces molecules away from a well-ordered crystalline state (Figure 4.4(e)). After pore closure, persistent following flow exists along with regions of vortex-like motion centered on the lobes that pinch shut to complete collapse (Figure 4.4(f)).

As expected, snapshots and velocity fields suggest mechanisms of collapse that depend on the initial impact strength. Weak shock passage results in pore collapse *via* a visco-plastic flow of material that largely ceases when the pore pinches shut, with little penetration of material into the downstream region or residual vorticity in the inflow regions. The moderate shock results in more focusing of the upstream wall material with early signs of jet formation and some amount of penetration into the downstream wall. By contrast, the strong shock focuses material and velocities along the pore centerline strongly enough to create a hydrodynamic jet that penetrates significantly into the downstream wall along with considerable vorticity in the inflow region. The greater focusing of material with increasing impact strength should result in a greater deposition

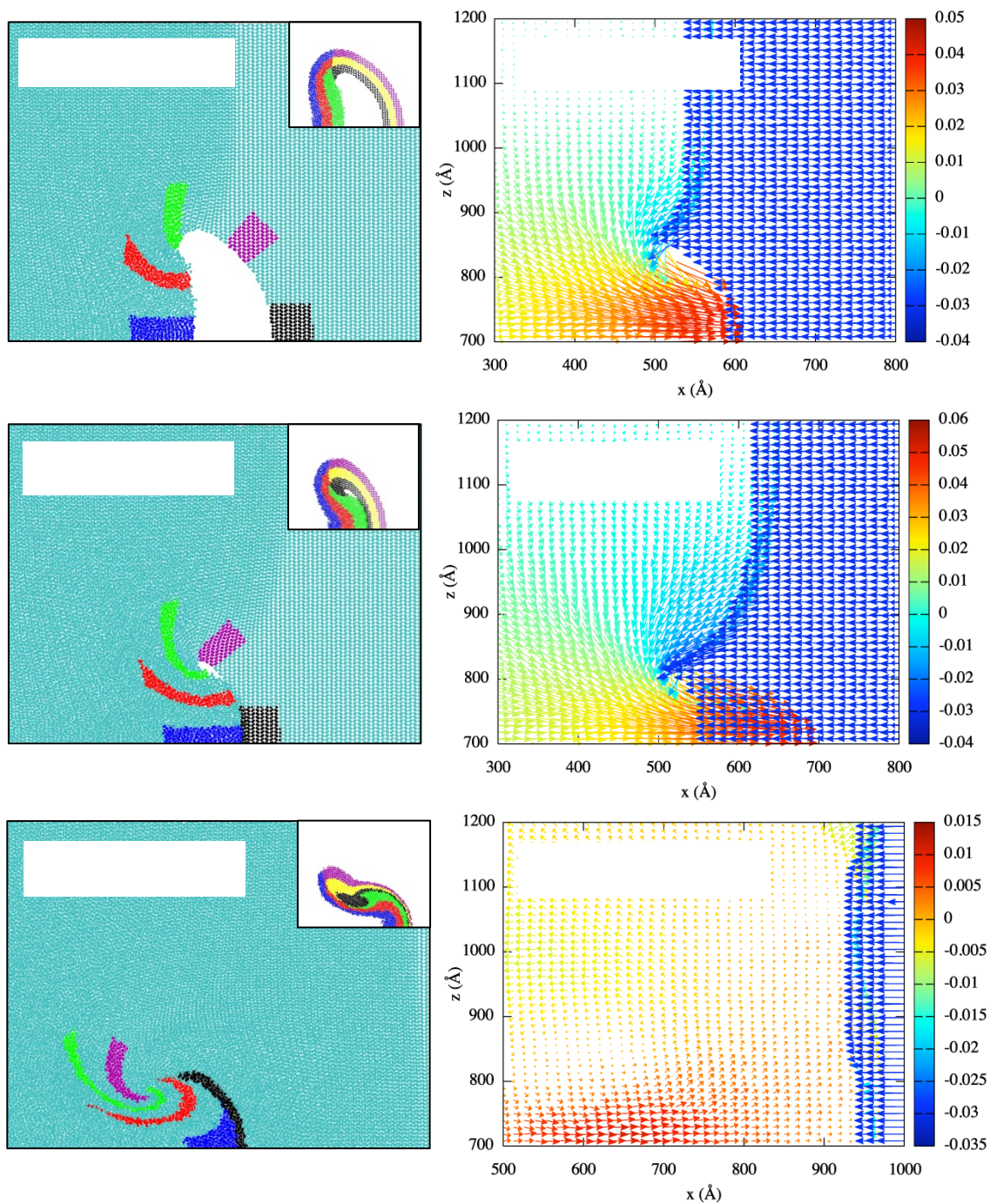


Figure 4.4. As in Figure 4.2, but for the 3.0 km·s⁻¹ impact.

of energy at the stagnation zone, leading to the formation of an intense mechanical hot spot.

4.3.2 Rotational Order During Collapse

Time autocorrelation functions for a time-dependent vector, defined individually in the lab frame for each molecule, were calculated for the molecules in Sets I-V to quantify the extent of molecular rotational motion induced by pore collapse as a function of initial location at the pore surface, and for molecules in Set VI as a point of reference for molecules far from the pore. To calculate the autocorrelation functions, for each molecule m in a given set the unit vector $\hat{r}(t)$ that points from the ring nitrogen atom N1 to carbon atom C4 (see Figure 4.1(a)) was monitored as a function of time t . The time autocorrelation function (ACF) of \hat{r} for molecule m was calculated as

$$C_{m,r}(\tau) = \frac{1}{T-\tau} \sum_{t'=0}^{T-\tau} \sum_{t=t'+\tau}^{T-\tau} \frac{\hat{r}(t) \cdot \hat{r}(t+\tau)}{|\hat{r}(t)| |\hat{r}(t+\tau)|}, \quad (1)$$

where t' is a particular time origin, τ is the positive time lag from that time origin, T is the total interval of time observed (2.0 ps per time window, as elaborated below), and Δt is the spacing between successive data points. All time origins t' within a given time window are treated as equivalent. The range of $C_{m,r}(\tau)$ is $[-1,+1]$ and for a liquid the long-time value should approach zero. The ACF $C_{R,r}(\tau)$ for the molecules in a given set (I-VI) was defined as the arithmetic average of $C_{m,r}(\tau)$ over all M molecules assigned to that set:

$$C_{R,r}(\tau) = \frac{1}{M} \sum_{m=1}^M C_{m,r}(\tau). \quad (2)$$

Chapter 4: Molecular Dynamics Simulations of the Collapse of a Cylindrical Pore in the Energetic Material α -RDX

The analysis was performed separately for contiguous 2.0 ps time windows starting at the instant when the shock wave reached the upstream pore wall and continuing until the time of maximum compression. The results are presented in Figure 4.5, where the dashed vertical lines denote the approximate times of pore closure. Additionally, the ACFs presented in Figure 4.5 were fit to the exponential function,

$$C(\tau) = Ae^{-\frac{\tau}{\alpha}}, \quad (3)$$

to obtain the characteristic rotational time constant α that defines an approximate time scale on which, on average, the molecules in a particular region lose memory of their initial orientation within a given 2.0 ps time window. Smaller α corresponds to faster rotational disordering. Values of α are presented in Table 1 for four selected 2.0 ps time windows for each shock strength. These time constants are not intended as rigorous metrics for rotational diffusion in RDX but instead provide a consistent method for comparing the different extents of rotational motion at different locations and time windows during collapse for the different impact strengths.

In the results from Section 4.3.1 it was seen that passage of the weak shock wave (1.0 km·s⁻¹ impact) collapses the pore in a visco-plastic manner characterized by convergence of mainly upstream wall material along the centerline. The molecular-scale rotational motion as characterized by the autocorrelation function during collapse (Figure 4.5(a)) is consistent with this observation. Molecules in Sets II and III along the upstream wall (red and green curves, respectively) are ejected into the pore at about a $|45^\circ|$ angle to the direction of shock propagation (see Figures 4.2(a) and 4.2(b)) producing strong molecular torques that cause increased rotational motion of the molecules in these sets.

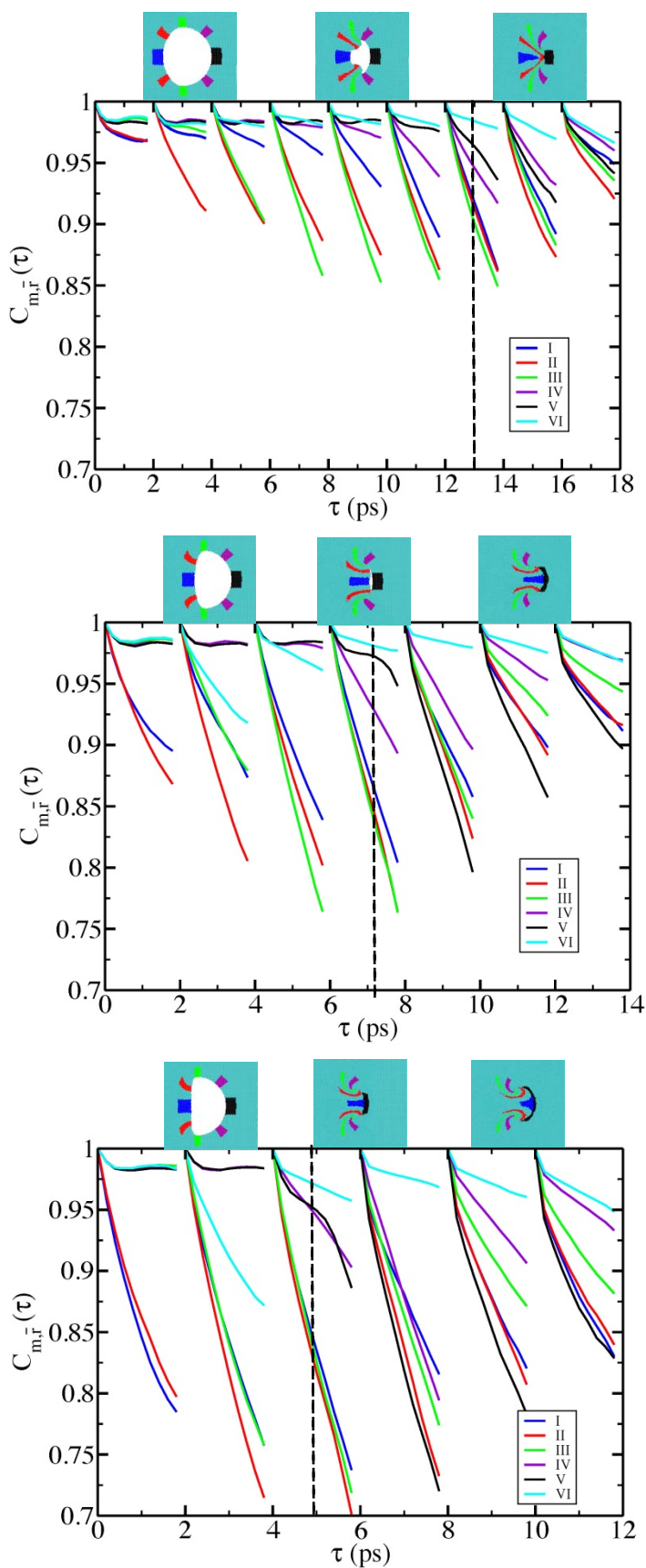


Figure 4.5. Rotational autocorrelation functions during and after pore collapse. (a) $U_p = 1.0 \text{ km}\cdot\text{s}^{-1}$, (b) $U_p = 2.0 \text{ km}\cdot\text{s}^{-1}$, and (c) $U_p = 3.0 \text{ km}\cdot\text{s}^{-1}$. ACFs are calculated in contiguous 2.0 ps time windows starting when the shock reaches the upstream pore wall. The time windows are offset horizontally in the figure for ease of viewing. Line colors coincide with previously defined sets. The vertical dashed lines indicate the approximate times of pore closure. Insets are placed above the curves as representative snapshots of the simulations around the time of analysis.

Chapter 4: Molecular Dynamics Simulations of the Collapse of a Cylindrical Pore in the Energetic Material α -RDX

By contrast, ejection zone material (Set I, blue curve) is ejected into the pore essentially parallel to the shock direction producing less torque on average on the molecules at early times so that less rotational motion occurs compared to the molecules in Sets II and III. These observations are supported by the rotational time constants (see Table 4.1(a)); Sets II and III exhibit much smaller time constants (≈ 18 ps) than Set I (≈ 56 ps) in the early stages of collapse ([4-6] ps time window). It is not until the late stages of collapse ([10-12] ps time window), when molecules initially surrounding the pore are all converging to the “pinch point,” that the time constant for Set I approaches those for Sets II and III. Throughout the collapse, Sets II and III exhibit more rotational motion (lower values of $C_{R,R}(\tau)$ at a given τ) than the ejection zone material and the ACFs for those three sets exhibit greater decay in all time windows than do sets initially on the downstream wall (Sets IV-V) or far from the shock (Set VI).

For the moderate and strong shocks, $2.0 \text{ km}\cdot\text{s}^{-1}$ and $3.0 \text{ km}\cdot\text{s}^{-1}$, Figures 4.5(b) and 4.5(c), and Tables 1(b) and 1(c), respectively, the ACFs for Sets II and III still exhibit the most rapid and greatest magnitude decay during approximately the first half of collapse, but rotational motion in Set I is now similar to these other upstream wall regions (Figures 4.5(b) and 4.5(c), [0-2] and [2-4] ps time windows). Indeed, for the stronger shocks, up until pore closure the rotational time constants for Sets I, II, and III are all within ≈ 6 picoseconds of each other for the $2.0 \text{ km}\cdot\text{s}^{-1}$ shock (Table 4.1(b), [2-4] ps time window) and within less than 2 picoseconds for the $3.0 \text{ km}\cdot\text{s}^{-1}$ shock (Table 4.1(c), [2-4] ps time window).

Table 4.1. Rotational time constants for RDX. Units are ps. Time windows coincide with those presented in Figure 5. Dashes in the table indicate curves in Figure 5 that are not well described by an exponential decay.

(a) $U_p = 1.0 \text{ km}\cdot\text{s}^{-1}$

Set	Time Window			
	[4 – 6]	[10 – 12]	[12 – 14]	[16 – 18]
I	55.6	15.6	12.8	40.0
II	17.9	12.7	12.7	25.0
III	18.2	11.8	11.4	31.2
IV	---	31.2	22.2	50.0
V	---	---	30.3	33.3
VI	---	---	---	62.5

(b) $U_p = 2.0 \text{ km}\cdot\text{s}^{-1}$

Set	Time Window			
	[2 – 4]	[6 – 8]	[8 – 10]	[12 – 14]
I	14.5	8.6	12.8	22.7
II	8.3	7.0	9.9	23.3
III	14.1	6.9	10.8	37.0
IV	---	16.7	17.0	66.7
V	---	45.4	8.4	18.5
VI	21.7	---	---	66.7

(c) $U_p = 3.0 \text{ km}\cdot\text{s}^{-1}$

Set	Time Window			
	[2 – 4]	[4 – 6]	[6 – 8]	[10 – 12]
I	6.7	6.1	9.6	10.8
II	5.4	5.4	6.0	11.5
III	6.5	5.6	7.4	15.9
IV	---	18.9	7.9	30.3
V	---	17.9	5.7	10.6
VI	13.5	---	---	40

Chapter 4: Molecular Dynamics Simulations of the Collapse of a Cylindrical Pore in the Energetic Material α -RDX

Results to the right of the vertical dashed lines in Figure 4.5 are for times between initial pore closure and maximum compression. From the simulation snapshots and velocity fields shown in Figures 4.2-4.4 it is clear that material ejected from the upstream wall stagnates quickly upon impacting the downstream wall for the weak shock, with little further mass flow once the pore has closed; whereas increasing amounts of post-closure flow (penetration) of the upstream wall material into the downstream wall occurs for the moderate and strong shocks. The material stagnation in the vicinity of the collapse zone for the weak shock case is apparent in the autocorrelation function (Figure 4.5(a)). Immediately following collapse ([12-14] ps time window), the collapse zone material (Sets I-V) does not rotationally disorder to a much greater degree than material far from the pore (Set VI) that has mainly only been uniaxially compressed and heated by the shock. By the time of maximum compression ([16-18] ps time window), rotational motion has mostly stagnated throughout the sample.

The collapse-zone regions (Sets I-V) in the moderate shock case (Figure 4.5(b) and Table 4.1(b)) exhibit more rotational motion after collapse than for the weak shock. It was observed in connection with Figure 4.3 that although there is some degree of focusing for the moderate shock case, the focusing is not strong enough to result in a well-formed jet. While there is some penetration into the downstream wall, rotational motion has largely ceased by the time of maximum compression similar to the weak shock (Figure 4.5(b), [12-14] ps time window). It should also be noted that the temperature and pressure are higher in the vicinity of the collapse zone compared to material away from the pore (see Section 4.3.3). The higher temperature (higher kinetic energy) in conjunction with structure disruption due to penetration of the downstream

Chapter 4: Molecular Dynamics Simulations of the Collapse of a Cylindrical Pore in the Energetic Material α -RDX

wall will favor increased rotational motion. However, the higher pressure from compression will serve to reduce the amount of rotational motion. These competing factors probably explain why the results far from the pore (Set VI) are almost quantitatively similar at long times for the two weaker shocks.

Increased rotational motion after pore closure is observed for the strong shock case compared to the two weaker shocks (see Figure 4.5(c) and Table 4.1(c)). The rotational time constants for collapse zone material (Sets I – III) immediately after collapse for the 1.0 km·s⁻¹ and 2.0 km·s⁻¹ shocks are in the 10 – 13 ps range whereas for the 3.0 km·s⁻¹ shock smaller time constants in the 6 – 10 ps range are obtained. There is also evidence in the autocorrelation function for the strong shock of considerable rotational motion at the time of maximum compression (Figure 4.5(c), Table 1(c) [10-12] ps time window). This result is the combined effect of the heating, jet penetration, and persistent high-strain mass flow in the strong shock case.

4.3.3 Temperature and Longitudinal Pressure

Intramolecular (*i.e.*, rotational-vibrational) temperatures and longitudinal pressure components P_{xx} were calculated as functions of location in the sample for several instants of time during pore collapse using the same Eulerian grid described in Section 4.3.1. The intramolecular temperatures, hereafter *temperatures*, were calculated using a previously described method.⁶⁴ The atomic stress tensor for all atoms was saved at 0.2 ps intervals during the simulation, and pressures were then calculated from the longitudinal component of the atomic stress tensor, $P_{xx} = -\sigma_{xx}$, for all atoms in a given Eulerian grid

Chapter 4: Molecular Dynamics Simulations of the Collapse of a Cylindrical Pore in the Energetic Material α -RDX

cell at a given time. Figure 4.6 contains color maps of temperature for all three shock pressures at two times of interest: immediately after initial pore closure (left-hand column) and at the time of maximum compression (right-hand column). Results for the weak, intermediate, and strong shock are shown in the upper, middle, and lower rows (panels (a) and (b), (c) and (d), and (e) and (f), respectively). Figure 4.7 contains profiles of temperature (left-hand column) and longitudinal pressure component P_{xx} (right-hand column) along the shock direction, for material within 5.0 nm of the horizontal centerline, at four different instants after the collapse: when the pore first closes (black solid curves), the time of maximum compression (blue solid curves), and two intermediate times (red and green dashed curves). Figure 4.6 provides a qualitative overall description of the temperature distribution in the material whereas Figure 4.7 provides a more quantitative measure of the peak temperature and longitudinal pressure achieved and how those quantities evolve along the centerline as the collapse occurs.

The temperature maps for the weak shock just after pore closure and at the time of maximum compression are shown in Figures 4.6(a) and 4.6(b), respectively, and the corresponding temperature and longitudinal pressure profiles along the centerline at those times are shown as black and blue solid curves, respectively, in Figures 4.7(a) and 4.7(b). Peak temperatures of ≈ 1500 K and pressures of ≈ 22 GPa are achieved in the vicinity of the collapse zone within about 1 ps of closure (dashed red curves); corresponding temperature and longitudinal pressure values away from the pore are ≈ 400 K and approximately ≈ 9.8 GPa. From the temperature map, heating is limited to a relatively small area in the vicinity of the stagnation point (see Figures 4.6(a) and 4.6(b)); and after modest heating during the first ps after closure, the temperature profile remains relatively

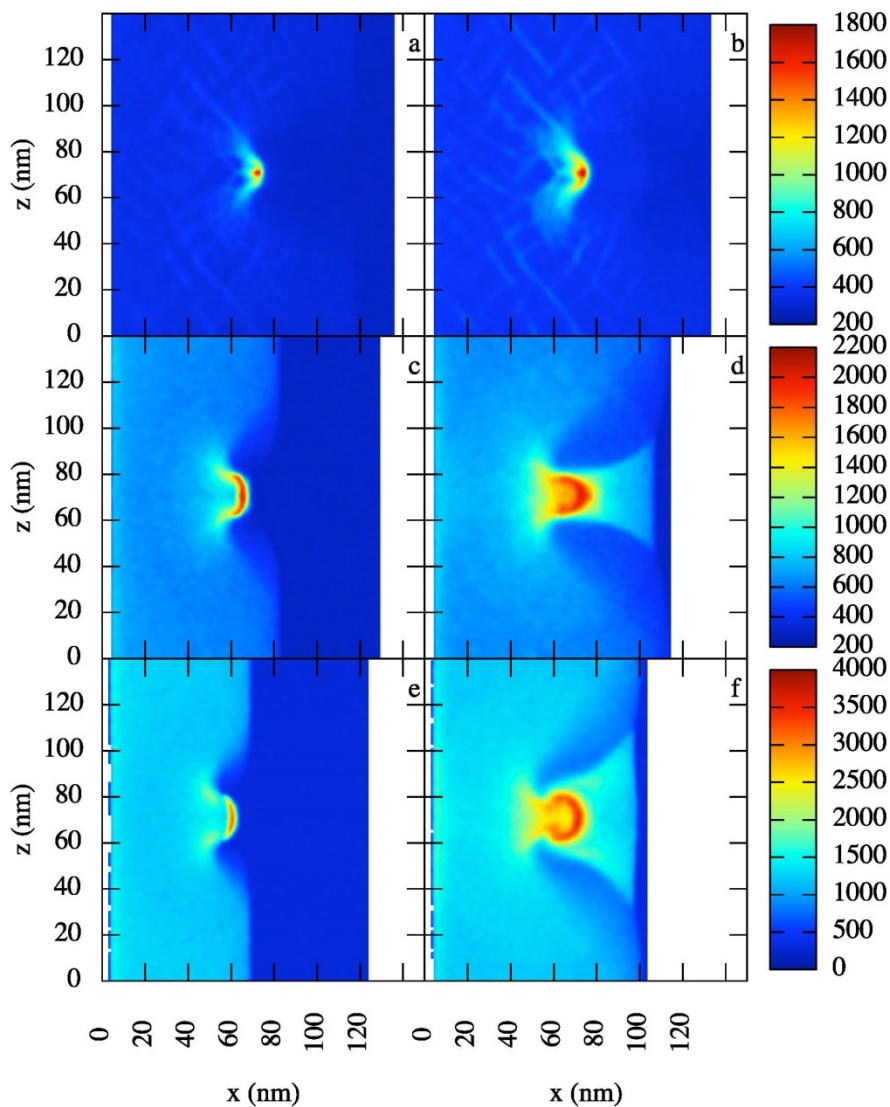


Figure 4.6. Rotational-vibrational temperatures just after pore closure (left column, panels (a), (c), and (e)) and at the time of maximum compression (right column, panels (b), (d), and (f)) for $U_p = 1.0 \text{ km}\cdot\text{s}^{-1}$ (top row), $2.0 \text{ km}\cdot\text{s}^{-1}$ (middle row), and $3.0 \text{ km}\cdot\text{s}^{-1}$ (bottom row). Note that the temperature scale differs for each impact strength. The white line in panel (a) depicts the initial pore diameter, 35 nm, and is intended merely as a visual aid.

Chapter 4: Molecular Dynamics Simulations of the Collapse of a Cylindrical Pore in the Energetic Material α -RDX

constant in the time that elapses between initial pore closure and maximum compression of the system 4.4 ps later (see Figure 4.7(a)).

In contrast to the temperature profiles for the weak shock, the longitudinal pressure profiles (see Figure 4.7(b)) broaden and decrease in amplitude quickly after pore closure. At the time of initial closure (25.2 ps, black solid curve) there is a narrow pressure spike. Pressure waves reflecting from the stagnation point increase the pressure slightly (red dashed curve), after which the two waves quickly decrease in amplitude as they move forward and backward through the material. The 13 GPa peak pressure at the time of maximum compression (blue solid curve value at ≈ 110 nm) is higher than the pressure of 9.71 GPa expected from shock compression in the defect-free crystal of RDX. Presumably, this pressure overshoot would decay to the nominal shock pressure should the simulation time be extended.

Pore collapse resulting from the moderate shock has a greater effect on heating material surrounding the collapse zone than for the weak shock case. Once again a localized region of higher temperatures is visible just after collapse (Figure 4.6(c)). However, in contrast to the result discussed above for the weak shock, in this case temperature at maximum compression (Figure 4.6(d)) exhibits a profile that has evolved considerably since initial closure. The area of the hotter material has increased from Figure 4.6(c) to 4.6(d) and a “fan” is visible between the shock wave and the collapse zone in Figure 4.6(d). The peak temperature along the centerline is ≈ 2000 K (Figure 4.7c) and remains fairly constant in time. However, in contrast to the weak shock case, here the peak broadens considerably over that same time interval. The causes for this are a combination of convection and redistribution of energy from the molecular translational

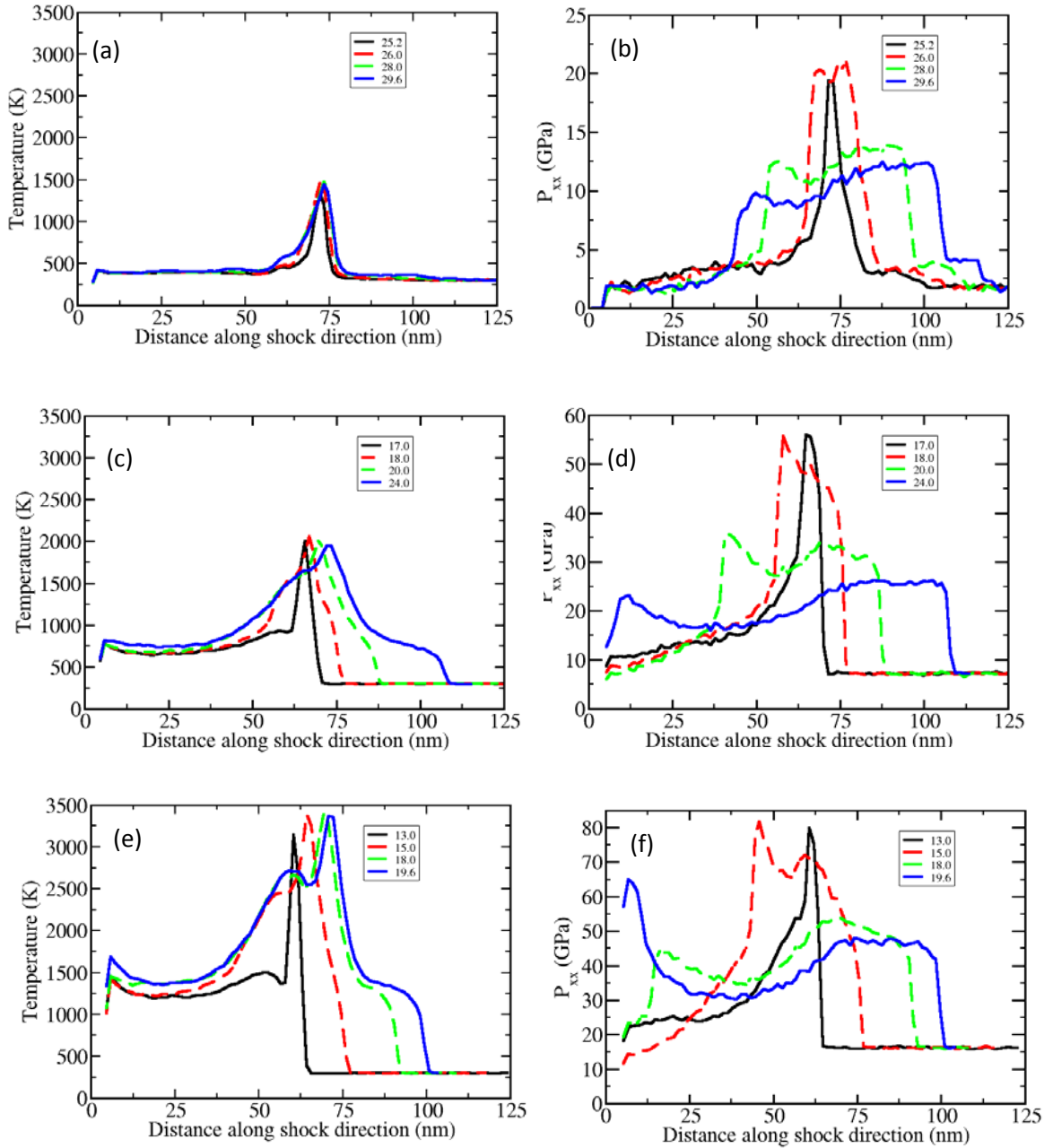


Figure 4.7. Spatial profiles of temperature (left column) and longitudinal stress (right column) parallel to the shock direction. The results are for a strip of material located within 5 nm of the horizontal centerline of the simulation cell for three different impact speeds U_p . Panels (a) and (b): $U_p = 1.0$ km·s⁻¹; panels (c) and (d) 2.0 km·s⁻¹; panels (e) and (f): 3.0 km·s⁻¹. Lines are colored according to elapsed time, in ps, since initiation of the shock, with the shortest (black) and longest (blue) elapsed times depicted using solid curves and the intermediate times (red and green) depicted using dashed curves.

degrees of freedom in the flow to intramolecular kinetic energy in the stagnated region.

A secondary compressive wave centered on the collapse zone is visible in the pressure profiles (Figure 4.7d). Similar to the $1.0 \text{ km}\cdot\text{s}^{-1}$ impact case, pressure waves that quickly decrease in amplitude are reflected from the stagnation point. The peak pressure value in Figure 4.7(d) at the time of maximum compression is $\approx 25 \text{ GPa}$, which is close to the Rankine-Hugoniot shock pressure of 24.00 GPa , but much less than the peak pressure, $\approx 55 \text{ GPa}$, at the time of initial pore closure 4.7 ps earlier.

The evolution of the temperature distribution becomes much more pronounced when considering the strong shock wave generated by the $3.0 \text{ km}\cdot\text{s}^{-1}$ impact (Figures 4.6(e) and 4.6(f)). Similar to the moderate shock case, an arc of localized heating is visible just after collapse (Figure 4.6(e)) corresponding to recompression and partial stagnation of molecules against the downstream pore wall. Additionally, there are two lobes of heated material located just above and below the centerline and $\approx 10 \text{ nm}$ behind the leading edge of the stagnation region. These lobes coincide with the small vortex regions generated near the end of pore closure (Figure 4.4(d)). The temperature distribution changes noticeably in the time interval between cavity closure and maximum compression, with the collapse zone material convecting heat to surrounding material. Once again, the temperature peak broadens in the time interval between closure and maximum compression (Figure 4.7(e)). An initial narrow peak at about 3100 K , just after closure at 13 ps , is visible that broadens considerably with increasing time after closure. The increased peak broadening is attributed to increased amounts of convection due to

the greater penetration of the downstream wall and more translational kinetic energy from the stronger shock that is redistributed into intramolecular energy.

As for the intermediate shock strength, a secondary compression wave is evident in the pressure profiles for the strong shock case (Figure 4.7(f)). An initial pressure spike to ≈ 80 GPa is visible shortly after closure at 13 ps. Reflected waves originating at the stagnation point travel out through the material recompressing the system. Once again, the amplitude of the reflected waves decreases quickly as they travel through the system. The peak pressure at maximum compression is ≈ 45 GPa, which compares to the calculated Rankine-Hugoniot shock pressure of 42.48 GPa. (The peak located near the piston at 19.6 ps is taken to be an artifact of the fast traveling wave reflecting off of the piston.)

Ideally one would like to monitor the samples for longer times to determine whether or to what extent pore collapse affects the long-time structural properties. However, the time scale available in the current studies is limited by the shock wave reaching the right-hand side of the sample. Shock front absorbing boundary conditions have been employed in previous studies^{47,65} to extend the amount of simulation time available for data analysis. However, the SFABC method is not suitable for the current simulations due to the numerous secondary waves in the material that arise due to reflections from the piston and the pore surfaces, which would severely complicate analysis and interpretation of the results.

4.4 Conclusions

The shock-induced collapse of a 35 nm diameter cylindrical pore in the energetic crystal α -RDX was observed for three different impact velocities using molecular dynamics simulations. For the $1.0 \text{ km}\cdot\text{s}^{-1}$ shock, the pore collapses in a visco-plastic manner wherein net translational motion ceases after collapse and there is little convection of heat to material away from the collapse zone. The collapse at $2.0 \text{ km}\cdot\text{s}^{-1}$ exhibits more focusing along the pore centerline than does the $1.0 \text{ km}\cdot\text{s}^{-1}$ shock. Material focusing results in a greater amount of downstream wall penetration following impact. The stronger penetration produces more molecular rotation during and after collapse along with a greater amount of energy convection to material away from the initial collapse zone.

For the $3.0 \text{ km}\cdot\text{s}^{-1}$ shock, an enhanced focusing of material occurs along the pore centerline that is sufficient to produce a fluid-like jet structure during collapse. The jet causes a greater deposition of mechanical energy at the downstream wall leading to much higher temperatures achieved in the collapse zone. Jet penetration into the downstream wall upon impact leads to the development of a following flow after closure. Translational kinetic energy in this inflow region is redistributed to intramolecular kinetic energy and is spread to surrounding material through convection. Critical-size hot spots remain beyond the current computational capabilities of MD simulations. However, simulations on the atomic scale such as those presented in this work can provide insight into the fundamental collapse mechanism of pores in energetic materials. This information, in combination with continuum-scale models and experimental data, can aid

Chapter 4: Molecular Dynamics Simulations of the Collapse of a Cylindrical Pore in the Energetic Material α -RDX

the development of a more complete understanding of the role of pore collapse in hot spot generation.

References

- (1) Bowden, F. P.; Yoffe, A. D. *Initiation and Growth of Explosion in Liquids and Solids*; Cambridge, **1952**.
- (2) Handley, C. Numerical Modeling of two HMX-based plastic-bonded explosives at the mesoscale, St. Andrews University, **2011**.
- (3) Tarver, C. M.; Chidester, S. K.; Nichols, A. L. *The Journal of Physical Chemistry* **1996**, *100*, 5794.
- (4) Field, J. E. *Accounts of Chemical Research* **1992**, *25*, 489.
- (5) Bowden, F. P.; McOnie, M. P. *Proceedings of the Royal Society of London. Series A. Mathematical and Physical Sciences* **1967**, *298*, 38.
- (6) Coley, G. D.; Field, J. E. *Proceedings of the Royal Society of London. A. Mathematical and Physical Sciences* **1973**, *335*, 67.
- (7) Winter, R. E.; Field, J. E. *Proceedings of the Royal Society of London. A. Mathematical and Physical Sciences* **1975**, *343*, 399.
- (8) Coffey, C. S. *Physical Review B* **1981**, *24*, 6984.
- (9) Bowden, F. P.; Gurton, O. A. *Proceedings of the Royal Society of London. Series A. Mathematical and Physical Sciences* **1949**, *198*, 337.
- (10) Dear, J. P.; Field, J. E.; Walton, A. J. *Nature* **1988**, *332*, 505.
- (11) Bourne, N. K.; Field, J. E. *Proceedings of the Royal Society of London. Series A: Mathematical and Physical Sciences* **1991**, *435*, 423.
- (12) Bourne, N. K.; Field, J. E. *Proceedings of the Royal Society of London. Series A: Mathematical, Physical and Engineering Sciences* **1999**, *455*, 2411.
- (13) Bourne, N. K.; Milne, A. M. *Proceedings of the Royal Society of London. Series A: Mathematical, Physical and Engineering Sciences* **2003**, *459*, 1851.
- (14) Swantek, A. B.; Austin, J. M. *Journal of Fluid Mechanics* **2010**, *649*, 399.
- (15) Dattelbaum, D. M.; Sheffield, S. A.; Stahl, D. B.; Dattelbaum, A. M.; Trott, W.; Engelke, R. In *Fourteenth Symposium (International) on Detonation* **2010**.
- (16) Stoltz, C. A.; Mason, B. P.; Hooper, J. *Journal of Applied Physics* **2010**, *107*.
- (17) Mang, J. T.; Hjelm, R. P.; Francois, E. G. *Propellants, Explosives, Pyrotechnics* **2010**, *35*, 7.
- (18) Mang, J. T.; Hjelm, R. P. *Propellants, Explosives, Pyrotechnics* **2011**, *36*, 439.
- (19) Menikoff, R. *AIP Conference Proceedings* **2004**, *706*, 393.
- (20) Ball, G. J.; Howell, B. P.; Leighton, T. G.; Schofield, M. J. *Shock Waves* **2000**, *10*, 265.
- (21) Bourne, N. K.; Field, J. E. *Journal of Fluid Mechanics* **1992**, *244*, 225.
- (22) Tran, L.; Udaykumar, H. S. *Journal of Propulsion and Power* **2006**, *22*, 947.
- (23) Tran, L.; Udaykumar, H. S. *Journal of Propulsion and Power* **2006**, *22*, 959.
- (24) Jackson, T. L.; Buckmaster, J. D.; Zhang, J.; Anderson, M. J. *Combustion Theory and Modelling* **2015**, *19*, 347.
- (25) Barton, N. R.; Winter, N. W.; Reaugh, J. E. *Modelling and Simulation in Materials Science and Engineering* **2009**, *17*, 035003.
- (26) Austin, R. A.; Barton, N. R.; Howard, W. M.; Fried, L. E. *Journal of Physics: Conference Series* **2014**, *500*, 052002.
- (27) Austin, R. A.; Barton, N. R.; Reaugh, J. E.; Fried, L. E. *Journal of Applied Physics* **2015**, *117*, 185902.
- (28) Levesque, G. A.; Vitello, P. *Propellants, Explosives, Pyrotechnics* **2015**, *40*, 303.
- (29) Holian, B. L.; Germann, T. C.; Maillet, J. B.; White, C. T. *Physical Review Letters* **2002**, *89*, 285501.

Chapter 4: Molecular Dynamics Simulations of the Collapse of a Cylindrical Pore in the Energetic Material α -RDX

- (30) Hatano, T. *Physical Review Letters* **2004**, 92, 015503.
- (31) Shi, Y.; Brenner, D. W. *The Journal of Physical Chemistry C* **2008**, 112, 6263.
- (32) Mintmire, J. W.; Robertson, D. H.; White, C. T. *Physical Review B* **1994**, 49, 14859.
- (33) Herring, S. D.; Germann, T. C.; Grønbech-Jensen, N. *Physical Review B* **2010**, 82, 214108.
- (34) van Duin, A. C. T.; Dasgupta, S.; Lorant, F.; Goddard III, W. A. *The Journal of Physical Chemistry A* **2001**, 105, 9396.
- (35) Strachan, A.; Kober, E. M.; van Duin, A. C. T.; Oxgaard, J.; Goddard III, W. A. *The Journal of Chemical Physics* **2005**, 122, 054502.
- (36) Shan, T. R.; Thompson, A. P. *Journal of Physics: Conference Series* **2014**, 500, 172009.
- (37) Thompson, A. P.; Shan, T. R. *Journal of Physics: Conference Series* **2014**, 500, 052046.
- (38) Hooks, D. E.; Ramos, K. J.; Martinez, A. R. *Journal of Applied Physics* **2006**, 100, 024908.
- (39) Ramos, K. J.; Hooks, D. E.; Bahr, D. F. *Philosophical Magazine* **2009**, 89, 2381.
- (40) Dang, N. C.; Dreger, Z. A.; Gupta, Y. M.; Hooks, D. E. *The Journal of Physical Chemistry A* **2010**, 114, 11560.
- (41) Ramos, K. J.; Hooks, D. E.; Sewell, T. D.; Cawkwell, M. J. *Journal of Applied Physics* **2010**, 108, 066105.
- (42) Doherty, R. M.; Watt, D. S. *Propellants, Explosives, Pyrotechnics* **2008**, 33, 4.
- (43) Infante-Castillo, R.; Pacheco-Londoño, L. C.; Hernández-Rivera, S. P. *Journal of Molecular Structure* **2010**, 970, 51.
- (44) Elban, W. L.; Hoffsommer, J. C.; Armstrong, R. W. *J Mater Sci* **1984**, 19, 552.
- (45) Patterson, J. E.; Dreger, Z. A.; Gupta, Y. M. *The Journal of Physical Chemistry B* **2007**, 111, 10897.
- (46) Shi, Y.; Brenner, D. W. *The Journal of Physical Chemistry B* **2008**, 112, 14898.
- (47) Cawkwell, M. J.; Sewell, T. D.; Zheng, L.; Thompson, D. L. *Physical Review B* **2008**, 78, 014107.
- (48) Bedrov, D.; Hooper, J. B.; Smith, G. D.; Sewell, T. D. *The Journal of Chemical Physics* **2009**, 131, 034712.
- (49) Cawkwell, M. J.; Ramos, K. J.; Hooks, D. E.; Sewell, T. D. *Journal of Applied Physics* **2010**, 107, 063512.
- (50) Munday, L. B.; Chung, P. W.; Rice, B. M.; Solares, S. D. *The Journal of Physical Chemistry B* **2011**, 115, 4378.
- (51) Nomura, K.; Kalia, R. K.; Nakano, A.; Vashishta, P. *Appl. Phys. Lett.* **2007**, 91, 183109.
- (52) Mathew, N.; Picu, R. C. *The Journal of Chemical Physics* **2011**, 135, 024510.
- (53) Choi, C. S.; Prince, E. *Acta Crystallographica Section B* **1972**, 28, 2857.
- (54) Millar, D. I. A.; Oswald, I. D. H.; Francis, D. J.; Marshall, W. G.; Pulham, C. R.; Cumming, A. S. *Chemical Communications* **2009**, 562.
- (55) Millar, D. I. A.; Oswald, I. D. H.; Barry, C.; Francis, D. J.; Marshall, W. G.; Pulham, C. R.; Cumming, A. S. *Chemical Communications* **2010**, 46, 5662.
- (56) Davidson, A. J.; Oswald, I. D. H.; Francis, D. J.; Lennie, A. R.; Marshall, W. G.; Millar, D. I. A.; Pulham, C. R.; Warren, J. E.; Cumming, A. S. *CrystEngComm* **2008**, 10, 162.
- (57) Munday, L. B.; Solares, S. D.; Chung, P. W. *Philosophical Magazine* **2012**, 92, 3036.
- (58) Gallagher, H. G.; Halfpenny, P. J.; Miller, J. C.; Sherwood, J. N.; Tabor, D. *Philosophical Transactions of the Royal Society of London. Series A: Physical and Engineering Sciences* **1992**, 339, 293.
- (59) Mathew, N.; Picu, C. R.; Chung, P. W. *The Journal of Physical Chemistry A* **2013**, 117, 5326.
- (60) Plimpton, S. *Journal of Computational Physics* **1995**, 117, 1.

Chapter 4: Molecular Dynamics Simulations of the Collapse of a Cylindrical Pore in the Energetic Material α -RDX

- (61) Smith, G. D.; Bharadwaj, R. K. *The Journal of Physical Chemistry B* **1999**, *103*, 3570.
- (62) Bedrov, D.; Ayyagari, C.; Smith, G.; Sewell, T.; Menikoff, R.; Zaug, J. *Journal of Computer-Aided Materials Design* **2001**, *8*, 77.
- (63) Hockney, R. W.; Eastwood, J. W. *Computer Simulations Using Particles*; McGraw-Hill: New York, **1981**.
- (64) Eason, R. M.; Sewell, T. D. *The Journal of Physical Chemistry C* **2011**, *116*, 2226.
- (65) Bolesta, A. V.; Zheng, L.; Thompson, D. L.; Sewell, T. D. *Physical Review B* **2007**, *76*, 224108.

Chapter 5: Conclusions

A complete understanding of the shock to initiation to detonation process in energetic materials will require analysis from multiple disciplines (chemistry/physics/engineering/materials science/computer science) across a wide range of temporal and spatial scales. Emphasis must be placed on comprehending how information from each of these disciplines contributes to the knowledge base of energetic material response. What we seek, in addition to understanding the phenomena on particular space and time scales, is the development of verified methods and validated models that provide a robust predictive capability based on sound physics, chemistry, numerical simulations, and other fundamental disciplines. The focus of the research in this thesis has been on two energetic materials, PETN and RDX, studied at the atomic scale with the aid of molecular dynamics simulations. Both projects were attempts to provide insight at the Å to μm length scale and femtosecond to picosecond time scale to events that have been observed at larger scales.

In the case of PETN, an orientation dependent shock response had been observed previously by experimental methods. A “steric hindrance model” was proposed to explain the dependence of detonation sensitivity on crystal orientation, whereby insensitive orientations were able to relieve shock-imparted stresses through slip while sensitive orientations were sterically hindered from relieving shock stresses. The theoretical results presented in Chapter 3 agree well with the experimentally based steric hindrance model. Relative molecular displacements were calculated as a metric to quantify the amount of displacement that occurs for crystals of PETN when shocked along a specific direction.

Chapter 5: Conclusions

The results obtained from relative molecular displacement and temperature calculations for a shock propagating along the sensitive [001] direction are consistent with only elastic compression of the material, whereas the results for shock propagating along the insensitive [100] direction are consistent with plastic deformation of the material. This is an example of the ability of Molecular Dynamics simulations to make contact with and then extend a description of events observed experimentally at the macroscale.

Shocks in defect-containing RDX were examined in Chapter 4. The shock-induced collapse of pores in energetic materials has been often studied due to the fact that pores are potential sites of “hot spot” formation that can lead to ignition and potentially acceleration and spread of chemistry in energetic materials. As discussed in the introduction to Chapter 4, much of the analysis on pore collapse up to this point has been performed at the micron to millimeter scale using experimental methods and continuum scale simulations. It is only within the past few years that MD simulations have been applied to pore collapse for energetic materials. This work presents some initial steps into the study of shock-induced pore collapse in RDX. Results were obtained that were largely consistent with previous experimental and continuum-scale studies. A visco-plastic and a hydrodynamic collapse response were observed depending on the initial impact strength. The visco-plastic response resulted in very little energy localization and minimal long-term effect on the surrounding material. However, the hydrodynamic response produced a jet that localized energy at the downstream wall and resulted in enhanced temperatures and pressures upon impact.

There are obviously areas that can be improved on for the models, simulations, and analysis presented in this work. One rather important approximation throughout these

Chapter 5: Conclusions

studies has been the neglect of chemistry due to the use of a non-reactive force field. The error introduced by this approximation has been assumed to be minimal (or, in the simulations of strong shock in RDX, simply ignored) due to the short time scale of the events being studied and the fact that we were primarily concerned with the mechanical response of materials being studied. However, it would still prove useful to quantify just how much of an effect the approximation has on the results. Performing simulations with a reactive force field such as ReaxFF is one possibility. However, as mentioned earlier, the primary concern in our studies has been with the mechanical response of shocked energetic materials, and that the Smith force field was specifically chosen for the ability to predict accurate thermo-mechanical properties. Modification of the Smith force field to include reactivity would also not be a simple task but there are minor tweaks that could offer insight. For example, use of a Morse potential in place of the harmonic term would be a more realistic representation of a chemical bond. Once sufficient vibrational energy is distributed into the intramolecular modes then bond rupture would occur; this would help provide information on when our approximation neglecting chemistry begins to break down. However, this would need to be done within such a framework that the simulation would stop when the first reaction occurred, because the forces would become unrealistic if bond lengths were large but other covalent forces (angles, dihedrals, impropers) were retained and if the effect of breaking one bond on the local electronic structure in molecules was neglected.

The PETN case considered only perfect crystals whereas real world materials will always contain defects. It would be interesting to analyze the effect that the presence of defects will have on the observed elastic/plastic responses. Furthermore, only two

Chapter 5: Conclusions

different orientations were studied in this work; the sensitive [001] direction and the insensitive [100] direction. Further analysis can be performed to determine if the same qualitative features are observed for the other sensitive orientation, [110], and all other orientations that are insensitive. The RDX case did consider defects but current computational capabilities do not allow simulations of pores at sizes that are thought to be dominant in producing critical hot spots. As computational power increases in the future it will be interesting to consider larger pores that are perhaps closer to those present in real world materials. Additionally, the RDX study was a first step along the path of studying pores in energetic materials at the atomic scale using molecular dynamics, most of the results presented were largely of a qualitative nature. The simulated trajectories still contain huge amounts of information that have yet to be explored. There is a wealth of information that can be gathered by application of more rigorous metrics to characterize the energy localization and stress deposition that results from pore collapse.

The studies presented in this thesis are an example of theoretical analysis at the atomic scale being able to supplement and provide insight into events that are observed at the macroscale. The force fields used were parameterized largely with data obtained from quantum chemistry calculations, simulations were performed using computer codes based on classical dynamics, and then analysis was performed with the results being compared to available experimental data. This is in keeping with the theme put forth in Chapter 1 of coupling analysis of energetic materials across multiple scales to reach a more complete understanding of the shock to initiation to detonation process.

Vita

Reilly Michael Eason was born June 28, 1983 in Jackson, Tennessee to Mike and Judy Eason. He started pursuit of a bachelor's degree in Chemistry at Union University in 2004 and it was there that Dr. Michael Salazar inspired a love of Physical Chemistry. With the aid of Dr. Salazar, Reilly was accepted into the doctoral program at the University of Missouri. There he began working for Dr. Thomas Sewell in the field of Theoretical Chemistry. He obtained his Ph.D. in the Spring of 2016 and currently works as the chemist for Fluid Routing Solutions.